REPUBLIQUE ALGERIENNE DEMOCRATIQUE ET POPULAIRE
MINISTERE DE L'ENSEIGNEMENT SUPERIEUR ET DE LA RECHERCHE SCIENTIFIQUE
UNIVERSITE DE MEDEA



FACULTE DE TECHNOLOGIE

THESE DE DOCTORAT

Présentée en vue de l'obtention du diplôme de

Docteur en : Génie Mécanique

Spécialité : Génie des matériaux

Présentée par : BENATALLAH MOHAMED AMINE

Thème

Contribution à la fabrication et caractérisation des matériaux à énergie solaire photovoltaïques à base de pérovskite organique et inorganique

Présentée devant le jury composé de :

Nom & Prénom	Grade	Institution d'affiliation	Désignation
ZIRARI Mounir	Pr	Université de Médéa	Président
ELMOHRI Abdennour	MCA	Université de Médéa	Directeur de thèse
Rabhi Selma	MCA	Université de Constantine	Co- Directeur de thèse
CHIBA Younes	Pr	Université de Médéa	Examinateur 1
BENCHERIF Hichem	MCA	HNS-RE2SD de Batna	Examinateur 2

Année académique : 2025/2026

PEOPLE'S DEMOCRATIC REPUBLIC OF ALGERIA
MINISTRY OF HIGHER EDUCATION AND SCIENTIFIC RESEARCH
UNIVERSITY YAHIA FARES OF MEDEA



FACULTY OF TECHNOLOGY

THESIS

To obtain the degree of

DOCTOR in: Mechanical Engineering

Specialty: Materials Engineering

Presented by: BENATALLAH MOHAMED AMINE

Thesis title

Contribution to the Fabrication and Characterization of Photovoltaic Solar Energy Materials Based on Organic and Inorganic Perovskite

Defended in front of a jury composed of:

Last and first name	Grade	Institution of affiliation	Designation
ZIRARI Mounir	Pr	University of Medea	President
ELMOHRI Abdennour	MCA	University of Medea	Supervisor
Rabhi Selma	MCA	University of Constantine	Co-supervisor
CHIBA Younes	Pr	University of Medea	Examiner 1
BENCHERIF Hichem	MCA	HNS-RE2SD of Batna	Examiner 2

Academic year : 2025/2026

الملخص:

تركز هذه الاطروحة الدكتوراه على الدراسة العددية وتحسين الخلايا الشمسية بيروفسكايت(PSCs) ، والتي تُعد من أكثر التقنيات الكهروضوئية الواعدة للجيل القادم. وبفضل خصائصها البصرية والإلكترونية المتميزة، وإمكانية ضبط فجوتها الطاقوية، وانخفاض تكلفة تصنيعها، فقد حققت هذه الخلايا كفاءات تحويل طاقوي (PCE) مرتفعة. ومع ذلك، لا تزال مشاكل الاستقرار، وصعوبات التوسع الصناعي، وسُمية الرصاص تمثل عوائق رئيسية أمام تسويقها على نطاق واسع .في هذا العمل، تم استخدام برنامج SCAPS-1D كأداة عددية لدراسة فيزياء الخلية وتقييم استراتيجيات التحسين. وقد تم تقسيم هذه الدراسة إلى قسمين رئيسيين. ركز القسم الأول على الخلايا الشمسية بيروفسكايت المرنة، حيث تمت دراسة دور مواد جديدة لنقل الشحنات مثل طبقات نقل الثقوب :(HTLs) ACZTSe، $CuBiS_3$، CZGS، D-PBTTT-14، وCu_2O Se/Te-doped، بالإضافة إلى طبقات نقل الإلكترونات :(ETLs) SnS_2، $BaZrS_3$، STO، WS_2، و ZrS_2.كما تمت دراسة تأثير عيوب الواجهات من خلال إضافة طبقة بيروفسكايت ثنائية الأبعاد-2D (PVKبهدف تحسين الخصائص البينية، حيث تم اختيار مادة CBz-PAI كطبقة تمرير بينية. علاوة على ذلك، تمت دراسة تأثير الملامس الخلفي المعتمد علىMXene ، والذي أظهر تحسينات ملحوظة في استخلاص الشحنات، وتقليل إعادة التركيب، وتعزيز استقرار الواجهات. وقد حققت الخلية الشمسية المرنة المحسّنة كفاءة تحويل طاقوي بلغت 27.17%.أما القسم الثاني فقد ركز على الخلايا الشمسية بيروفسكايت ثنائية الوجه(Bifacial PSCs) ، من خلال تحليل أدائها تحت الإضاءة الأمامية والخلفية، مع إبراز الدور الحاسم لهندسة الطبقات وتحسين انتقال الشحنات في تحقيق كفاءات أعلى وتحسين الأداء الكهروضوئي العام. وقد حقق الجهاز ثنائي الوجه المحسن كفاءة بلغت 28.38% للواجهة الأمامية و28.27% للواجهة الخلفية .تساهم نتائج هذه الأطروحة في ربط النمذجة النظرية بالتطبيقات العملية، كما تقدم استراتيجيات واعدة لتطوير خلايا شمسية بيروفسكايت أكثر كفاءة واستقرارًا واستدامة، مما يمهد الطريق نحو تطبيقات كهروضوئية واسعة النطاق وصديقة للبيئة.

الكلمات المفتاحية: الخلايا الشمسية بيروفسكايت(PSCs) ، محاكاةSCAPS-1D ، الخلايا الكهروضوئية المرنة، الخلايا الشمسية ثنائية الوجه، كفاءة التحويل الطاقوي(PCE) ، الطاقة المتجددة.

Abstract :

This doctoral thesis focuses on the numerical investigation and optimization of perovskite solar cells (PSCs), recognized as one of the most promising next-generation photovoltaic technologies. Due to their outstanding optoelectronic properties, tunable bandgap, and low-cost fabrication, PSCs have achieved remarkable power conversion efficiencies (PCEs). However, stability issues, scalability challenges, and lead toxicity remain major obstacles to their commercialization. In this work, the SCAPS-1D simulator was employed as a numerical tool to investigate device physics and evaluate optimization strategies. This study was divided into two sections. The first section focused on flexible perovskite solar cells, where we investigated the role of novel charge transport materials such as HTLs: ACZTSe, $CuBiS_3$, CZGS, D-PBTTT-14, and Se/Te-doped Cu_2O, as well as ETLs: SnS_2, $BaZrS_3$, STO, WS_2, and ZrS_2. In these solar cells, interface defects were examined, where a two-dimensional perovskite (2D-PVK) layer was added to enhance the interfacial effect. CBz-PAI was selected as the interfacial passivation layer. Moreover, the back contact was also investigated, which demonstrated significant improvements in charge extraction, reduced recombination, and enhanced interfacial stability. The optimized flexible perovskite solar cell achieved a power conversion efficiency of 27.17%. The second section focused on bifacial perovskite solar cells (Bifacial PSCs), analyzing their performance under both front and rear illumination, and highlighting the critical role of layer engineering and transport optimization in achieving higher efficiencies and improved overall photovoltaic performance. The optimized bifacial device achieved efficiencies of 28.38% for the front side and 28.27% for the back side. The findings of this thesis provide valuable insights bridging theoretical modeling and experimental applications, offering practical strategies for the design of efficient, stable, and sustainable perovskite solar cells, paving the way toward large-scale and environmentally friendly implementation.

Keywords: Perovskite Solar Cells (PSCs), SCAPS-1D Simulation, Flexible Photovoltaics, Bifacial PSCs, Renewable Energy.

Résumé :

Cette thèse de doctorat porte sur l'étude numérique et l'optimisation des cellules solaires à pérovskite (PSCs), reconnues comme l'une des technologies photovoltaïques de nouvelle génération les plus prometteuses. Grâce à leurs propriétés optoélectroniques exceptionnelles, leur bande interdite ajustable et leur faible coût de fabrication, les PSCs ont atteint des rendements de conversion de puissance (PCE) remarquables. Cependant, les problèmes de stabilité, les défis liés à l'industrialisation et la toxicité du plomb demeurent des obstacles majeurs à leur commercialisation. Dans ce travail, le simulateur SCAPS-1D a été utilisé comme outil numérique afin d'étudier la physique des dispositifs et d'évaluer les stratégies d'optimisation. Cette étude a été divisée en deux parties. La première partie s'est concentrée sur les cellules solaires à pérovskite flexibles, où nous avons étudié le rôle de nouveaux matériaux de transport de charges tels que les couches de transport de trous (HTLs) : ACZTSe, $CuBiS_3$, CZGS, D-PBTTT-14 et Se/Te-doped Cu_2O, ainsi que les couches de transport d'électrons (ETLs) : SnS_2, $BaZrS_3$, STO, WS_2 et ZrS_2. Dans ces cellules solaires, les défauts d'interface ont été examinés, où une couche de pérovskite bidimensionnelle (2D-PVK) a été ajoutée afin d'améliorer les effets interfaciaux. Le matériau CBz-PAI a été sélectionné comme couche de passivation interfaciale. De plus, le contact arrière a également été étudié, démontrant des améliorations significatives de l'extraction des charges, une réduction de la recombinaison et une amélioration de la stabilité interfaciale. La cellule solaire flexible optimisée a atteint un rendement de conversion de puissance de 27,17 %.La deuxième partie a porté sur les cellules solaires à pérovskite bifaciales (Bifacial PSCs), en analysant leurs performances sous illumination avant et arrière, tout en mettant en évidence le rôle critique de l'ingénierie des couches et de l'optimisation du transport des charges pour atteindre des rendements plus élevés et améliorer les performances photovoltaïques globales. Le dispositif bifacial optimisé a atteint des rendements de 28,38 % pour la face avant et de 28,27 % pour la face arrière. Les résultats de cette thèse apportent des perspectives précieuses reliant la modélisation théorique aux applications expérimentales, tout en proposant des stratégies pratiques pour la conception de cellules solaires à pérovskite efficaces, stables et durables, ouvrant ainsi la voie à des applications photovoltaïques à grande échelle et respectueuses de l'environnement.

Mots-clés : Cellules solaires à pérovskite (PSCs), Simulation SCAPS-1D, Photovoltaïque flexible, Cellules solaires bifaciales, Énergie renouvelable.

Acknowledgment

Praise be to Almighty God, whose blessings of faith, perseverance, and wisdom have enabled me to complete this work.

I wish to express my deepest gratitude to my supervisor, Prof. Abdennour Elmohri, from the Department of Mechanical Engineering, Faculty of Technologies, Dr. Yahia Fares University, Médéa, for his insightful guidance, unwavering support, and constructive supervision, which have been fundamental to the success of this thesis.

My sincere thanks are also extended to Dr. Selma Rabhi from Constantine 1 University, for her valuable scientific contributions and continuous encouragement, particularly in the preparation and publication of our joint research papers, which have significantly enriched this work.

I am profoundly grateful to my collaborators, Dr. Ibrahim Yaacoub Bouderbala from Ferhat Abbas University, Setif, and Dr. Mir Waqas Alam from King Faisal University, Saudi Arabia, for their fruitful cooperation and invaluable contributions to this research.

I would also like to acknowledge with great appreciation Prof. KEZRANE Mohamed, Director of the Laboratoire de Mécanique Physique et Modélisation Mathématique (LMP2M), University of Médéa, for his constant support and for providing an excellent research environment that greatly facilitated the accomplishment of this thesis.

My deepest appreciation further goes to the esteemed members of the jury: Prof. Zirari Mounir (President of the Jury, University of Médéa), Prof. Chiba Younes (Examiner, University of Médéa), and Dr. Bencherif Hichem (Examiner, University of Batna), for kindly accepting to evaluate this thesis and for their constructive comments and valuable suggestions, which have substantially improved the quality of this work.

Finally, I dedicate this modest achievement to my beloved family, whose prayers, patience, and unwavering encouragement have been a source of strength and inspiration throughout my academic journey.

List of publication and communication

The research work conducted in this doctoral thesis has resulted in the following international publication and conference communications:

1) International Publication

- **Mohamed Amine Benatallah**, Abdennour Elmohri, Yacoub Ibrahim Bouderbala, Mir Waqas Alam, Selma Rabbi.
  Boosting Efficiency in Flexible Perovskite Solar Cells with Novel HTLs and ETLs: A drift-diffusion numerical study of CBz-PAI Interlayers and MXene Back Contacts. Advanced Theory and Simulations.
  First published: 22 January 2025.
  DOI: https://doi.org/10.1002/adts.202401161

2) Conferences (International and National)

- **Mohamed Amine Benatallah**, Abdennour Elmohri, Selma Rabbi.
  Modeling and Optimization of Lead-Free $MASnBr_3$ Perovskite Solar Cells with FTO/ZnS/Spiro-OMeTAD Structure through Numerical Simulation.
  University of Chlef, Algeria.
  12 June 2025.
  https://www.univ-chlef.dz/mse25/

- **Mohamed Amine Benatallah**, Abdennour Elmohri, Selma Rabbi.
  Modelling of Eco-Friendly Based Perovskite Solar Cells ($MASnI_3$) for High Efficiency.
  Presented at the **3rd International Conference on Innovative Academic Studies (ICIAS)**, Konya, Turkey, 26–28 September 2023.
  https://www.icias.net/

- **Mohamed Amine Benatallah**, Abdennour Elmohri, Selma Rabbi.
  Performance Enhancement of $CsSnGeI_3$-Based Perovskite Solar Cells with FTO/ZnS and Spiro-OMeTAD Using Numerical Analysis (SCAPS 1D).
  Presented at the **5th International Conference on Engineering and Applied Natural Sciences**, Konya, Turkey, 25–26 August 2024.
  https://www.iceans.org/

- **Mohamed Amine Benatallah**, Abdennour Elmohri, Selma Rabbi.
  Optimization of FTO/ZnS/MASnI3/CZTS Perovskite Solar.
  Presented at the **5th International Conference on Engineering and Applied Natural Sciences**, Konya, Turkey, 25–26 August 2024.
  https://www.iceans.org/

Table of Contents

الملخص .....

Abstract .....

Résumé .....

Acknowledgment .....

List of publication and communication .....

Table of Contents .....

List of Figures .....

List of Tables .....

Nomenclature .....

Chapter I .....

General Context and the Evolution of Solar Energy Technologies **4**

Introduction **4**

I.1 The Increasing Global Demand for Energy **4**

I.2 Environmental Consequences: Pollution, CO_2 Emissions, and Climate Change **5**

I.3 The Transition to Renewable Energy Sources **6**

I.3.1 The importance of transitioning to clean and sustainable energy sources **6**

I.3.2 Solar Energy **7**

I.3.3 Advantages of Solar Energy: Abundance, Safety, and Environmental Friendliness **8**

I.4 Evolution of Solar Cell Generations **8**

I.4.1 First Generation **8**

I.4.2 Second Generation **11**

I.4.3 Third generation **12**

I.5 Perovskite Solar Cells: The Promising Third Generation **14**

I.5.1 The Historical Origin of Perovskite **14**

I.5.2 Crystallographic Structure of Perovskite Compounds **15**

I.5.3 Initial Use of Perovskite in Solar Cells **16**

I.5.4 Performance Evolution **17**

I.5.5 Advantages of Perovskite Solar Cells **18**

I.6 Fabrication Methods of Perovskite Solar Cells **19**

I.6.1. Perovskite Solar Cell Architectures **19**

I.6.2 Deposition Techniques **25**

I.7 Manufacturing Challenges of Perovskite Solar Cells **32**

I.8 Future Research Directions in Perovskite Solar Cells **33**

Conclusion 34
Chapter II .....
Introduction 36
II.1 The Physical and Methodological Framework of the SCAPS 1D Model 37
II.2 Analytical Modeling of Photovoltaic Performance Indicators in Solar Cells 39
Conclusion: 41
Chapter III .....
Introduction 43
III.1 Selection of Materials and Parameters for Simulation 44
III.1.1 Physical and Electronic Properties of Selected Materials 44
III.1.2 Detailed Description of Selected Materials 46
III.2 Results and Discussion 49
III.3 Impact of CBz-PAI Interlayer on Various ETLs and HTLs-Based FPSCs Performance 52
III.6 Effect of Parasitic Resistances (Rs and Rsh) and Working Temperature on FPSC Performance 56
III.7 Impact of the Work Function of Back Contact on FPSC Performances 58
III.8 Optimized Device 59
Chapter IV .....
Bifacial Perovskite Solar Cells 64
Introduction 65
IV.1 Selection of Materials and Parameters for Simulation 66
IV.1.1 Physical and Electronic Properties of Selected Materials 66
IV.1.2 Detailed Description of Selected Materials 68
IV.2 Results and Discussion 70
IV.2.1 Energy Band Alignment and Its Influence on Device Performance 72
IV.2.2 Spectral Response Analysis through Quantum Efficiency (QE) Curves 73
IV.2.3 Influence of Layer Thickness on Photovoltaic Performance 75
IV.2.4 Influence of Total Defect Density (N_t) on Photovoltaic Performance 77
IV.2.5 Influence of Carrier Concentration of HTLs and ETLs on Photovoltaic Performance 79
IV.2.6 Influence of Temperature on Photovoltaic Parameters 80
IV.3 Final Optimized Devices 81
IV.3.1 Influence of Absorber Density on Charge Carrier Diffusion Length and Lifetime 83
IV.3.2 Electrical Impedance Analysis of Optimized Bifacial PSCs 84
IV.3.3 Comparative Photovoltaic Performance of Initial and Optimized Bifacial Perovskite Solar Cell Configurations 85
Conclusion 87

General Conclusion .....

References .....

Annex .....

SCAPS 1D Simulation Workflow and Functional Setup **108**

Zone 1 - Working Point Parameters **110**

Zone 2 - Series and Shunt Resistance Configuration: **111**

Zone 3 - Project Configuration and Action List Management: **112**

Zone 4 -Illumination and Spectrum Settings **113**

Zone 5 - Simulation Type and Parameter Range Definition **115**

Zone 6 - Setting Up the Solar Cell Structure (Set Problem) **117**

Zone 7 - Set Problem: Defining the Solar Cell Architecture and Its Components **119**

Zone 8- Batch & Record Panel **124**

Zone 9- Execution of Batch and Record Calculations **126**

Zone 10 - Results Display Interface (Results of Calculations) **127**

Zone 11 - Simulation Management and Program Control **134**

List of Figures

Chapter I .....

Figure I.1 Global Growth in Electricity Consumption (2022-2050) under Different Scenarios **5**

Figure I.2 Link between Fossil Fuel-Based Electricity Generation and Global CO_2 Emissions **6**

Figure I.3 Transition to Renewable Energy as a Strategic Pathway toward Sustainable Development **7**

Figure I.4 Solar Radiation and its Conversion into Electricity through Photovoltaic Cells **7**

Figure I.5 Image showing first-generation crystalline silicon solar cells, including monocrystalline (Mono-Si) (b) and polycrystalline (Poly-Si) types (a) **8**

Figure I.6 Structural and technical composition of first-generation cells **10**

Figure I.7 Second Generation Thin Film Solar Cells.....**11**

Figure I.8 Structural and technical composition of second-generation cells **12**

Figure I.9 Image showing third-generation Organic Solar Cells (OSCs) **13**

Figure I.10 Image showing third-generation Dye-Sensitized Solar Cells (DSSCs) **13**

Figure I.11 Perovskite Solar Cells (PSCs) **14**

Figure I.12 Image of the Mineralogical Form of Perovskite (Calcium Titanate, CaTiO3) **15**

Figure I.13 3D-Perovskite Crystal Structure (ABX3) **15**

Figure I.14 Surface Morphology of an FTO Substrate (Fluorine-doped Tin Oxide) **19**

Figure I.15 Surface Morphology of an FTO Substrate (Fluorine-doped Tin Oxide) **20**

Figure I.16 Schematic illustration for Spin Coating of perovskite films. **25**

Figure I.17 Schematic illustration for Centrifugal Sedimentation of perovskite films **26**

Figure I.18 Schematic illustration for blade coating of perovskite films **27**

Figure I.19 Schematic illustration for Spray Pyrolysis Deposition of perovskite films **28**

Figure I.20 Schematic illustration for Slot-Die Coating of Perovskite Films **30**

Figure I.21 Schematic illustration for Inkjet Printing of Perovskite Films **31**

Chapter III.....

Figure III.1 Schematic architecture of the reference flexible perovskite solar cell structure without the CBz-PAI passivation interlayer, consisting of PET/AZO/ETL/$(FAPbI_3)_{0.77}$ $(MAPbBr_3)_{0.14}(CsPbI_3)_{0.09}$/HTL/MXene.....**50**

Figure III.2 a) Heat-map of average PCE FPSC devices on n-i-p structure (PET/AZO/ETL/$(FAPbI_3)0.77(MAPbBr_3)_{0.14}(CsPbI3)_{0.09}$/HTL/MXene) without CBz-PAI passivation interlayer, b) band diagram energy of AZO/ZrS_2/$(FAPbI_3)_{0.77}(MAPbBr_3)_{0.14}$ $(CsPbI_3)_{0.09}$/Se/Te: CuO_2/ MXene **50**

Figure III.3 Schematic architecture of the flexible perovskite solar cell structure with the CBz PAI passivation interlayer, consisting of PET/AZO/ETL/$(FAPbI_3)_{0.77}(MAPbBr_3)_{0.14}$ $(CsPbI_3)_{0.09}$/CBz-PAI/HTL/MXene**.....51**

Figure III.4 Heat-map of average PVK performance of FPSC devices on n-i-p structure (PET/AZO/ETL/$(FAPbI_3)_{0.77}(MAPbBr_3)_{0.14}(CsPbI_3)_{0.09}$/HTL/MXene) without passivation interlayer, a) PCE, b) V_{OC}, c) J_{SC}, and d) FF**.....53**

Figure III.5 Analysis of Photovoltaic Parameters (PCE, VOC, JSC, and FF) for a FPSC: Impact of Thickness Variation in 2D-PVK Passivation Interlayer (CBz PAI), ETL (ZrS_2), and HTL (CZGS), and on Solar Cell Efficiency **.....54**

Figure III.6 Contour mapping of PVK performances due to the effect of thickness and interface defect density Nt of 3D-PVK ($(FAPbI_3)_{0.77}$ $(MAPbBr_3)_{0.14}$ $(CsPbI_3)_{0.09}$) absorber layer **.....55**

Figure III.7 Contour mapping of PV performances due to the impact of R_S and R_{Sh}**.....57**

Figure III.8 Variation of FPSC PV parameters as a function of a) temperatures, b) Work function of different MXenes used for left (back) contact **.....59**

Figure III.9 a) J-V curves with PV parameters presented in the inset, b) QE, c) Mott–Schottky plot, and d) Nyquist plots of the initial (without CBz-PAI interlayer) and final (with CBz-PAI interlayer) FPSCs**.....60**

Chapter IV .....

Figure IV.1 Layered Structure of bifacial Perovskite Solar Cell : FTO Substrate, ETL ($BaSnO_3$, Nb_2O_5, ZnOS, Ag_2S), 3D-PVK Layer, 2D-PVK Interlayer Passivation, and HTL (Me-4PACz, $CuAlO_2$, $CuCrO_2$, CuPc, $NiCo_2O_4$, V_4O_5)**.....66**

Figure IV.2 a) Heat-maps for different configurations of bifacial perovskite solar cells **.....70**

Figure IV.3 Energy band diagram of a best device incorporating Multiple Materials: FTO, ETLs, 3D-PVK-$Cs_x(FA_{0.4}MA_{0.6})_{1-X}PbI_{2.8}Br_{0.2}$, 2D-PVK- $(PEA)_2Pb_2I_4$, and HTLs **.....73**

Figure IV.4 Quantum efficiency of a best device incorporating Multiple Materials: FTO, ETLs, 3D-PVK-$Cs_x(FA_{0.4}MA_{0.6})_{1-X}PbI_{2.8}Br_{0.2}$, 2D-PVK- $(PEA)_2Pb_2I_4$, and HTLs, the insets present the structure of each configurations as mentioned in Table IV.1**.....74**

Figure IV.5 Analysis of Photovoltaic Parameters (PCE, V_{OC}, J_{SC}, and FF) in PSCB Solar Cells: The Impact of Thickness Variation in Electron Transport Layers (ETLs), 3D-Perovskite $Cs_x(FA_{0.4}MA_{0.6})_{1-x}PbI_{2.8}Br_{0.2}$, 2D-Perovskite $(PEA)_2Pb_2I$, and Hole Transport Layers (HTLs) on Solar Cell Efficiency **.....79**

Figure IV.6 Analysis of Photovoltaic Parameters (PCE, V_{OC}, J_{SC}, and FF) in PSCB Solar Cells: The Impact of Total defect density N_t Variation in Electron Transport Layers ETLs, 3D-Perovskite $Cs_x(FA_{0.4}MA_{0.6})_{1-x}PbI_{2.8}Br_{0.2}$, 2D-Perovskite $(PEA)_2Pb_2I_4$, and Hole Transport Layers HTLs on Solar Cell Efficiency **.....78**

Figure IV.7 Contour Mapping of PCE (%) Performance as a Function of Shallow Donor Density (N_D) and Shallow Acceptor Density (N_A)Variations in Electron Transport Layers (ETLs) and Hole Transport Layers (HTLs)**.....79**

Figure IV.8 Analysis of Photovoltaic Parameters (PCE, V_{OC}, J_{SC}, and FF) in PSCB Solar Cells: The Impact of Temperature (°K) Variation in Electron Transport Layers (ETLs), 3D-Perovskite

$Cs_x(FA_{0.4}MA_{0.6})_{1-x}PbI_{2.8}Br_{0.2}$, 2D-Perovskite $(PEA)_2Pb_2I_4$, and Hole Transport Layers (HTLs) on Solar Cell Efficiency **81**

Figure IV.9 Curves Analyzing the Generation rate and Recombination rate of Photogenerated Carriers in Different Devices (I, II, III, IV) **82**

Figure IV.10 Carrier Diffusion Length (Ln, Ln) and Carrier Lifetime (T_n, T_p) as Functions of Defect Density (Nt) in the Optimal PSCB Solar Cell **83**

Figure IV.11 Nyquist impedance plot of PSCB with different types of an Optimized Device incorporating Multiple Materials: ETLs, 3D-PVK-Cs_x(FA0.4MA0.6)1-XPbI2.8Br0.2, 2D-PVK-(PEA)2Pb2I4, and HTLs **84**

Figure IV.12 I-V Curves of an Optimized Device Incorporating Multiple Materials: FTO, ETLs, 3D-PVK-Cs_x(FA0.4MA0.6)1-XPbI2.8Br0.2, 2D-PVK- (PEA)2Pb2I4, and HTLs **86**

Annex .....

Figure A.1 General view of the SCAPS 1D Action Panel interface **109**

Figure A.2 Division of the Action Panel into 10 functional zones, labeled for detailed explanation **109**

Figure A.3 Working Point Parameters Section in the SCAPS 1D Action Panel **110**

Figure A.4 Series and Shunt Resistance Configuration Panel in the SCAPS 1D Interface **112**

Figure A.5 Action List and Global Settings Panel in the SCAPS 1D Interface **113**

Figure A.6 Spectral Source and Illumination Direction Settings in SCAPS 1D **114**

Figure A.7 Definition of the Carrier Generation Profile G(x) in SCAPS 1D **115**

Figure A.8 Simulation Type and Sweep Range Configuration Panel in SCAPS 1D **117**

Figure A.9 Division of the "Set Problem" Window into Three Functional Zones in SCAPS 1D ..**120**

Figure A.10 Screenshot of the “Add Layer” window displaying the defined structure **120**

Figure A.11 Screenshot of the “Interface” window, focusing on a specific interface **121**

Figure A.12 Screenshot of the “Left Contact” window with visible work function setup and optical filtering options **121**

Figure A.13 Layer Structure Diagram of the Solar Cell in the SCAPS 1D Interface (Zone B). This figure illustrates the arrangement of layers, the doping type (indicated via color coding), and the direction of incident light **123**

Figure A.14 Zone 6-C serves as a control interface for Zone 6, allowing the addition of new elements, reinitialization, and saving of changes **124**

Figure A.15 This interface illustrates the configuration and execution of batch simulations for measurement and analysis **125**

Figure A.16 The interface illustrates the configuration and execution of measurement parameters (Record) to be analyzed **126**

Figure A.17 This screen displays the execution of the simulation according to the predefined Batch and Record settings **127**

Figure A.18 Shows the simulation results based on the previously selected test type, displaying only the relevant outputs without including all default results **128**

Figure A.19 Interface for configuring the initial settings prior to running the simulation in SCAPS 1D **129**

Figure A.20 Interface displaying the I-V parameter after completing the simulation in SCAPS 1D. **129**

Figure A.21 Interface displaying the C-V parameter after completing the simulation in SCAPS 1D. **130**

Figure A.22 Interface displaying the C-f parameter after completing the simulation in SCAPS 1D. **130**

Figure A.23 Interface displaying the QE parameter after completing the simulation in SCAPS 1D. **131**

Figure A.24 SCAPS 1D interface providing multiple saving tools, including saving graphs, saving data **131**

Figure A.25 SCAPS 1D interface illustrating the process of saving simulation plots as image files (e.g., PNG or JPEG) for documentation and analysis **132**

Figure A.26 interface showing the process of saving numerical results as a text file or in a designated folder for further processing with external tools such as Excel or Origin **132**

Figure A.27 SCAPS 1D interface illustrating the display of numerical results for direct preview without saving them to a file, with the option to copy and paste into external programs for further analysis **133**

Figure A.28 SCAPS 1D interface showing how to print the simulated curves, with options to adjust scaling and annotations to ensure clear presentation in scientific reports **133**

Figure A.29 This section enables the analysis of simulation data using the program's available tools for results visualization and interpretation **135**

List of Tables

Chapter I .....

Table I.1 Efficiency Evolution of Perovskite Solar Cells (2009 - 2026) **17**

Chapter III .....

Table III.1 Input parameters for TCOs, ETL, and 3D-PVK (FAPbI3)0.77(MAPbBr3)0.14 (CsPbI3)0.09 ..... **44-45**

Table III.2 Input parameters for 2D-PVK(CBz-PAI), and organic and inorganic HTLs **45**

Table III.3 Experimental and theoretical efficiencies for FPSCs reported in literature with a comparison of our study **61**

Chapter IV .....

Table IV.1 Input parameters for TCO, ETL, 3D-PVK(CSX(FA0.4 MA0.6)1-x PbI2.8 Br0.2), χ: electron affinity, ϵ: dielectric permittivity, CB: conduction band effective density of states, VB: valance band effective density of states, μp: electron mobility, μN: hole mobility **67**

Table IV.2 Input parameters for 2D-PVK (PEA2-Pb2I4), and organic and inorganic HTLs **67-68**

Table IV.3 Bifaciality factor of highest performance device configuration for both sides **71**

Table IV.4 Performance comparison of the final optimized device configuration (front and back illumination) against previously reported triple cation-devices **87**

Nomenclature

PVK	Perovskite
PSC	Perovskite solar cell
FPCs	Flexible Perovskite solar cell
FTEs	Flexible transparent electrodes
SC	Solar cell
OSCs	Organic Solar Cells
DSSCs	Dye-Sensitized Solar Cells
HTL	Hole Transport Layer
ETL	Electron Transport Layer
PET	Polyethylene terephthalate
TCO	Transparent Conducting Oxides
3D PVK	3D Perovskite absorber layer
2D PVK	2D Perovskite absorber layer
UV	Ultraviolet
PCE	Power Conversion Efficiency
J_{SC}	Short-Circuit Current Density
V_{OC}	Open-Circuit Voltage
FF	Fill Factor
C-V	Capacitance–Voltage
C-f	Capacitance–Frequency
QE	Quantum Efficiency
I-V	Current–Voltage characteristics
LD	Low dimensional
MHP	Metal-halide perovskite
MXene	2D transition metal carbides/nitrides (e.g., Ti_3C_2Tx)
Eg	Energy Band Gap
Xe	Electron Affinity
ϵ_r	Relative Permittivity (Dielectric Constant)
C_b	Conduction Band
V_b	Valence Band
μ_n	Electron Mobility
μ_p	Hole Mobility
N_D	Donor Density
N_A	Acceptor Density
Nt	Trap Density
FA	Formamidinium (cation in perovskites)
MA	Methylammonium (cation in perovskites)
Cs	Cesium (cation in perovskites)
DMF	Dimethylformamide

DMSO	Dimethyl Sulfoxide
GBL	Gamma-Butyrolactone
PI	Polyimide
R2R	Roll-to-Roll (fabrication technique)
ABX_3	Generic perovskite crystal structure (A: cation, B: metal cation, X: halide anion)
AC	Alternating Current
ACS	American Chemical Society
ACZTSe	Ag-Cu-Zn-Ti-Se (quaternary compound HTL material)
AM1	Air Mass 1 (solar spectrum reference condition)
AZO	Aluminum-doped Zinc Oxide
$BaZrS_3$	Barium Zirconium Sulfide
CBz-PAI	Carbazole-based Polyarylimide (interlayer material)
CZGS	Cu_2ZnGeS_4 (semiconductor material)
$CuBiS_3$	Copper Bismuth Sulfide
D-PBTTT-14	Conjugated Polymer (semiconducting material)
R_s	Series Resistance
R_{sh}	Shunt Resistance
SCAPS	Solar Cell Capacitance Simulator
SEM	Scanning Electron Microscopy
SRH	Shockley-Read-Hall (recombination model)
STO	Strontium Titanate ($SrTiO_3$)
SnS_2	Tin Disulfide
TCO	Transparent Conducting Oxide
TEM	Transmission Electron Microscopy
XRD	X-ray Diffraction
ZrS_2	Zirconium Disulfide
Bf	Bifaciality Factor
Rct	Charge Transfer Resistance
Rrec	Recombination Resistance
C	Capacitance
SAM	Self-Assembled Monolayer
Nyquist Plot	Electrical Impedance Representation
τ	Carrier Lifetime
Ln, Lp	Diffusion Length of electrons/holes
Eg(opt)	Optimized Energy Band Gap
ΔV	Voltage Deficit ($V_{OC} - Eg/q$)
IEA	International Energy Agency
IAEA	International Atomic Energy Agency
BP	Beyond Petroleum
RFF	Resources for the Future

General Introduction

Context

The global energy sector is undergoing a profound transformation as humanity seeks sustainable alternatives to fossil fuels, which are associated with greenhouse gas emissions, climate change, and resource depletion.[1] Among renewable energy resources, solar energy has emerged as one of the most promising solutions due to its abundance and ability to provide long-term low-carbon electricity.[2] Photovoltaic (PV) technologies have significantly evolved across different generations, from crystalline silicon solar cells (first generation) and thin-film technologies (second generation) to organic and dye-sensitized solar cells (third generation). Within this technological evolution, metal-halide perovskite solar cells (PSCs) have rapidly emerged as highly promising next-generation photovoltaic devices owing to their exceptional optoelectronic properties, tunable bandgap, low-cost fabrication processes, and remarkable progress in power conversion efficiencies (PCEs).[3-5]

Problem Statement

Despite their extraordinary potential, PSCs still face several critical challenges that limit their large-scale commercialization. These challenges include instability under thermal stress, humidity, and ultraviolet irradiation, as well as the toxicity associated with lead-based compositions and the difficulty of achieving reproducibility and industrial scalability.[6-7] Moreover, interfacial recombination and defect-induced non-radiative losses remain major limiting factors affecting both efficiency and long-term operational stability.[8] Addressing these limitations requires a deeper understanding of the underlying physical mechanisms and the development of advanced material engineering and device optimization strategies.

Motivation

The motivation behind this doctoral research arises from the urgent need to develop photovoltaic devices that are not only highly efficient but also stable and environmentally sustainable. Numerical simulation has become an essential approach for understanding charge transport mechanisms, recombination dynamics, and interfacial effects in PSCs.[9] In this context, the SCAPS 1D simulator provides a reliable and powerful platform for investigating the physical behavior of perovskite solar cells and optimizing their structural and material parameters under various operating conditions. By relying on advanced numerical modeling

rather than purely experimental trial-and-error approaches, this work aims to accelerate the development of optimized perovskite solar cell architectures with enhanced efficiency, reduced recombination losses, and improved device stability.

Research Contributions

This doctoral thesis contributes to the advancement of perovskite photovoltaic technology through several important achievements:

- Investigation of novel hole transport layers (HTLs) and electron transport layers (ETLs) to improve charge extraction and suppress recombination losses.
- Implementation of CBz-PAI interfacial layers to enhance interface quality, reduce defect-assisted recombination, and improve carrier transport dynamics.
- Exploration of MXene-based back contacts as alternative electrodes with improved conductivity, favorable energy-level alignment, and enhanced device stability.
- Development of comprehensive SCAPS-1D simulation methodologies to analyze the influence of material properties and structural parameters on photovoltaic performance.
- Numerical optimization of bifacial inverted PSCs incorporating hybrid 2D/3D perovskite absorbers through detailed investigations of thickness variation, defect density, carrier concentration, temperature effects, and overall device stability.

Organization of the Thesis

This dissertation is organized into four scientific chapters followed by a general conclusion and perspectives:

- **Chapter I** presents the global context of the energy transition, the evolution of photovoltaic technologies, and the emergence of perovskite solar cells.
- **Chapter II** presents the physical and methodological framework of the SCAPS-1D simulator, including the fundamental semiconductor equations, drift–diffusion modeling, and photovoltaic performance analysis used throughout this thesis.
- **Chapter III** focuses on the numerical investigation and optimization of flexible perovskite solar cells incorporating novel HTLs, ETLs, CBz-PAI interfacial engineering, and MXene-based back contacts, with detailed analysis of their influence on photovoltaic performance. [10]

- **Chapter IV** is devoted to the optimization and numerical analysis of bifacial perovskite solar cells based on hybrid 2D/3D absorbers under front-side and rear-side illumination conditions, including investigations of thickness variation, defect density, carrier concentration, temperature effects, generation–recombination mechanisms, and impedance characteristics.[11]
- **General Conclusion and Perspectives** summarizes the principal findings of this work, discusses the remaining scientific challenges, and proposes future research directions toward efficient, stable, and sustainable perovskite solar cells.
- **Annex** presents complementary information related to the SCAPS-1D simulation environment, software interface configuration, implemented numerical parameters, and additional simulation details used throughout this work.

Chapter

I

General Context and the Evolution of Solar Energy Technologies

Introduction

The increasing global demand for clean and sustainable energy has accelerated the development of renewable energy technologies, particularly photovoltaic (PV) systems. Over the past decades, photovoltaic technologies have undergone remarkable evolution, progressing from conventional silicon-based solar cells to advanced thin-film and emerging perovskite solar cells. This evolution has been mainly driven by the need to improve power conversion efficiency, reduce manufacturing costs, and develop environmentally sustainable energy solutions.

I.1 The Increasing Global Demand for Energy

In recent years, the global demand for electricity has witnessed an unprecedented and significant surge. This growth is primarily driven by the rapid electrification of industrial sectors and transportation systems, the rising reliance on digital infrastructure and data centers, and the widespread adoption of smart technologies. Global energy outlooks suggest that electricity consumption is expected to continue its upward trajectory over the next three decades.

According to the International Energy Agency (IEA), in its Net Zero Emissions by 2050 scenario,[12] global electricity consumption is projected to increase from approximately 28,661 terawatt-hours (TWh) in 2022 to around 55,000 TWh by 2050 representing a 92% rise. Under the Stated Policies Scenario, the projected consumption reaches about 45,000 TWh by 2050, indicating a 57% increase.[13]

Similarly, BP's Beyond Petroleum Accelerated scenario estimates global demand to fall between 50,000 and 55,000 TWh.[14] The International Atomic Energy Agency (IAEA) also forecasts that consumption could exceed 53,000 TWh if nuclear energy adoption is expanded.[15] Resources for the Future (RFF) predicts a global electricity demand of approximately 51,000 TWh,[16] while Statista presents a more optimistic scenario, projecting consumption to reach 77,000 TWh by 2050 an increase of 169% compared to 2022 levels.[17]

These projections clearly indicate a consistent and robust rise in global electricity consumption. Emerging economies such as Algeria are expected to follow this trend, with substantial growth in electricity demand anticipated. This growth is closely linked to global dynamics, including population expansion, urban development, and increased reliance on modern technologies.

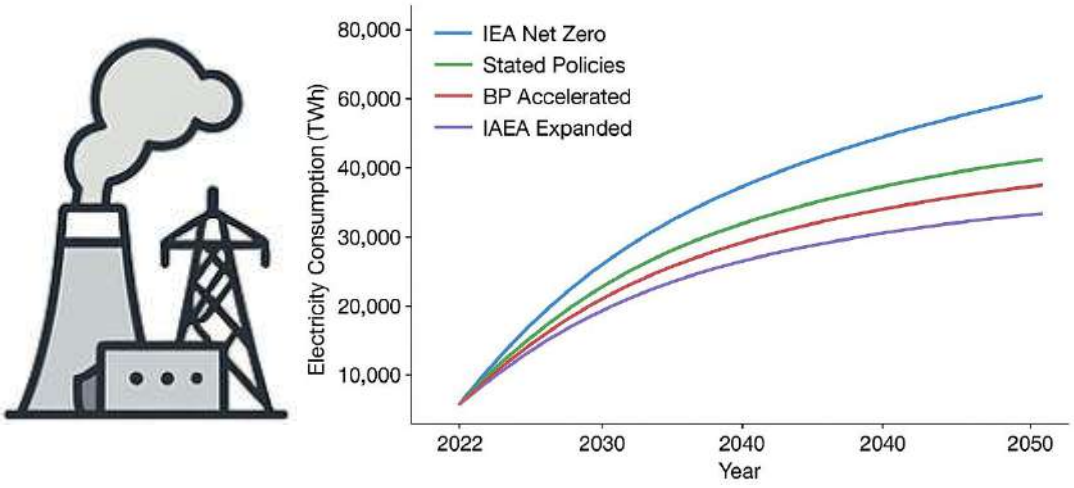


Figure I.1 Global Growth in Electricity Consumption (2022-2050) under Different Scenarios.

I.2 Environmental Consequences: Pollution, CO_2 Emissions, and Climate Change

It is important to emphasize that the global increase in electricity consumption is not solely driven by the demands of economic growth and development. It is also closely linked to rising levels of environmental pollution particularly when electricity generation relies on conventional sources such as coal, oil, and natural gas see Figure I.2.

Recent statistics indicate that the world remains heavily dependent on fossil fuels to meet its energy needs. In 2023, fossil fuel sources accounted for over 60% of global electricity production, despite significant growth in renewable energy deployment.[18] At the broader level of primary energy consumption, fossil fuels still represent approximately 80% of the total global energy mix**,** highlighting the persistent dominance of carbon-intensive sources.

In terms of emissions, it is estimated that around 91% of global carbon dioxide (CO_2) emissions originate from fossil fuel combustion, including oil, gas, and coal. According to data from the International Energy Agency IEA and related databases,[19] coal alone is responsible for nearly 46% of CO_2 emissions resulting from fossil fuel use .[20]

Despite global efforts to transition toward cleaner energy systems, the 2019 World Energy Report showed continued increases in fossil fuel usage: electricity generation from natural gas rose by +4%, while coal-based electricity grew by +2% in that year alone. This trend

underscores the ongoing reliance on fossil fuels, even amid a growing push for clean energy transitions (IEA, 2019).[16]

Furthermore, IEA estimates suggest that oil and gas operations are responsible for approximately 15% of total energy-related greenhouse gas emissions**,** amounting to nearly 5.1 billion metric tons of CO_2 equivalent annually.[21]

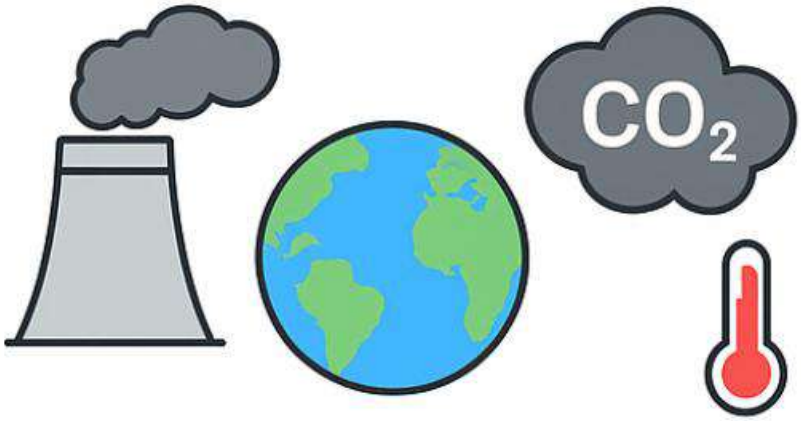


Figure I.2 Link between Fossil Fuel-Based Electricity Generation and Global CO_2 Emissions.

I.3 The Transition to Renewable Energy Sources

I.3.1 The importance of transitioning to clean and sustainable energy sources

The transition to sustainable energy represents a pivotal strategic choice for achieving an effective balance between economic growth demands and the preservation of ecological system stability**.** It contributes to the reduction of carbon emissions, the enhancement of energy security, and the decreased reliance on conventional fossil fuel sources. By adopting renewable energy sources such as solar, wind, and hydropower, countries can establish a low-carbon development model, improve air quality, and mitigate the accelerating impacts of climate change, as presented in Figure I.3. Clean energy also offers a vital opportunity to foster technological innovation, particularly in energy storage and smart energy systems, while generating sustainable employment within the green economy. Thus, the shift toward sustainable energy is not merely an environmental option but a strategic imperative to ensure a safer and more resilient future for coming generations.



Figure I.3 Transition to Renewable Energy as a Strategic Pathway toward Sustainable Development.

I.3.2 Solar Energy

Solar energy is one of the most abundant renewable energy sources on Earth**.** The planet receives over 173,000 terawatts of solar radiation each day more than 10,000 times the world's total energy consumption. According to the Handbook of Solar Energy,[22] the effective utilization of solar energy depends on the characteristics of solar radiation, including intensity, duration, and angle of incidence, making it a clean and sustainable energy source. In recent decades, significant advances in photovoltaic conversion technologies have enhanced the efficiency and reliability of solar energy systems, strengthening their role in the global transition toward sustainable energy production.



Figure I.4 Solar Radiation and its Conversion into Electricity through Photovoltaic Cells.

I.3.3 Advantages of Solar Energy: Abundance, Safety, and Environmental Friendliness

Solar energy is classified as a source free from the chemical hazards and flammability risks typically associated with fossil fuels. It offers a sustainable solution with no harmful emissions or air pollutants, making it both environmentally and human-health friendly.[23] From an ecological perspective, increased adoption of solar energy has been linked to significant reductions in carbon dioxide emissions, contributing to improved air quality and climate stability.[24] On average, each kilowatt-hour of electricity produced from solar energy prevents a substantial amount of CO_2 compared to coal-based generation. Therefore, solar energy is not merely a technical alternative, but a fundamental pillar of the global energy transition thanks to its natural abundance, environmental safety, and tangible impact in combating climate change.

I.4 Evolution of Solar Cell Generations

I.4.1 First Generation

A)- Crystalline Silicon Cells (Monocrystalline and Polycrystalline)

First-generation solar cells, based on crystalline silicon (c-Si) technology, represent the foundational architecture of conventional photovoltaic systems. This generation includes two main types:

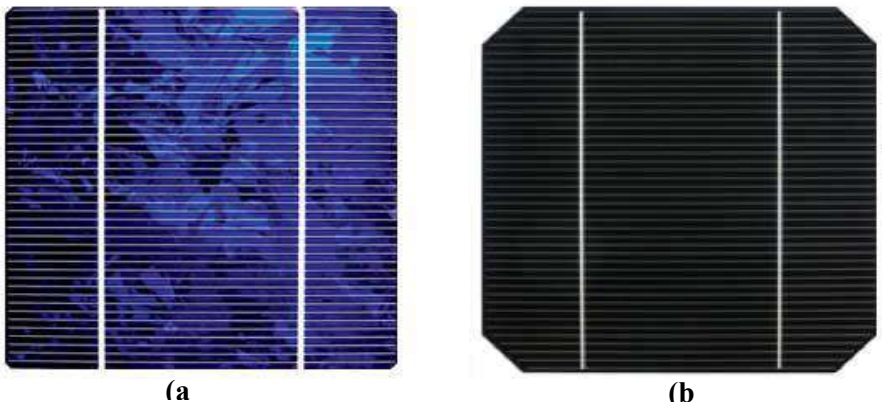


Figure I.5 Image showing first-generation crystalline silicon solar cells, including monocrystalline (Mono-Si) (b) and polycrystalline (Poly-Si) types (a).[25]

Monocrystalline cells are typically manufactured using the Czochralski process, which produces highly uniform, single-crystal silicon ingots see Figure I.5. This results in minimal

structural defects and reduced grain boundaries,[26] enabling more efficient charge carrier transport and higher photovoltaic conversion efficiency see Figure I.5.

In contrast, polycrystalline cells are produced via Directional Solidification, a technique that leads to multiple crystalline grains within a single wafer. The presence of grain boundaries in poly-Si increases the likelihood of electron-hole recombination, thereby slightly reducing the electrical performance compared to mono-Si counterparts.

From a performance perspective, monocrystalline silicon solar cells typically achieve commercial efficiencies ranging from 20% to 24%, while advanced silicon technologies such as TOP Con, HJT, and back-contact architectures have demonstrated efficiencies exceeding 27% under optimized laboratory conditions.[27-28] These improvements are mainly achieved through enhanced surface passivation, reduced charge carrier recombination, and improved carrier transport mechanisms. Polycrystalline silicon solar cells, although generally less efficient, typically operate within an efficiency range of 15% to 19%. Despite the presence of grain boundaries that increase charge carrier recombination, polycrystalline technologies remain attractive for large-scale photovoltaic applications due to their lower manufacturing cost and industrial maturity.[27]

B)- Technical Composition and Layer Structure

First-generation solar cells rely on a conventional yet refined structure based on crystalline silicon (c-Si) see Figure I.6, carefully engineered to maximize photovoltaic conversion efficiency. These cells typically consist of a semiconductor (p - n) junction, where a p-type silicon base is combined with a thin n-type emitter layer. This junction generates an internal electric field that facilitates the separation of photogenerated charge carriers upon light absorption.[29]

On the front surface, an anti-reflective coating commonly made of silicon nitride (S_iN_x) is applied to minimize reflective losses and enhance photon absorption. The collected charges are then extracted through a fine metallic grid, usually printed with silver (Ag), in the form of microscopic fingers designed to reduce shading while maintaining efficient conductivity.[30]

The rear side of the cell is coated with an aluminum (Al) layer that functions as a back contact and serves to reflect uncollected electrons back toward the active junction. This technique, known as Back Surface Field (BSF), improves carrier collection and reduces surface recombination losses.[31]

The fabrication of these cells requires high-temperature processing, typically ranging between 1000°C and 1450°C**,** to melt, crystallize, and refine the silicon ingots particularly for

monocrystalline cells produced using the Czochralski method.[32] Despite the thermal complexity of the manufacturing process, crystalline silicon cells demonstrate excellent electrical stability and reliable performance under a wide range of environmental conditions, making them an industrially robust and widely adopted technology.[33]

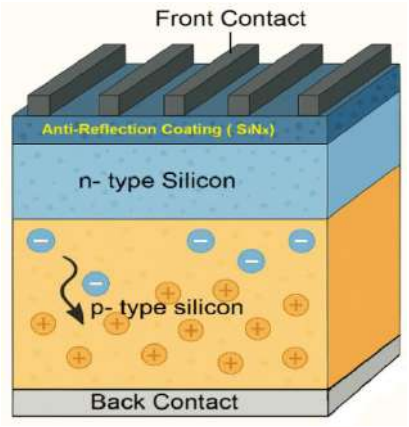


Figure I.6 Structural and technical composition of first-generation cells.

C)- The Environmental Dimension of First-Generation Silicon Solar Cell Manufacturing

While first-generation crystalline silicon solar cells offer relatively high photovoltaic conversion efficiencies typically ranging between 18% and 27% these advantages come with substantial environmental burdens associated with their manufacturing processes. The production of monocrystalline cells, in particular, demands temperatures exceeding 1400°C to melt and purify silicon, in addition to energy-intensive crystal pulling methods such as the Czochralski process.

According to Jammula et al. (2024),[24] the manufacturing phase is characterized by high embodied energy, defined as the total energy required to produce each watt of photovoltaic capacity. For crystalline silicon modules, this value ranges between 150 and 200 kWh per square meter of panel area, which significantly affects the net energy balance and delays the energy payback period. From an environmental perspective, the purification of silicon generates hazardous chemical byproducts, most notably silicon tetrachloride ($SiCl_4$), a toxic compound that requires careful containment and disposal to avoid soil and water contamination. Additionally, the use of fluorinated gases, such as sulfur hexafluoride (SF_6) and nitrogen trifluoride (NF_3), in cleaning and etching processes contributes significantly to the carbon footprint, as these gases have global warming potentials thousands of times higher than CO_2.

Another notable issue is the reliance on precious metals, particularly silver (Ag), for front-side metallization. The extraction and processing of silver not only raise material costs but also pose

concerns regarding long-term material sustainability, especially in light of increasing global deployment. A study by Korichi et al.[34] (2025) estimates that the metallization stage alone may account for up to 15% of the total environmental impact of a silicon solar cell.

Despite their long operational lifespan often exceeding 25 years the current infrastructure for end-of-life solar panel recycling remains underdeveloped. As the global adoption of first-generation PV technologies continues to accelerate, this creates a mounting future waste management challenge and raises concerns over the environmental lifecycle of these systems.

I.4.2 Second Generation

A)- Solar Cells for Thin-Film Technologies

Second-generation solar cells are based on thin-film photovoltaic technologies, developed as alternatives to conventional crystalline silicon solar cells in order to reduce production costs, material consumption, and energy usage. The principal materials employed in this generation include cadmium telluride (CdTe), copper indium gallium selenide (CIGS), and amorphous silicon (a-Si:H). These technologies offer several advantages, including flexibility, lightweight structures, and compatibility with low-cost substrates such as glass and plastic, making them highly suitable for building-integrated photovoltaics (BIPV), portable electronic devices, and aerospace applications. In terms of performance, commercial CdTe and CIGS solar cells typically achieve efficiencies ranging from 15% to 20%, while laboratory-scale devices have demonstrated efficiencies exceeding 23% for CIGS and approximately 22% for CdTe according to recent NREL efficiency reports.[27-28] Although amorphous silicon (a-Si:H) solar cells generally exhibit lower efficiencies, typically in the range of 8% to 12%, they remain attractive due to their low manufacturing cost and relatively good performance under low-irradiance conditions.



Figure I.7 Second Generation Thin Film Solar Cells.[35]

B)- Structure of Thin-Film CdTe and CIGS Solar Cells

Second-generation solar cells consist of extremely thin semiconductor layers, typically between 1 and 3 micrometers, significantly thinner than the ~150–200 µm layers used in crystalline silicon cells. A typical CdTe solar cell structure includes the following layers as presented in Figure I.8:

(1) - Glass or polymer substrate,
(2) - Transparent conductive oxide (TCO), often indium tin oxide (ITO),
(3) - CdS buffer layer,
(4) - CdTe absorber layer,
(5) - Metal back contact (usually graphite, Mo, or Cu).

Compared to crystalline silicon, these thin-film processes require lower processing temperatures (often below 500°C), allowing for reduced embodied energy and material cost. According to Maalouf et al. (2023) ,[36] the overall embodied energy of thin-film technologies is up to 50% lower than that of silicon-based counterparts, while enabling scalable large-area production.

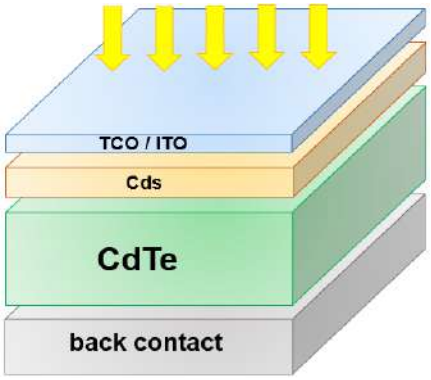


Figure I.8 Structural and technical composition of second-generation cells.

I.4.3 Third generation

Third-generation solar cells are specifically developed to overcome the fundamental efficiency ceiling of conventional single-junction silicon photovoltaics, known as the Shockley–Queisser limit (~33%). At the same time, they seek to mitigate challenges related to high manufacturing costs and the environmental footprint of large-scale production.[37] The motivation behind this generation is to create lightweight, cost-effective, and environmentally sustainable alternatives that broaden the applicability of solar energy (Giannouli, 2021; Shah et al., 2023).[38] Unlike the earlier generations, third-generation concepts are based on novel physical principles and

material innovations, such as multi-junction cells, quantum dots, hot-carrier extraction, and perovskite photovoltaics. This category therefore encompasses several advanced technologies, most notably:

A)- Organic Solar Cells (OSCs)

Utilize conductive polymers or small organic molecules as the active light-absorbing layers. OSCs are lightweight, flexible, and compatible with low-temperature processing methods such as inkjet printing or roll to roll coating, with current lab efficiencies reaching ~19.4%).[27]

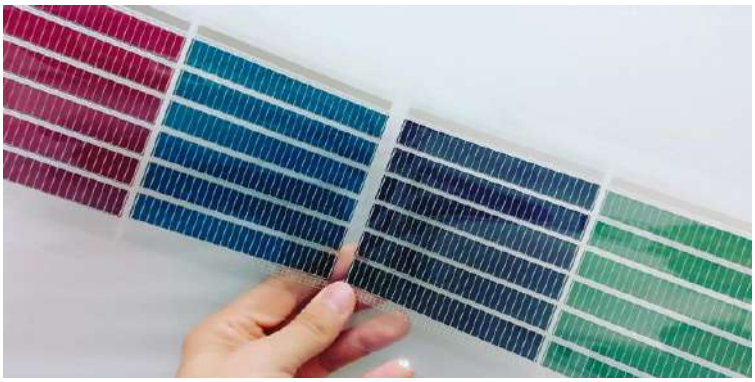


Figure I.9 Image showing third-generation Organic Solar Cells (OSCs).[39]

B)- Dye-Sensitized Solar Cells (DSSCs)

Based on photo-sensitizing dyes adsorbed onto a porous semiconductor (typically TiO_2), DSSCs are cost-effective and easily manufactured, with efficiencies ranging from 12% to 13%, but suffer from electrolyte instability and limited long-term performance the Figure I.10.[27]



Figure I.10 Image showing third-generation Dye-Sensitized Solar Cells (DSSCs).[40]

C)- Perovskite Solar Cells (PSCs)

Incorporate hybrid organic - inorganic perovskite materials (e.g., $CH_3NH_3PbI_3$) and have demonstrated exceptional power conversion efficiencies exceeding 27.3% in lab settings by 2026.[27] Tandem architectures (e.g., perovskite–silicon) have recently exceeded 31.25% efficiency (Qin et al., 2023).[41] PSCs also benefit from low-temperature fabrication (<150 °C) and solution-processability.

These technologies represent a significant departure from silicon-based devices by enabling low-energy manufacturing, flexible substrates, and printable large-area modules. They can reduce embodied energy by up to 60**%** compared to first-generation cells (Di Giacomo et al., 2016) see Figure I.3.[42]

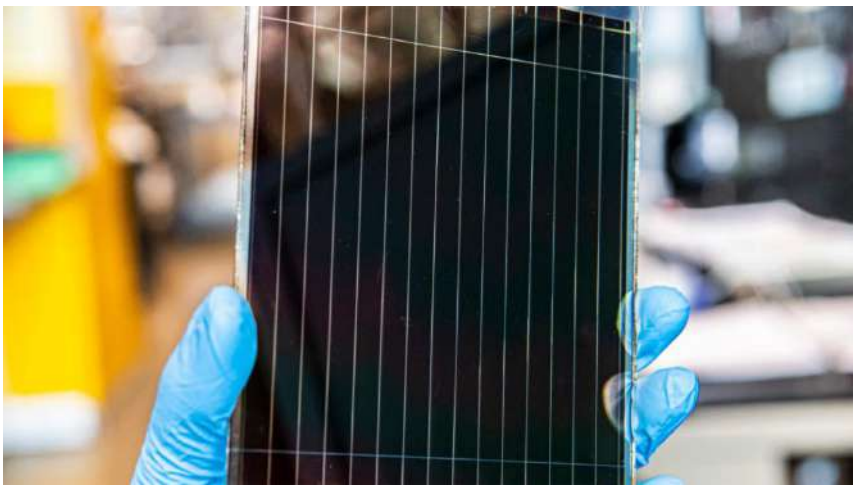


Figure I.11 Perovskite Solar Cells (PSCs).[43]

I.5 Perovskite Solar Cells: The Promising Third Generation

I.5.1 The Historical Origin of Perovskite

The term perovskite originates from the Russian mineralogist Lev Perovski, who was honored in 1839 when the mineral $CaTiO_3$ was discovered in the Ural Mountains (Russia) by the German chemist Gustav Rose and named after him.[44] However, significant progress in understanding the crystallographic structure of perovskite materials began in the 1940**s**, when Helen Dick McGaw published the first detailed description of the orthorhombic symmetry of $CaTiO_3$ see Figure I.4.[45] Since then, perovskite-type compounds have become a major subject of research in solid-state chemistry, particularly for their applications in ferroelectrics, electronic devices, catalysis, and more recently, solar photovoltaics.[46]



Figure I.12 Image of the Mineralogical Form of Perovskite (Calcium Titanate, $CaTiO_3$).

I.5.2 Crystallographic Structure of Perovskite Compounds

The crystal structure of perovskite compounds used in solar cells is based on the general formula ABX_3, where A is a monovalent cation (e.g., $CH_3NH_3^+$ or Cs^+), B is a divalent metal cation (e.g., Pb^{2+} or Sn^{2+}), and X is a halide anion (I^-, Br^-, or Cl^-) .[47] In the ideal configuration, the B-site cation is located at the center of an octahedron formed by six X anions, while the A-site cation occupies the interstitial voids between these octahedra to maintain charge balance. This yields a highly symmetric cubic perovskite structure with space group Pm3m as presented in Figure I.13.

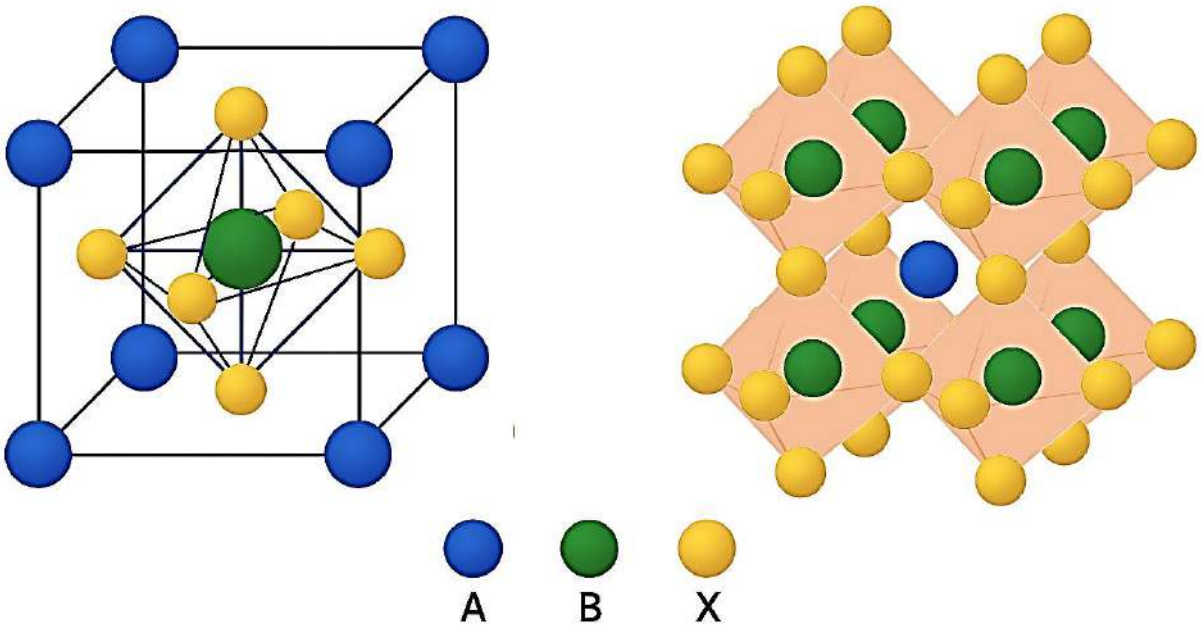


Figure I.13 3D-Perovskite Crystal Structure (ABX_3).

However, in most hybrid organic–inorganic perovskites, size mismatch among the ions causes structural distortions, leading to tetragonal or orthorhombic phases at room temperature.
To predict and assess the geometric stability of perovskite materials, the Goldschmidt tolerance factor (t) is used, calculated as:

$$t = \frac{r_A + r_x}{\sqrt{2}\,(r_B + r_x)} \quad (1)$$

A tolerance factor close to 1.00 indicates ideal cubic symmetry, while values significantly below 1.00 predict lower-symmetry distortions. For example, the widely studied perovskite $CH_3NH_3PbI_3$ has a tolerance factor of approximately 0.91, resulting in a stable tetragonal phase at ambient temperature and a transition to the cubic phase when heated above 330 K .[48]

I.5.3 Initial Use of Perovskite in Solar Cells

Although perovskite ($CaTiO_3$) has been known since its discovery by Gustav Rose in 1839, its application in photovoltaic technologies only emerged in recent decades. In 2009, Kojima et al. introduced a major scientific advancement by employing methylammonium lead iodide ($CH_3NH_3PbI_3$) as a light-absorbing material in dye-sensitized solar cells (DSSCs), achieving a power conversion efficiency (PCE) of 3.8%. However, the use of liquid electrolytes resulted in limited thermal and chemical stability, thereby restricting the practical potential of these early devices (Kojima et al., 2009; Jena et al., 2019).[46]
By 2012, the introduction of a solid-state hole transport material (HTM) such as Spiro-OMeTAD in place of the liquid electrolyte marked a turning point. This development gave rise to solid-state perovskite solar cells (PSCs), and efficiency increased significantly to 9.7%, opening the door to a new era of research and development in photovoltaic science (Kim et al., 2012; Miyasaka et al., 2022).[49]
Subsequent improvements in crystal structure, defect passivation, and interfacial layer engineering contributed to the dramatic rise in efficiency. Single-junction perovskite cells have now achieved certified efficiencies of 25.8%, while tandem perovskite–silicon devices reached a record 33.9% as of 2023, approaching the theoretical Shockley-Queisser limit (NREL, 2023).[50]

Table I.1 Efficiency Evolution of Perovskite Solar Cells (2009 - 2026):

Year	Cell Type and Innovation	Power Conversion Efficiency (PCE)	Reference
2009	Dye-Sensitized Solar Cell (DSSC) with $CH_3NH_3PbI_3$	3.8%	[46]
2012	Solid-State PSC using Spiro-OMeTAD	9.7%	[49]
2014	PSC with mixed halides and layered architecture	16.2%	[51]
2016	Enhanced HTM and interfacial contact layers	20.1%	[52]
2018	Crystal edge passivation for improved performance	22.7%	[53]
2020	Thermally stable PSC with extended durability	24.5%	[54]
2023	Monolithic Tandem (Perovskite–Silicon) Cell	33.9%	[55]
2026	Advanced Perovskite/Silicon Tandem Solar Cell	**34.02%**	[56]

I.5.4 Performance Evolution

Since the first implementation of CH3NH3PbI3 as a light-absorbing material in 2009, perovskite solar cells (PSCs) have demonstrated an unprecedented trajectory of efficiency improvement. Starting from a modest 3.8% power conversion efficiency (PCE) in dye-sensitized configurations, PSCs reached over 25.8% in certified single-junction devices and surpassed 33% in tandem configurations by 2023 (Kojima et al., 2009; Qin et al., 2023).[57] More recently, advanced perovskite/silicon tandem solar cells achieved reverse-scan efficiencies up to 34.02% in 2026, highlighting the exceptional potential of PSC technologies for next-generation high-efficiency photovoltaic applications.[56]

This rapid advancement is largely attributed to innovations in both material chemistry and architectural design. Chemically engineered compositions especially triple-cation systems incorporating formamidinium (FA^+), methylammonium (MA^+), and cesium (Cs^+) have enabled improved thermal and moisture stability and broader spectral absorption (Saliba et al., 2016; Jena et al., 2019).[43-44] Architecturally, the evolution from mesoscopic to planar and ultimately to monolithic tandem structures has significantly enhanced charge collection efficiency and minimized energy losses (Correa-Baena et al., 2017).[59]

Moreover, the engineering of interfacial layers between the perovskite absorber and transport layers (ETL/HTL) has played a vital role in reducing non-radiative recombination and extending device longevity (Seo et al., 2016).[60]

Taken together, the dramatic rise in PCE within just over a decade marks one of the most rapid developments in photovoltaic history. This exceptional performance growth underscores the global interest in PSCs as promising candidates for next-generation solar technology, leading into the next section on why perovskite is increasingly favored over conventional materials.

I.5.5 Advantages of Perovskite Solar Cells

The global momentum behind perovskite solar cells (PSCs) is driven by a synergistic set of advantages that position them at the forefront of third-generation photovoltaic technologies. Beyond their record-setting efficiencies, PSCs offer unique benefits in terms of cost-effectiveness, fabrication versatility, structural flexibility, and compositional tunability.

From a performance perspective, PSCs have reached certified power conversion efficiencies (PCEs) exceeding 27.3% in single-junction cells and over 33.9% in tandem perovskite silicon architectures values that approach the Shockley Queisser theoretical limit (Qin et al., 2023; NREL, 2023).[50] These achievements stem from outstanding optoelectronic properties, including high absorption coefficients ($>10^5$ cm^{-1}), long charge diffusion lengths (on the order of micrometers), and low exciton binding energies (~20 meV), which facilitate efficient carrier generation and separation even in ultrathin layers (Jena et al., 2019).[59]

In terms of manufacturability, PSCs offer significant advantages over conventional silicon cells. Whereas silicon requires energy-intensive processing (>1000 °C) and high-purity crystallization, perovskite films can be fabricated at low temperatures (<150 °C) using solution-based methods. According to life cycle assessments, the embodied energy of PSCs can be as low as 20% of that of silicon, and their energy payback time (EPBT) can be less than one year, depending on module architecture and operational conditions (Sreedev & Rakhesh, 2024; Zhao, 2025).[61]

Their compatibility with solution-processable deposition techniques such as inkjet printing, spray coating, slot-die coating, and spin coating enables cost-effective, high-throughput manufacturing. Gorter et al. (2025) demonstrated that roll-to-roll fabrication of PSC modules can be achieved at industrially relevant speeds of up to 3 meters per minute, significantly reducing capital costs and accelerating market adoption.[62]

Mechanically, the low processing temperature and thin-film structure of perovskites allow their integration on flexible polymeric substrates (e.g., PET, PEN, PI), opening pathways for next-generation applications including wearable electronics, building-integrated photovoltaics (BIPV), and portable energy systems. Castriotta et al. (2025) reported less than 3% degradation

in performance after 1000 bending cycles,[63] underscoring the structural robustness of flexible PSC modules.

Furthermore, perovskite materials exhibit remarkable compositional versatility. By tuning A-site cations (e.g., FA^+, MA^+, Cs^+) and halide anions (I^-, Br^-), researchers have engineered bandgaps ranging from 1.2 to 2.3 eV, enabling tailored absorption for single-junction, tandem, or semi-transparent applications. Advanced strategies, such as quantum dot engineering or Mn^{2+} doping, have further improved phase stability and optoelectronic performance under real-world conditions (Zhao, 2025).[64]

I.6 Fabrication Methods of Perovskite Solar Cells

I.6.1. Perovskite Solar Cell Architectures

Perovskite solar cells (PSCs) are generally classified into two principal device architectures: the conventional N-I-P structure and the inverted P-I-N structure. In the conventional N-I-P configuration, the electron transport layer (ETL) is deposited directly on the transparent conductive substrate, followed by the perovskite absorber layer and the hole transport layer (HTL). This architecture has demonstrated excellent photovoltaic performance and is widely employed in high-efficiency PSCs.

In contrast, the inverted P-I-N structure positions the HTL beneath the perovskite layer and the ETL above the absorber layer see Figure I.14. Compared to N-I-P devices, P-I-N architectures generally exhibit lower hysteresis, improved interfacial stability, and superior compatibility with flexible photovoltaic applications due to their low-temperature fabrication processes. The selection of device architecture strongly affects charge transport mechanisms, recombination dynamics, operational stability, and overall photovoltaic performance.[65-66]

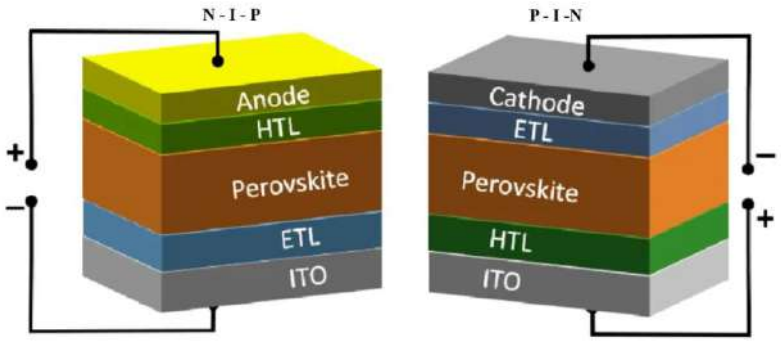


Figure I.14 Schematic representation of conventional N-I-P and inverted P-I-N perovskite solar cell architectures.

A)- Transparent Conducting Oxides (TCOs)

Transparent Conducting Oxides (TCOs) play a critical role in the architecture of optoelectronic devices due to their unique ability to combine high optical transparency in the visible range with excellent electrical conductivity. Widely used TCO materials include Indium Tin Oxide (ITO), Aluminum-doped Zinc Oxide (AZO), and Fluorine-doped Tin Oxide (FTO), which are commonly employed as front electrodes in devices such as solar cells, OLEDs, and flat-panel displays (Hosono, 2017).[67]

TCOs are typically deposited as thin films on glass or flexible polymer substrates, forming the transparent electrode that facilitates charge collection or injection while allowing incident light to reach the active layers of the device (Granqvist, 2000).[68] Structurally, most TCOs possess a crystalline lattice such as wurtzite or rutile, and exhibit a wide optical bandgap (usually >3 eV), which accounts for their high transmittance in the visible spectrum (Ashraf et al., 2019).[69]

The electrical conductivity in TCOs arises primarily from a high carrier concentration, which can be induced by oxygen vacancies or aliovalent doping (e.g., Sn^{4+} in ITO or Al^{3+} in AZO). This results in degenerate n-type semiconducting behavior, allowing for low resistivity values while maintaining optical transparency (Zhang et al., 2016).[70]

In advanced device architectures, parameters such as film thickness, surface roughness, and interfacial compatibility are optimized to ensure efficient integration of TCOs with adjacent layers, particularly organic semiconductors or absorber layers in photovoltaic devices. Moreover, recent research has expanded into p-type TCOs, which aim to enable fully transparent electronic circuits, though achieving high conductivity and transparency simultaneously remains a key challenge (Hu et al., 2020).[71]

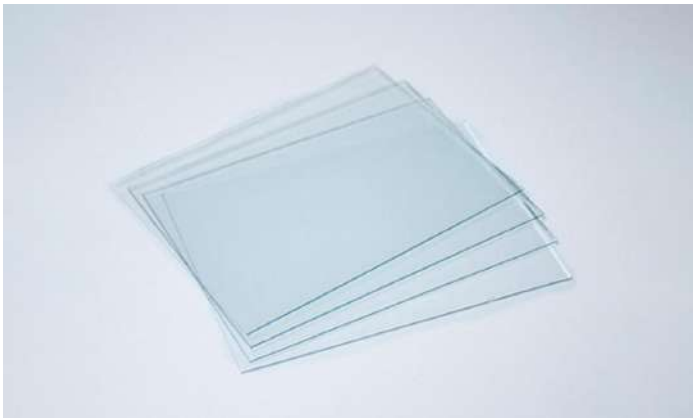


Figure I.15 Surface Morphology of an FTO Substrate (Fluorine-doped Tin Oxide).

B)- The Electron Transport Layer (ETL)

The Electron Transport Layer ETL is a fundamental component in the architecture of perovskite solar cells PSCs. It plays a dual role: facilitating the extraction and directional transport of photo-generated electrons from the perovskite absorber to the cathode, while simultaneously blocking holes, thus suppressing charge recombination and enhancing the overall PCE of the device. The working principle of the ETL is based on energy level alignment: for effective charge transfer, the conduction band minimum CBM of the ETL must be lower than that of the perovskite layer, forming an energy gradient that drives electron flow while impeding hole transport (Jiang et al., 2018).[72]

The concept of charge transport layers emerged from dye-sensitized solar cells (DSSCs), but the use of a dedicated ETL in perovskite solar cells began with early work in 2009, when titanium dioxide TiO_2 was used as the ETL due to its favorable stability and electronic properties (Kojima et al., 2009).[46] However, TiO_2 suffers from low electron mobility (~0.1 $cm^2/V.s$) and requires high-temperature annealing (>450 °C), which limits its compatibility with flexible substrates. This led to the emergence of tin oxide SnO_2 as a superior ETL, owing to its high mobility (~100 $cm^2/V.s$), wide bandgap (~3.6 eV), low-temperature processability (<150 °C), and superior chemical and UV stability (Huang et al., 2022).[73]

Other ETL materials include zinc oxide (ZnO), known for its high mobility and versatile nanostructuring potential, although its chemical instability with perovskite requires surface passivation or compositional modification. Doped versions such as aluminum-doped ZnO AZO and bilayer structures (e.g., ZnO/SnO_2 or TiO_2/SnO_2) have demonstrated enhanced band alignment and surface morphology, leading to notable efficiency improvements from 12% to over 20% in some configurations (Noh et al., 2018).[74] More advanced designs incorporate SnO_2 quantum dots, 2D materials like Mo_2 or SnS_2, and hybrid ETLs that minimize trap states and enhance interfacial contact. These have shown certified efficiencies exceeding 22% (Li et al., 2022; Rathnam et al., 2024).[75]

Recent computational and experimental studies indicate that optimizing ETL properties, such as increasing electron mobility and minimizing interfacial defects, can lead to significant improvements in device metrics open-circuit voltage Voc can increase by up to 200 mV, while the fill factor FF may improve by over 10%, depending on the ETL structure (Tan et al., 2024).[76] Additionally, novel materials such as lanthanum-doped $BaSn_3$ (La-$BaSnO_3$) have emerged with ultrahigh mobility (>300 $cm^2/V.s$) and ideal conduction band alignment with

perovskite layers, making them promising candidates for next-generation PSCs with enhanced stability and efficiency (Zhao et al., 2024).[77]

C)-The Active Absorber Layer:

The absorber layer in the structure of perovskite solar cells (PSCs) functions as the active unit that directly governs the conversion of solar energy into electrical energy, serving as the site where electron-hole pairs are generated under light irradiation. Physically, this layer is a thin crystalline film typically ranging in thickness from 300 to 600 nanometers, and it is deposited atop the electron transport layer ETL using low-temperature solution-based techniques such as spin coating or slot-die printing (Gao et al., 2022).[78]

The crystallinity and defect density within this layer are critical parameters in determining the device's overall performance. Studies have shown that grain boundaries act as non-radiative recombination centers, reducing carrier lifetime and consequently lowering the open-circuit voltage Voc and final power conversion efficiency (Bi et al., 2016).[79] Increasing the average grain size from 250 nm to 800 nm has been reported to enhance cell efficiency by up to 4.5%, and reduce the hysteresis index by more than 50% (Wang et al., 2021).[80]

This layer also exhibits notable mechanical and chemical sensitivity during fabrication. Non-uniform thickness or the presence of pinholes can lead to leakage currents and the formation of shunting paths, which are key contributors to the rapid degradation of photovoltaic performance during operation.[81]

To address these limitations, several strategies have been developed to improve the quality of the absorber layer, including:

- Crystallographic engineering using additives such as $Pb(SCN)_2$ and MACl, which promote larger grain growth and reduce surface trap states, leading to an increase in efficiency from 16% to over 20% in laboratory-scale devices (Jeon et al., 2014; Chen et al., 2019).[82]
- Multi-step thermal annealing, which helps restructure the internal lattice and reduce lattice strain, thereby improving the fill factor (FF) by up to 10% (Wang et al., 2021).[79]
- Anti-solvent engineering, using chlorobenzene or toluene during the coating process, to facilitate rapid and uniform crystallization and minimize microcrack formation (Jeon et al., 2014).[80]

Numerical simulations based on drift-diffusion models have indicated that optimizing the morphology of the absorber layer can lead to an increase in short-circuit current density (Jsc) by 3-5 (mA/cm²), and a fill factor enhancement of 8-12%, resulting in a final power conversion efficiency exceeding 22% in standard two-terminal devices under AM1.5G conditions (Chen et al., 2022).[83]

D)- The Hole Transport Layer (HTL)

The Hole Transport Layer (HTL) is a critical component in both organic solar cells (OSCs) and perovskite solar cells (PSCs), where it functions as a selective conduit for holes generated in the active layer, enabling their extraction and transport to the anode while effectively blocking electrons, thereby minimizing recombination losses. This selective transport mechanism not only enhances the power conversion efficiency (PCE) of the device but also contributes to the stability and longevity of the solar cell (Hu et al., 2020).[84]

The concept of HTLs originated with the development of organic light-emitting diodes (OLEDs) and was later adapted to photovoltaic applications. In PSCs, the HTL typically resides between the transparent conducting electrode (e.g., ITO or FTO) and the perovskite absorber. The choice of HTL material significantly influences interface quality, energy level alignment, film morphology, and charge extraction efficiency. Commonly used HTLs include spiro-OMeTAD, PEDOT: PSS, NiOx, PTAA, and CuSCN. For example, Spiro-OMeTAD, a widely adopted molecular HTL, offers excellent hole mobility and compatibility with perovskite layers but requires expensive additives (e.g., Li-TFSI, tBP) that can compromise long-term stability (Juarez-Perez et al., 2016; Kim et al., 2018).[69-63]

Recent studies have focused on inorganic HTLs, such as nickel oxide (NiOx), due to their high stability, appropriate valence band alignment (~5.2 eV), and lower cost. NiOx has shown promising results in inverted PSCs, contributing to efficiencies exceeding 20% and improved thermal and UV stability (Kim et al., 2018; Yao et al., 2022).[69-70] In addition, new research explores the use of graphene quantum dots (GQDs) and transition metal oxides, which offer tunable electronic properties and can form compact, defect-passivating interfaces with perovskite absorbers (Zheng et al., 2013).[87]

Furthermore, dopant engineering and HTL morphology optimization have proven effective in enhancing hole mobility and reducing trap-assisted recombination. For instance, incorporating dopants such as cobalt, copper, or molybdenum into spiro-OMeTAD or NiOx improves

conductivity and interface contact, ultimately leading to higher fill factors and more stable device operation (Juarez-Perez et al., 2016; Zhao et al., 2020).[72-69]

Overall, the proper design and selection of HTLs are essential for achieving high-efficiency, long-term stable, and scalable perovskite and organic solar cell technologies.

E)- Metal Back Electrode in Perovskite Solar Cells

The metal back electrode plays a critical role in the device architecture of perovskite solar cells (PSCs), functioning both as a charge collection layer and as an electrical contact that transports carriers (electrons or holes) from the transport layers to the external circuit. To ensure efficient operation and long-term stability, this component must fulfill several key criteria: high electrical conductivity ($\geq 10^6$ S/m), chemical inertness toward adjacent layers, work function alignment with the hole transport layer (HTL) or electron transport layer (ETL), and thermal and environmental durability under operational stress conditions (Tress et al., 2021).[89]

Gold (Au) is frequently employed in lab-scale PSCs due to its excellent conductivity (~4.1×10^7 S/m), high chemical stability, and favorable work function (~5.1 eV), which aligns well with commonly used HTL materials such as Spiro-OMeTAD. However, Au tends to react with halide ions from the perovskite under humid or elevated temperature conditions, leading to ion diffusion and device degradation. Additionally, its high cost limits its scalability for commercial applications (Leijtens et al., 2015).[90]

Similarly, silver (Ag) is widely adopted owing to its superior conductivity (~6.3×10^7 S/m) and lower cost relative to gold. Yet, it is more chemically reactive with additives in the HTL (e.g., Li-TFSI), resulting in the formation of interfacial compounds like AgI, which compromise device performance. This issue can be mitigated by inserting ultrathin interfacial buffer layers such as MoO_3 or NiOx (typically 5-20 nm), which enhance charge extraction and prolong device stability.[91]

Copper (Cu), with its high conductivity (~5.9×10^7 S/m) and low cost, offers an appealing alternative; however, it suffers from significant reactivity with the perovskite and may form undesirable oxides or diffusion products. Protective coatings like TiN or CrO_x have been explored to suppress ion migration and improve interfacial stability.[92]

Aluminum (Al), another low-cost and lightweight candidate, has a relatively low work function (~4.3 eV), which is not ideal for direct contact with HTLs. Consequently, interfacial modifiers such as PEDOT: PSS or MoO_3 are required to facilitate effective energy level alignment.

Furthermore, Al's susceptibility to surface oxidation leads to long-term conductivity losses and reduced device lifetime.[93]

Carbon-based electrodes, including graphite, carbon paste, and carbon nanotubes, have attracted attention as low-cost and chemically robust alternatives. They offer excellent resistance to humidity and UV radiation; however, their surface conductivity is often suboptimal (>20 Ω/sq), which can reduce power conversion efficiency unless enhanced through techniques such as thermal annealing or nanomaterial doping (Li et al., 2020).[94]

To address these challenges, interfacial engineering between the back electrode and the adjoining functional layers has become an essential strategy. Numerical simulations and experimental studies have shown that inserting nanoscale interlayers of NiOx or MoO_3 can increase the open-circuit voltage (Voc) by up to +200 mV, improve the fill factor by over 10%, and enhance overall device efficiency by 10-15%, while extending operational stability beyond 1000 hours under accelerated aging conditions.[94]

I.6.2 Deposition Techniques

A)- Spin Coating and Centrifugal Sedimentation in Perovskite Layer Fabrication

Spin coating and centrifugal sedimentation are among the most widely employed techniques for fabricating the active perovskite absorber layer in perovskite solar cells (PSCs), offering advantages in thin film uniformity, crystallinity control, and scalability under low-temperature solution processing conditions.

- **Spin Coating**

Spin coating is the conventional method used to deposit uniform thin films of perovskite precursors (typically PbI_2 and MAI or FAI in DMF/DMSO) onto substrates. The precursor solution is dropped onto the substrate, which is then rotated at speeds typically between 2000

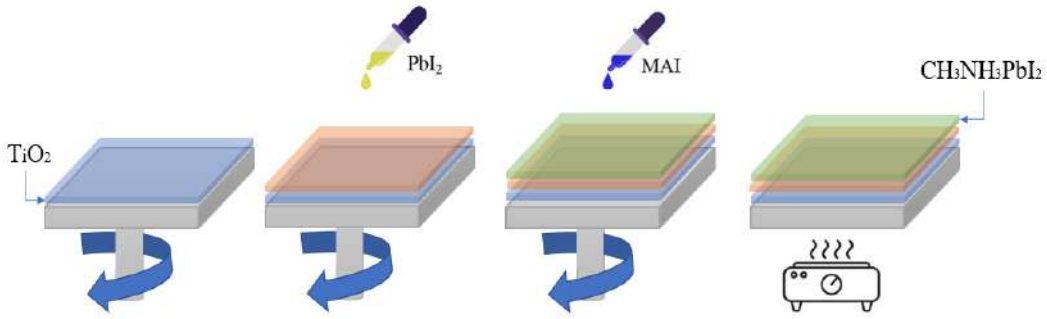


Figure I.16 Schematic illustration for Spin Coating of perovskite films.

and 6000 revolutions per minute (rpm) for 20 to 60 seconds, depending on the desired film thickness, which generally ranges from 300 to 600 nm (Jeon et al., 2014).[79]

To enhance crystallization and suppress defects, anti-solvent dripping is often employed during spinning. A nonpolar solvent like chlorobenzene or toluene is dripped 10-15 seconds into the spinning process to induce rapid nucleation and improve grain size uniformity. After coating, the film is typically annealed at 100-150 °C for 10-30 minutes, promoting phase formation and solvent evaporation (Bi et al., 2016).[95]

- **Centrifugal Sedimentation**

Centrifugation is commonly used in two ways: (1) to purify the precursor solution by removing insoluble aggregates or nanoparticle clusters, and (2) to deposit compact films directly through centrifugal casting. Precursor solutions are placed into centrifuge tubes and spun at 3000-6000 rpm for 5-10 minutes, enabling removal of heavy sediment or achieving homogeneous dispersion of colloidal particles.[96]

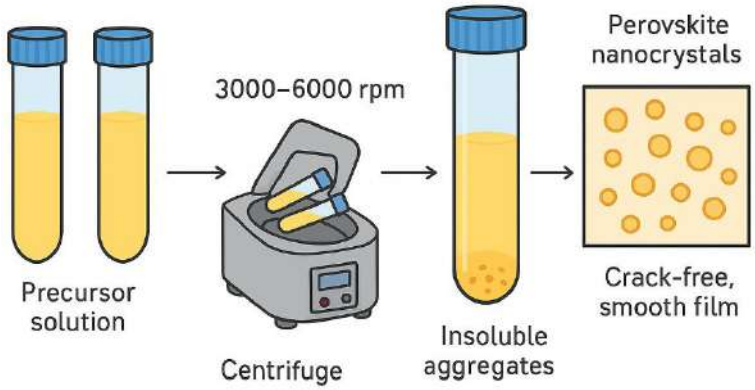


Figure I.17 Schematic illustration for Centrifugal Sedimentation of perovskite films.

This technique is particularly advantageous for nanocrystal-based perovskites such as $CsPbBr_3$ and $CsPbI_2Br$, where controlling the sedimentation rate allows for crack-free, smooth films that enhance device reproducibility and scale-up potential.

perovskite precursor solution uniformly across a heated substrate using a linearly moving blade, resulting in the formation of a thin film with controlled thickness.

B)- Blade Coating Technique for the Fabrication of Perovskite Solar Cells

Blade coating is considered one of the most promising large-scale fabrication techniques for perovskite solar cells (PSCs), due to its high scalability and compatibility with continuous manufacturing processes such as roll-to-roll (R2R) printing. The process involves spreading a

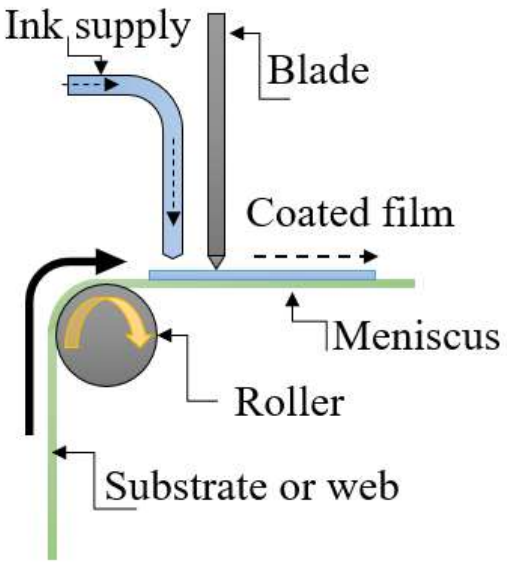


Figure I.18 Schematic illustration for blade coating of perovskite films.

1)- **Key Physical Parameters Influencing Film Quality**

- **Blade Speed:** This directly influences the final film thickness. Optimal speeds typically range between 5 and 60 mm/s. A speed of 30 mm/s, for example, often results in films with thicknesses around ~400 nm.
- **Gap Height (Blade–Substrate Distance):** Generally, set between 100 and 300 µm. Larger gap heights lead to higher solution flow rates and therefore thicker films.
- **Substrate Temperature During Deposition:** Typically maintained between 80 and 120 °C to accelerate solvent evaporation and promote initial crystallization, enhancing the uniformity and crystallinity of the film.
- **Ink Composition:** Common precursor solutions consist of PbI_2 and MAI in a 1:1 molar ratio, dissolved in DMSO or DMF, often with additives like MACl or FAI to enhance grain growth and reduce defect densities.
- **Post-Annealing Treatment:** This thermal step is critical to complete the crystallization process and improve grain size. Annealing is typically performed at 100-150 °C for 10-30 minutes after film deposition.

2)- **Demonstrated Experimental Results**

In a study by Marques et al. (2021),[97] blade coating was applied to deposit $MAPbI_3$ films at a blade speed of 30 mm/s on a substrate heated to 100 °C. The resulting films exhibited a

thickness of ~450 nm and an average grain size of ~800 nm, enabling a power conversion efficiency (PCE) of 21.1% over an active area of 1 cm².

Additionally, in the case of $CsPbBr_3$ perovskite films fabricated via blade coating at a substrate temperature of 110 °C and a gap height of 150 µm, the resulting layers demonstrated high crystallinity, optical absorption exceeding 90% in the visible spectrum (400-750 nm), and excellent thermal stability making them strong candidates for long-term applications (Razza et al., 2015).[98]

C)- Spray Pyrolysis Deposition for Perovskite Solar Cells

Spray pyrolysis is one of the most versatile and scalable thin-film deposition techniques employed in the fabrication of electron-transporting and functional oxide layers for perovskite solar cells (PSCs). Its widespread adoption is primarily due to its operational simplicity, compatibility with moderate processing temperatures, and cost-effectiveness. The method involves atomizing a precursor solution containing metal salts into fine droplets, which are directed toward a heated substrate (typically at 300-500 °C). Upon impact, the solvent rapidly evaporates and the solutes undergo thermal decomposition, forming a uniform, adherent solid layer.

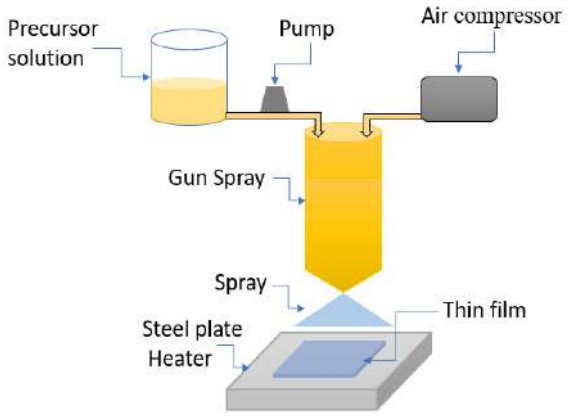


Figure I.19 Schematic illustration for Spray Pyrolysis Deposition of perovskite films**.**

1)**- Process Steps**

The process proceeds through three fundamental stages:

- **Precursor Preparation**: Common precursors include titanium tetrachloride ($TiCl_4$) or titanium isopropoxide for TiO_2, and zinc nitrate for ZnO, typically dissolved in ethanol or deionized water at concentrations of 0.2-0.5 mol/L.

- **Droplet Generation**: The solution is atomized using either airbrush nozzles at 1-2 bar or ultrasonic spray heads, generating droplet sizes between 1-50 µm.
- **Deposition and Pyrolysis**: Droplets are transported toward a heated substrate often FTO or ITO-coated glass maintained at 350-500 °C. The film is formed through successive droplet impact, evaporation, and chemical conversion. Deposition times range from 5-15 minutes, and the resulting film thickness is typically 70-150 nm, depending on precursor concentration and spray duration.

2)- **Experimental Implementations**

- Tsupeng et al. (2016) demonstrated the deposition of compact TiO_2 on FTO substrates using aerosol spray pyrolysis at 450 °C, achieving 16.2% efficiency in $MAPbI_3$-based PSCs due to minimized trap states and improved interfacial contact.[99]
- Kalki et al. (2022) reported ultrasonic spray pyrolysis for $MASnBr_3$ perovskite films, showing improved surface homogeneity and suppressed grain agglomeration, with droplet control enhancing thickness reproducibility around 120 nm.[100]
- Ikemachi et al. (2019) investigated the influence of substrate temperature and confirmed that elevating the pyrolysis temperature to 450 °C significantly enhanced grain boundary definition, decreased porosity, and improved optical absorption.[101]

3)- **Advantages and Scalability**

Spray pyrolysis allows the deposition of oxide-based ETLs such as TiO_2, ZnO, SnO_2, and even perovskite absorber layers under ambient conditions. Its compatibility with flexible or curved substrates, absence of vacuum requirement, and ability to be integrated into roll-to-roll manufacturing lines make it an ideal candidate for the scalable production of next-generation PSCs.

D)- Slot-Die Coating of Perovskite Films

Slot-die coating is considered one of the most industrially viable techniques for depositing thin films in perovskite solar cells (PSCs), owing to its superior control over film thickness, high uniformity, and compatibility with roll-to-roll (R2R) production lines. The method involves dispensing a precursor ink through a narrow slit die head onto a preheated, continuously moving substrate, forming a uniform wet film without the need for vacuum or spin-assisted processes.
The process begins with the preparation of a perovskite precursor ink, typically consisting of methylammonium (MA^+), formamidinium (FA^+), or cesium (Cs^+) cations combined with PbI_2 salts, dissolved in solvents such as DMF, DMSO, or GBL. The solution is prepared at a

concentration of 1.2-1.5 M, with a tuned viscosity ranging between 5-30 mPa.s to ensure stability during coating. Slot-die deposition is carried out with a flow rate of 0.02-0.1 mL/min, a substrate movement speed of 10-50 mm/s, and a nozzle-to-substrate height of 100-250 µm, yielding wet film thicknesses of ~1–2 µm, which shrink to 300-600 nm after annealing.

Following deposition, the films undergo a drying step at 70-100 °C for 30-60 seconds, essential for solvent evaporation and suppression of morphological defects. A thermal annealing step at 100-150 °C for 10-20 minutes facilitates the formation of the desired perovskite crystal structure with minimal pinholes and high optical absorption.

In a study by Whittaker et al. (2018),[102] $MAPbI_3$ films deposited via slot-die coating in ambient air achieved uniform coverage and power conversion efficiencies (PCEs) exceeding 19.5% on 1 cm^2 substrates. Further optimization by Vijayan et al. (2020) enabled PCEs of 21.1%,[103] highlighting the feasibility of this technique under ambient and scalable conditions. Gao et al. (2020) demonstrated that precise control of flow rate and substrate temperature was key to forming uniform films even outside controlled environments.[104]

Slot-die coating also supports the sequential or tandem deposition of additional layers such as SnO_2 (ETL) or NiOx (HTL), facilitating the integration of high-performance device stacks. Moreover, material waste is minimized (<10%), making this method both eco-efficient and cost-effective, especially for large-area and flexible perovskite solar modules.

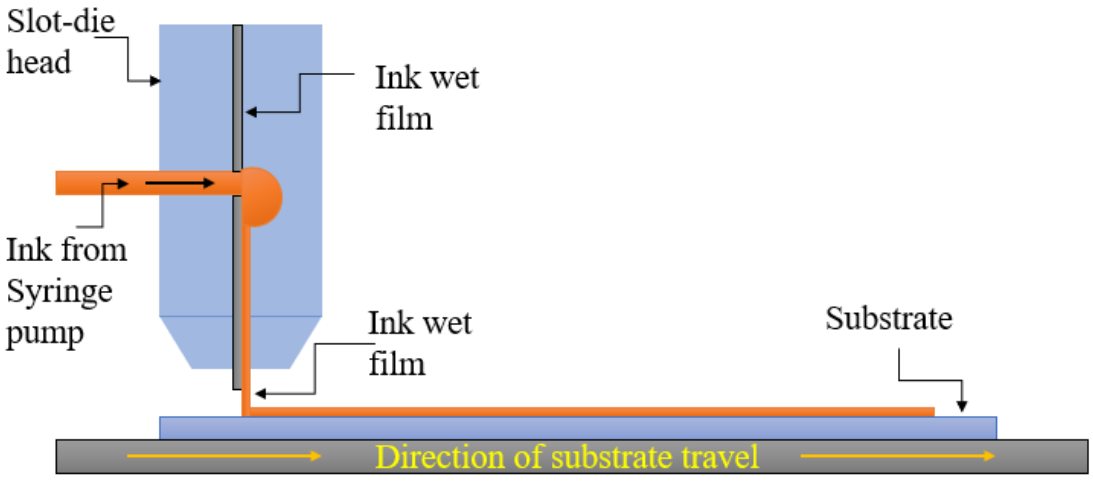


Figure I.20 Schematic illustration for Slot-Die Coating of Perovskite Films.

E)- Inkjet Printing of Perovskite Layers:

Inkjet printing is emerging as a highly promising, contactless, and digitally controlled deposition technique for fabricating perovskite solar cells (PSCs). It offers precise material

usage, excellent patterning resolution, and full compatibility with flexible substrates and scalable roll-to-roll production. This method relies on ejecting microdroplets of a tailored perovskite precursor ink directly onto a preheated substrate, allowing for precise control of film morphology and thickness.

The process begins with the preparation of a well-formulated perovskite ink, typically consisting of precursors such as PbI_2, MAI, or FAI, dissolved in solvents like DMF, DMSO, or GBL. The viscosity is carefully tuned to 5-20 mPa.s, and surface tension is adjusted to 25-40 mN/m to ensure stable jetting and uniform droplet formation. Inkjet nozzles used in PSC fabrication typically have diameters of 10-50 µm, generating droplets in the picoliter range (Zhang et al., 2023).[105]

During printing, substrates are usually maintained at 40-80 °C to assist wetting and solvent evaporation. Post-deposition treatment involves a two-step process: soft baking at 80-100 °C for 1-2 minutes, followed by thermal annealing at 100-150 °C for 10-20 minutes, which promotes complete crystallization of the perovskite layer and enhances film uniformity (Peng et al., 2017; Liu et al., 2020).91]

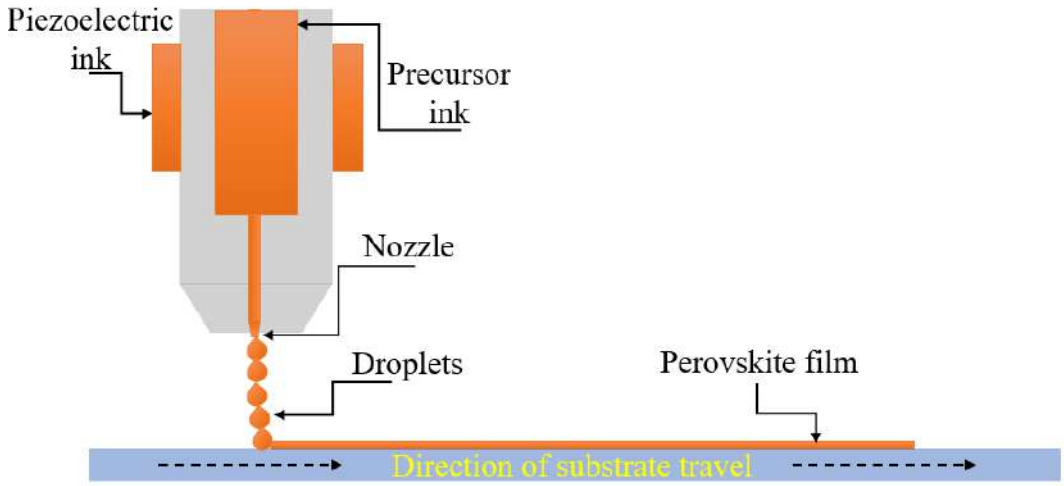


Figure I.21 Schematic illustration for Inkjet Printing of Perovskite Films.

Recent experimental work by Liu et al. (2020) achieved power conversion efficiencies (PCE) up to 18.6% using inkjet-printed $FAPbI_3$ films on glass substrates.[108] Similarly, Unger et al. (2022) demonstrated the fabrication of fully inkjet-printed flexible PSCs with excellent operational stability exceeding 500 hours under continuous illumination.[109]

Inkjet printing also enables multi-pass and gradient deposition, allowing for custom compositional engineering of the absorber or transport layers. The low material wastage

(utilization >90%) and compatibility with additive manufacturing make it highly attractive for low-cost, high-throughput production of perovskite photovoltaics.

I.7 Manufacturing Challenges of Perovskite Solar Cells

Despite the rapid rise of perovskite solar cells (PSCs) as a high-efficiency, low-cost alternative to traditional photovoltaics, their transition from laboratory prototypes to commercially viable modules faces several fundamental challenges. One of the most critical issues is the inherent instability of hybrid organic–inorganic halide perovskites, such as methylammonium lead iodide ($MAPbI_3$), when exposed to moisture, oxygen, UV radiation, or elevated temperatures. Rong et al. (2018) reported that unencapsulated PSCs lost over 50% of their initial efficiency within days under ambient conditions with >50% relative humidity, underscoring the need for improved material stability or advanced encapsulation techniques (Rong et al., 2018).[110]

Long-term operational stability remains a major obstacle. While silicon-based solar modules exhibit lifespans exceeding 25 years, most PSCs degrade significantly within a few months. Mohammed et al. (2023) demonstrated that photo-induced degradation, especially under UV exposure and ambient humidity, leads to the formation of non-photoactive byproducts like PbI_2, as well as decomposition of MA^+ and FA^+ cations, which severely reduce device performance even with encapsulation layers (Mohammed et al., 2023).[111]

A parallel concern is the lead toxicity inherent in state-of-the-art perovskite formulations such as $MAPbI_3$ and $FAPbI_3$. These materials contain up to 0.4 g of Pb per module, which poses environmental and health risks upon leakage or improper disposal. Emphasized that lead leaching into soil or water could result in neurological damage, especially if devices are not recycled or contained properly. Although tin-based alternatives (e.g., $MASnI_3$) have been explored, they suffer from rapid oxidation of Sn^{2+} to Sn^{4+}, causing device instability and performance drop within days (Wang L et al., 2025).[112]

From a manufacturing perspective, issues such as film uniformity, scalability, and reproducibility remain unresolved. Wang et al. (2021) highlighted that most lab-scale deposition techniques (e.g., spin coating) are incompatible with continuous large-area processing. Additionally, variations in solvent evaporation rates and difficulty in controlling perovskite crystallization over large substrates lead to non-uniform absorber layers, affecting device consistency. Scalable techniques like slot-die coating and inkjet printing offer promise, but still face challenges in achieving the reliability, throughput, and yield required for industrial adoption (Wang et al., 2021).[113]

I.8 Future Research Directions in Perovskite Solar Cells

Perovskite solar cells (PSCs) have witnessed remarkable progress over the past decade, not only in power conversion efficiency (PCE) but also in the diversification of applications, enabling their integration into emerging energy technologies. One promising direction is the development of bifacial PSCs, which can absorb light from both front and rear surfaces leading to total power output gains of 20-30% over conventional single-sided designs. Zhang et al. (2019) demonstrated that incorporating semi-transparent rear electrodes, such as indium tin oxide (ITO) and aluminum-doped zinc oxide (AZO), enables high-efficiency bifacial configurations without compromising thermal stability, making them ideal for smart building facades and dual-axis solar farms (chen et al., 2019).[114]

Simultaneously, research is advancing toward flexible and wearable PSCs based on lightweight plastic substrates like PET and PI, processed via low-temperature printing techniques. According to Hashemi et al. (2020), such devices can be integrated into smart textiles and medical wearables, with flexible PSCs achieving lab-scale PCEs exceeding 18%, along with good mechanical durability under repetitive bending. However, challenges remain in optimizing interlayer adhesion and developing corrosion-resistant, conductive flexible electrodes (Hashemi et al., 2020).[115]

A strategic research goal is the development of lead-free perovskite solar cells, in response to growing environmental and toxicity concerns. Most high-efficiency PSCs rely on Pb^{2+}-based compounds (e.g., $MAPbI_3$, $FAPbI_3$), prompting a shift toward tin-based alternatives like $MASnI_3$ and $FASnI_3$. Yet, these materials suffer from chemical instability, primarily due to the rapid oxidation of Sn^{2+} to Sn^{4+}. Getachew Alemu et al. (2020) reported that compositional engineering such as incorporating Cs^+ and FA^+ or using reducing additives like formic acid or ascorbic acid has improved stability, and lead-free PSCs have achieved efficiencies of 13-15% under inert conditions (Alemu et al., 2020).[116]

Additionally, tandem PSCs represent a major avenue for efficiency breakthroughs. As reviewed by Ho-Baillie et al. (2021),[117] perovskite-silicon or perovskite-CIGS tandem cells have demonstrated PCEs exceeding 30%, potentially surpassing the Shockley-Queisser limit. Further, space-grade perovskite photovoltaics are gaining traction due to their low weight and favorable performance under cosmic radiation, positioning them as next-generation candidates for satellites and high-altitude UAVs. Studies by Yong Tu et al. (2022) confirm promising results in orbital and stratospheric environments, highlighting the resilience of optimized PSC designs (Yong Tu et al., 2022).[118]

Conclusion

This chapter began by framing the global energy crisis, highlighting the overreliance on fossil fuels such as petroleum and natural gas, and the resulting environmental consequences most notably greenhouse gas emissions, climate change, and pollution of air and water. The transition toward renewable energy sources was presented not merely as a technological evolution, but as a strategic and environmental imperative for long-term sustainability.

In this context, the chapter provided a detailed examination of the evolution of photovoltaic (PV) technologies across the three generations of solar cells. The first generation, based on crystalline silicon; the second generation, centered on thin-film technologies; and the third generation, featuring advanced concepts such as organic solar cells, dye-sensitized solar cells, and particularly perovskite solar cells (PSCs). A comparative analysis of each generation's benefits and limitations especially regarding power conversion efficiency, manufacturing cost, and environmental sustainability was conducted.

A central focus of the chapter was the in-depth study of perovskite solar cells, which have emerged as one of the most transformative innovations in photovoltaics over the past decade. The discussion traced the historical discovery of perovskite materials, their crystal structure (ABX_3), and the significant milestone of their integration into photovoltaic devices starting in 2009. The unique optoelectronic properties of perovskites such as tunable bandgaps, high absorption coefficients ($\sim 10^5$ cm^{-1}), and long carrier diffusion lengths were analyzed to explain their technological appeal.

Furthermore, the chapter addressed various thin-film deposition techniques used to fabricate perovskite layers, including spin coating, blade coating, spray pyrolysis, inkjet printing, and slot-die coating. These were evaluated in light of processing parameters such as annealing temperature, film thickness, and deposition rate, and their impact on device efficiency and operational stability.

The chapter also critically examined key challenges still hindering the commercial viability of PSCs, including limited long-term stability, high sensitivity to moisture and thermal stress, and environmental concerns associated with lead-containing compounds. In contrast, emerging research directions were explored, such as the development of flexible and wearable PSCs, bifacial designs, tandem configurations, and the pursuit of lead-free compositions.

Chapter

II

SCAPS-1D Theoretical Foundations

This chapter aims to provide a comprehensive overview of the SCAPS 1D simulation tool, covering its theoretical foundations, physical modeling framework, and functional components. It begins with a historical background on the development of SCAPS 1D and the scientific motivations behind its creation. The chapter then explores the physical equations and assumptions that underpin the software's simulation capabilities, particularly for modeling multilayer solar cell architectures. A detailed explanation of the program's graphical interface and functional modules is presented, including how to define materials, configure boundary conditions, and execute simulations. The latter sections highlight the analytical outputs such as current-voltage characteristics, quantum efficiency, and energy band diagrams and discuss the software's advantages and limitations in photovoltaic research. The chapter concludes by connecting the role of SCAPS 1D in accelerating solar cell design with the broader goals of this thesis.

Introduction

In the pursuit of high-efficiency and cost-effective photovoltaic (PV) technologies, numerical simulation tools have emerged as indispensable instruments in both academic and industrial research. These tools provide an efficient and resource-conscious alternative to conventional experimental procedures, enabling researchers to explore and optimize solar cell designs virtually.

By solving fundamental semiconductor equations such as Poisson's equation and the continuity equations for electrons and holes under realistic boundary conditions, simulation platforms allow for detailed physical modeling of charge transport, recombination mechanisms, and electrostatic potential profiles within complex multilayered device architectures.

Among the most widely adopted simulation environments is SCAPS 1D, a one-dimensional numerical tool developed at Ghent University by the team of Prof. Marc Burgelman (Burgelman et al., 2000).[191]

SCAPS 1D operates based on the drift diffusion transport model, providing a flexible framework for simulating multilayer PV structures by enabling the user to define critical material parameters such as bandgap energy, doping concentrations, defect densities, carrier capture cross-sections, and band alignment at heterointerfaces. Its user-friendly graphical interface and robust physics engine have made it a staple in both instructional settings and advanced device modeling studies.

Recent literature highlights the growing importance of such simulation platforms in the development of third-generation solar cells, particularly perovskite-based devices, which require sophisticated modeling to capture their optoelectronic behavior (Shafi et al., 2022).[192] SCAPS 1D enables researchers to conduct detailed J-V (current–voltage) and quantum efficiency (QE) analyses, generate energy band diagrams, and evaluate recombination losses, thereby reducing reliance on trial-and-error fabrication. According to Kaymak et al. (2022),[193] numerical simulation environments support wide-scale parametric studies that would otherwise demand significant laboratory resources, allowing for the identification of critical design factors early in the development cycle.

Moreover, Kojovic et al. (2019) emphasize that integrating simulation tools into the research workflow not only enhances the predictive accuracy of device behavior but also accelerates experimental decision-making and reduces development time.[194] These environments offer a strategic advantage by allowing the exploration of vast design spaces, optimizing layer configurations, and minimizing material waste prior to experimental validation.

In summary, the integration of digital simulation tools particularly SCAPS 1D into PV research is not merely an auxiliary approach, but a strategic imperative. It deepens the physical understanding of device operation, enables rapid prototyping, and facilitates innovation by bridging theoretical modeling with experimental practice, thereby advancing the field toward more efficient and scalable solar energy solutions.

II.1 The Physical and Methodological Framework of the SCAPS 1D Model

The SCAPS 1D simulation program is built on a robust physical and numerical foundation that models the electro-optical behavior of multilayer photovoltaic devices. Its numerical model is based on solving a coupled system of differential equations that govern charge transport and electrostatic potential within the solar cell structure. This approach captures the core physical phenomena that determine device performance, especially in complex materials such as perovskite-based solar cells**.**

The model solves three principal equations Poisson's equation, the continuity equations, and the drift–diffusion transport equations under a one-dimensional (1D) simulation environment, optimized for layered thin-film structures.

a)- Poisson Equation:

$$\frac{\partial}{\partial x}\left(-\varepsilon(x)\frac{\partial V}{\partial x}\right) = q[-n(x) + p(x) - N_A^- + N_D^+ + p_i(x) - n_i(x)] \qquad (2)$$

The Poisson equation ,[195] presented above describes the spatial variation of the electrostatic potential *V(x)* within a semiconductor material as a function of the net local charge density. This charge density includes contributions from free carriers namely, electrons *n(x)* and holes *p(x)* as well as from ionized dopants, both donors N_D^+ and acceptors N_A^-. Additionally, the equation accounts for injected or trap-related charge carriers, denoted by $n_i(x)$ and $p_i(x)$which are especially relevant in defect-rich or illuminated structures. The resulting electric field, given by *E(x)* = - $\frac{\partial V}{\partial x}$, governs the drift component of carrier transport and plays a critical role in charge collection efficiency. To clarify the physical meaning and dimensional units of each symbol used in Equation (2).

b)- Carrier Continuity Equations

$$\frac{\partial n}{\partial t} = \frac{1}{q}.\frac{\partial J_n}{\partial x} + G_n - R_n \quad (3)$$

$$\frac{\partial p}{\partial t} = \frac{1}{q}.\frac{\partial J_p}{\partial x} + G_p - R_p \quad (4)$$

Equations (3) and (4) represent the fundamental principle of charge conservation within a semiconductor material. The terms $\frac{\partial n}{\partial t}$ and $\frac{\partial p}{\partial t}$ denote the time-dependent change in electron and hole concentrations, respectively. These variations result from three primary processes: charge carrier transport, represented by the spatial derivatives of the current densities $\frac{\partial J_n}{\partial x}$ and $\frac{\partial J_p}{\partial x}$ carrier generation due to light absorption G_n, G_p and recombination losses R_n, R_p within the bulk or at interfaces.[108]

Solving these equations is essential for understanding both steady-state and transient behaviors of solar cells, particularly within numerical models such as SCAPS 1D, which simulate the optoelectronic dynamics of multilayer devices like perovskite solar cells.

c)- Shockley-Read-Hall (SRH) Recombination Equation

Trap-assisted non-radiative recombination is one of the dominant performance-limiting mechanisms in thin-film solar cells, especially in materials with imperfect crystallinity, such as metal halide perovskites. This recombination process is accurately described by the extended form of the Shockley–Read–Hall (SRH) model, which accounts for the position of trap levels within the bandgap and the electronic properties of the semiconductor.

The generalized expression for the SRH recombination rate is given by:

$$R^{SRH} = \frac{n\,.\,p - n_{i,e}^2}{\tau_p(n + n_1) + \tau_n\,(p + p_1)} \quad (5)$$

Here, the numerator $(n\,.\,p - n_{i,e}^2)$ represents the deviation from thermal equilibrium,[196] while the denominator models the combined probabilities of electron and hole capture and emission via a trap level E_T The auxiliary terms n_1 and p_1 are thermally activated carrier concentrations defined as:

$$n_1 = N_C \,.\exp\left(\frac{E_T - E_C}{K_B T}\right) \quad (6)$$

$$p_1 = N_V \,.\exp\left(\frac{E_V - E_T}{K_B T}\right) \quad (7)$$

where E_T is the energy level of the trap, E_C and E_V are the conduction and valence band edges, and N_C and N_V denote the effective density of states in the respective bands.

This model becomes critically important in materials where the trap density N_T is high such as at grain boundaries, interfacial layers, or poorly passivated surfaces. The electron and hole lifetimes τ_n and τ_p depend on the trap density and the capture cross-sections σ_n, σ_p, following:

$$\tau = \frac{1}{\sigma \,.\, \upsilon_{th} \,.\, N_T} \quad (8)$$

where υ_{th} is the thermal velocity of charge carriers.

In simulation environments such as SCAPS 1D, this extended SRH model is essential for accurately capturing loss mechanisms due to deep-level defects, and it plays a central role in determining key performance parameters such as the open-circuit voltage Voc and overall power conversion efficiency (PCE).

II.2 Analytical Modeling of Photovoltaic Performance Indicators in Solar Cells

The four fundamental photovoltaic performance indicators open-circuit voltage V_{OC}, short-circuit current density J_{SC}, fill factor FF, and power conversion efficiency PCE serve as critical metrics for assessing the effectiveness of solar cells. These parameters are not merely numerical outputs; rather, they represent a deep interplay of physical processes including charge generation, recombination, transport, and electrostatic alignment within the multilayer structure of the device. Analytical expressions are widely used to link these physical behaviors to experimentally measurable quantities or numerical outputs obtained from simulation tools like SCAPS 1D.

The open-circuit voltage V_{OC}, defined as the maximum voltage available when no current flows, is governed by the quasi-Fermi level separation of electrons and holes under illumination. It can be expressed as:

$$V_{OC} = \frac{KT}{q} . In \left(\frac{(N_A + \Delta n)\Delta n}{n_i^2}\right) \quad (9)$$

Here, K is Boltzmann's constant, T is the absolute temperature, q is the elementary charge, N_A is the acceptor doping concentration, Δn is the excess carrier concentration generated by light absorption, and n_i^2 is the intrinsic carrier concentration. This relation highlights the dependence of V_{OC} (V) on photogenerated carrier accumulation and recombination losses. Lower-quality materials with high defect densities reduce Δn, resulting in a decreased V_{OC} (V).[197]

The short-circuit current density J_{SC} (mA/cm^2), representing the maximum photocurrent under zero voltage bias, is given by:

$$J_{SC} = q.G\left(L_n + L_p\right) \quad (10)$$

In this equation, G is the photogeneration rate of electron–hole pairs, and L_n, L_p are the diffusion lengths of electrons and holes, respectively. These lengths depend on carrier lifetimes and mobilities, and thus, J_{SC} (mA/cm^2) reflects the cell's ability to collect carriers before they recombine. A low J_{SC} (mA/cm^2) may indicate ineffective charge transport or insufficient light absorption.

The fill factor FF (%) quantifies the squareness of the J-V curve and is defined by the ratio of the maximum extractable power to the ideal power given by the product of V_{OC} (V) and J_{SC} (mA/cm^2):

$$FF = \frac{P_{max}}{V_{OC} . J_{SC}} \quad (11)$$

Where P_{max} is the maximum power output at the optimal operating point. FF (%) is sensitive to resistive losses (series and shunt), interface quality, and recombination mechanisms, especially at interfaces and electrodes. A lower FF (%) often reflects internal inefficiencies or mismatches in charge extraction.

Finally, the power conversion efficiency PCE (%)integrates the previous three parameters and quantifies the overall effectiveness of the solar cell in converting incident optical power into usable electrical energy:

$$PCE = \frac{V_{OC} \cdot J_{SC} \cdot FF}{P_{in}} \quad (12)$$

Here, P_{in} represents the incident optical power density, typically 1000 W/m² under AM1.5G standard conditions. The PCE (%) thus captures the cumulative influence of material quality, device architecture, and interfacial behavior.

These expressions are not only useful for performance evaluation but also for guiding the design and optimization of solar cells. In numerical simulation environments like SCAPS 1D, these parameters are extracted from the simulated $J - V$ curves and provide quantitative feedback for correlating physical layer parameters such as doping, defect density, and energy band alignment with expected device performance prior to fabrication.[198]

Conclusion:

In conclusion, the SCAPS 1D program stands as a powerful and versatile numerical simulation tool for the study and analysis of solar cells with various structural configurations and material/electronic properties. By dividing its interface into clearly defined functional zones, we have provided a detailed description of the procedures for data input, physical parameter configuration, simulation execution, and result analysis. This structured approach not only enhances the understanding of the program's operation but also offers a systematic framework for constructing accurate models and simulating diverse design scenarios, thereby contributing to the optimization of solar cell performance and the advancement of next-generation photovoltaic technologies.

Chapter

III

Flexible Perovskite Solar Cell

This chapter aims to investigate the enhancement of flexible perovskite solar cell performance through the integration of novel materials in both the hole transport layer (HTL) and the electron transport layer (ETL), specifically by employing CBz-PAI interlayers and MXene-based back contacts. The study is conducted using drift–diffusion numerical modeling via the SCAPS 1D simulator, with the objective of analyzing the influence of these materials on key photovoltaic parameters, including power conversion efficiency (PCE), open-circuit voltage (Voc), short-circuit current density (Jsc), and fill factor (FF). The work focuses on assessing the potential of these materials to reduce energy losses and improve charge transport, while considering the mechanical and structural flexibility required for flexible device applications.

Introduction

Despite the remarkable progress achieved in flexible perovskite solar cells (FPSCs) in recent years, a clear knowledge gap remains regarding the integration of high photovoltaic performance with the mechanical and structural requirements of flexible devices. Transitioning from rigid to flexible architectures imposes strict constraints on processing temperature, layer thickness, and material choice, which can adversely affect the optical and electrical properties, ultimately leading to reduced efficiency and long-term operational stability.[42],[119],[120]

Among the main challenges faced by FPSCs are: (1) limited power conversion efficiency (PCE) due to interfacial losses, (2) high non-radiative recombination rates caused by energy level mismatches, and (3) reduced charge collection efficiency as a result of low electrical conductivity or high series resistance in the transport layers.[121],[57] Addressing these challenges requires a targeted optimization of both the hole transport layer (HTL) and the electron transport layer (ETL), as these layers directly control charge extraction and separation, strongly influencing energy losses and the chemical stability of the device.[122],[123]

In this context, the present work adopts an innovative approach by incorporating a CBz-PAI interlayer to improve interfacial contact between the absorber and transport layers, thereby reducing energy level mismatch losses, along with employing MXene-based back contacts, which offer high electrical conductivity and excellent work function alignment, resulting in lower series resistance and enhanced charge collection.[124],[125],[126] This approach, implemented within a numerical simulation framework, enables an in-depth analysis of its effects on key photovoltaic parameters, including PCE, open-circuit voltage (Voc), short-circuit current density (Jsc), and fill factor (FF), while considering compatibility with low-temperature, polymer-based flexible substrates.

To implement this proposed design in the SCAPS 1D simulation environment, it was necessary to select appropriate materials for each device layer based on precise physical and electronic criteria. This selection process is presented in the following section, “Selection of Materials and Parameters for Simulation.”

III.1 Selection of Materials and Parameters for Simulation

The selection of materials for each layer in the proposed flexible perovskite solar cell design was guided by rigorous physical and electronic criteria. These include an optimal band gap for effective light absorption, appropriate electron affinity to facilitate efficient charge extraction, high charge carrier mobility, low defect density to minimize non-radiative recombination, and favorable chemical and thermal stability. In addition, compatibility with low-temperature processing techniques was prioritized to ensure suitability for flexible polymer substrates such as polyethylene terephthalate (PET). These considerations aim to ensure the successful integration of the proposed CBz-PAI interlayer and MXene-based back contact into the device structure.

III.1.1 Physical and Electronic Properties of Selected Materials

Table III.1-2 provides a summarized overview of the key physical and electronic properties of the materials employed in the proposed flexible perovskite solar cell design. These materials were selected based on their energy-level alignment with adjacent layers, ability to enhance charge transport and minimize energy losses, as well as their chemical and thermal stability and compatibility with low-temperature fabrication processes. This reference data forms the scientific basis for the subsequent numerical modeling performed using the SCAPS 1D simulator.

Table III.1 Input parameters for TCOs, ETL, and 3D-PVK $(FAPbI_3)_{0.77}(MAPbBr_3)_{0.14}(CsPbI_3)_{0.09}$

Parametre	TCOs		ETL					Absorber layer
	AZO	MXene Ti_2CF_2	SnS_2	$BaZrS_3$	STO	WS_2	ZrS_2	3D-PVK
Thickness(nm)	100	/	130	130	130	130	130	550
E_g (eV)	3.10	/	1.85	1.9	3.2	1.8	2.5	1.5
X(eV)	4.1	/	4.26	4.1	4	3.95	4.1	3.9
ϵ_r (eV)	9	/	17.7	9.6	8.7	13.6	16.4	10
C_b (cm^{-3})	$1.1E^{+17}$	/	$7.32E^{+18}$	$2.2E^{+18}$	$1.7E^{+19}$	$1.00E^{+17}$	$2.2E^{+18}$	$2.7E^{+18}$
V_b (cm^{-3})	$1.0E^{+18}$	/	$1.0E^{+19}$	$1.8E^{+19}$	$2.0E^{+20}$	$2.4E^{+16}$	$1.8E^{+19}$	$3.9E^{+18}$

μ_n ($cm^2V{-}1s{-}1$)	100	/	50	$1.7E^{-2}$	$5.3E{+}3$	100	$2.3E{+}3$	10
μ_p ($cm^2V{-}1s{-}1$)	25	/	25	$5.9E^{-2}$	$6.6E{+}2$	100	$1.3E{+}3$	10
N_D (cm^{-3})	$1.00E{+}15$	/	$9.85E{+}19$	$1.80E{+}18$	$2.00E{+}16$	$1.0E{+}18$	$1.0E{+}15$	$1.00E{+}9$
N_A ($cm{-}3$)	0	/	0	0	0	0	0	$1.00E{+}9$
N_t (cm^{-3})	$1.00E{+}10$	/	$1.00E{+}15$	$1.00E{+}15$	$2.00E{+}16$	-	$1.00E{+}15$	$1.00E{+}14$
Energy level (eV)	0.6	0.6	0.6	0.6	0.6	0.6	0.6	0.6
Work function (eV)	4.19 [127]	5.09 [128]	/	/	/	/	/	/
Referance	**[129]**	/	**[130]**	**[130]**	**[131]**	**[131]**	**[132]**	**[133]**

Table III.2 Input parameters for 2D-PVK(CBz-PAI), and organic and inorganic HTLs.

Parametre	Inter layer passivation	HTL				
	2D-PVK CBz-PAI	**ACZTSe**	**CuBiS3**	**CZGS**	**D-PBTTT-14**	**SeTe Cu2O**
Thickness (nm)	5	100	100	100	-	100
Eg (eV)	3.1	1.15	1.55	1.59	2.16	1.88
X(eV)	2.26	4.4	3.4	3.9	3.2	3.53
ϵ_r *(eV)*	3.0	9	13.4	10	10	7.11
C_b ($cm{-}3$)	$2.2E{+}18$	$2.2E{+}18$	16.45	$2.2E{+}18$	$2.8E{+}19$	$2.02E{+}17$
V_b ($cm{-}3$)	$1.8E{+}19$	$1.8E{+}19$	$3.5E{+}19$	$1.8E{+}19$	$1.0E{+}19$	$1.17E{+}19$
μn ($cm^2V{-}1s{-}1$)	$2.0E^{-2}$	$7.51E{+}2$	$2.4E{+}19$	6	$2.83E^{-3}$	1297
μp ($cm^2V{-}1s{-}1$)	$2.0E^{-2}$	$2.00E{+}1$	3	2	$2.83E^{-3}$	1297
N_D (cm^{-3})	0	0	0	0	0	0
N_A ($cm{-}3$)	$1.0E{+}19$	$1.00E{+}16$	$6.8E{+}1$	$7.00E{+}16$	$1.00E{+}18$	$3.00E{+}18$
N_t (cm^{-3})	0	$1.00E{+}14$	$1.00E{+}15$	$1.00E{+}18$	$1.00E{+}14$	$1.00E{+}15$
Energy level (eV)	0.6	0.6	0.6	0.6	0.6	0.6
Reference	**[134]**	**[135]**	**[132]**	**[132]**	**[136]**	**[137]**

III.1.2 Detailed Description of Selected Materials

- **Aluminum-Doped Zinc Oxide (AZO)**

Aluminum-doped zinc oxide (AZO) is a transparent conducting oxide (TCO) widely employed as a front electrode in optoelectronic devices due to its excellent optical transmittance (>85% in the visible spectrum) and high electrical conductivity. Doping ZnO with Al^{+3} ions enhances its carrier concentration and mobility by introducing additional free electrons into the conduction band. AZO offers a low-cost, non-toxic alternative to indium tin oxide (ITO) and demonstrates high stability under ambient conditions, making it an attractive choice for flexible photovoltaic applications.[122] The wide band gap (~3.3 eV) ensures minimal parasitic absorption, while its high work function alignment with electron transport layers facilitates efficient charge extraction.[138]

- **MXene (Ti_2CF_2, $V_3C_2F_2$) as Back Contact**

MXenes are a family of two-dimensional transition metal carbides and nitrides characterized by exceptional electrical conductivity, tunable surface terminations, and high mechanical flexibility. In this work, Ti_2CF_2 and $V_3C_2F_2$ are considered as back contact materials to enhance charge extraction and reduce series resistance. Their tunable work function enables excellent alignment with the valence band of the hole transport layer, while their high carrier mobility supports rapid charge transfer. MXenes also exhibit favorable mechanical properties,[124] making them compatible with flexible device architectures. Furthermore, their surface chemistry can be engineered to improve chemical stability and contact adhesion.[125]

- **Barium Zirconium Sulfide ($BaZrS_3$)**

$BaZrS_3$ is an emerging chalcogenide perovskite material with a direct band gap (~1.7 eV), suitable for use as an electron transport layer (ETL) due to its excellent chemical stability, low toxicity, and favorable electronic alignment with common perovskite absorbers. The high absorption coefficient and thermal stability of $BaZrS_3$ combined with its ability to be processed at relatively low temperatures, make it ideal for flexible devices. Its conduction band position facilitates efficient electron extraction while suppressing interfacial recombination losses.[139]

- **Tin Disulfide (SnS_2)**

Tin disulfide (SnS_2) is a layered n-type semiconductor with a wide band gap (~2.2 - 2.4 eV), making it suitable for electron transport applications. Its high electron mobility and strong

absorption in the UV-visible range enhance charge collection efficiency when interfaced with perovskite absorbers. The layered structure of SnS_2 facilitates solution-based low-temperature deposition, compatible with flexible substrates. Its conduction band minimum is well-aligned with the perovskite absorber, enabling efficient electron extraction while reducing interfacial recombination. Additionally, SnS_2 is chemically stable, environmentally benign, and cost-effective, which makes it a promising candidate for large-scale flexible photovoltaic applications.[140],[141]

- **Strontium Titanate ($SrTiO_3$, STO)**

Strontium titanate ($SrTiO_3$) is a perovskite oxide semiconductor with a wide band gap (~3.2 eV) and exceptional stability under UV illumination. It serves as an effective ETL due to its suitable conduction band position, which allows efficient electron extraction while blocking holes. STO possesses high dielectric permittivity, which reduces Coulombic attraction between photo-generated carriers, thus enhancing carrier separation. Its mechanical robustness and chemical inertness make it particularly attractive for flexible devices where long-term environmental stability is required.[142]

- **Tungsten Disulfide (WS_2)**

Tungsten disulfide (WS_2) is a two-dimensional transition metal dichalcogenide (TMD) material with a band gap of ~1.35 - 2.1 eV, depending on its thickness (monolayer to bulk). WS_2 exhibits high electron mobility and tunable electronic properties, making it a suitable ETL material in perovskite solar cells. Its layered structure enables flexible deposition techniques and provides mechanical flexibility, while its high chemical stability ensures durability under operating conditions. Additionally, WS_2 can passivate surface defects at the perovskite interface, reducing recombination and enhancing device performance.[143]

- **Zirconium Disulfide (ZrS_2)**

Zirconium disulfide (ZrS_2) is an n-type semiconductor with a band gap of ~1.7 eV, part of the transition metal dichalcogenide family. ZrS_2 combines high carrier mobility with strong light-matter interaction, making it a promising ETL candidate. Its conduction band position matches well with common perovskite absorbers, enabling efficient charge extraction. ZrS_2 also offers excellent chemical stability and can be processed at low temperatures, which is essential for flexible photovoltaic applications.[144]

- **Triple-Cation Perovskite Absorber**

The triple-cation perovskite (commonly $Cs_{0.05}$ $FA_{0.83}$ $MA_{0.12}$ PbI_3) combines cesium (Cs^+), formamidinium (FA^+), and methylammonium (MA^+) cations in the A-site of the perovskite lattice. This composition enhances phase stability, reduces ion migration, and suppresses moisture-induced degradation. The optimized band gap (~1.55 eV) allows broad absorption in the visible spectrum, and the improved crystallinity leads to enhanced carrier mobility and reduced trap densities. The triple-cation strategy significantly improves device performance and long-term stability, especially in flexible architectures where mechanical stress can accelerate degradation.[57]

- **CBz-PAI Interlayer**

The CBz-PAI (carbazole-polyaryleneimide) interlayer is an organic material designed to enhance interfacial contact between the perovskite absorber and the HTL. It offers excellent thermal and chemical stability, along with tunable energy levels for optimal band alignment. CBz-PAI effectively passivates defects at the interface, suppressing non-radiative recombination and improving charge extraction. Its mechanical flexibility and processability via solution methods make it ideal for incorporation into flexible PSC architectures.[134]

- **Ag-Cu-Zn-Ti-Se (ACZTSe) HTL**

The quaternary chalcogenide ACZTSe is a p-type semiconductor with a tunable band gap (~1.0–1.5 eV) and high hole mobility. It exhibits strong absorption in the visible range, high thermal stability, and compatibility with low-temperature deposition. ACZTSe's valence band aligns well with that of perovskite absorbers, enabling efficient hole extraction while blocking electron backflow. Its elemental composition is free of toxic heavy metals, supporting environmentally sustainable photovoltaic manufacturing.[145]

- **Copper Bismuth Sulfide ($CuBiS_3$)**

$CuBiS_3$ is a p-type semiconductor with a direct band gap of ~1.38 eV and high absorption coefficient, making it suitable for use as an HTL. It is composed of earth-abundant and non-toxic elements, providing an environmentally friendly alternative to conventional HTL materials. $CuBiS_3$'s valence band position enables efficient hole transport, and its inherent stability under operational conditions enhances the durability of the device.[146]

- **Cu_2ZnGeS_4 (CZGS)**

Cu_2ZnGeS_4 (CZGS) is a kesterite-type semiconductor with a band gap of ~1.5 eV, high absorption coefficient, and excellent thermal stability. Its composition consists of abundant and non-toxic elements, and its valence band alignment is ideal for hole extraction in perovskite solar cells. CZGS can be fabricated via low-cost solution processes, making it attractive for large-scale flexible device production.[147]

- **D-PBTTT-14**

D-PBTTT-14 (poly[2,5-bis(3-tetradecylthiophen-2-yl) thieno[3,2-b] thiophene]) is a highly crystalline conjugated polymer with high hole mobility and mechanical flexibility, making it suitable for HTL applications in flexible PSCs. Its molecular structure promotes strong π-π stacking, enabling efficient charge transport. The polymer's energy levels can be tuned through chemical modifications to achieve optimal band alignment with the perovskite absorber.[148]

- **Se/Te-Doped Cu_2O**

Se/Te-doped Cu_2O is a p-type semiconductor with improved electrical conductivity and tailored band structure compared to pristine Cu_2O. The incorporation of Se or Te atoms narrows the band gap slightly, enhancing visible light absorption, and improves hole mobility, leading to more efficient charge extraction. Cu_2O is abundant, non-toxic, and chemically stable, making it an attractive HTL material for sustainable photovoltaics.[149]

III.2 Results and Discussion

Phase I (without CBz-PAI interlayer)

In the initial stage, the reference architecture of the flexible perovskite solar cells (FPSC) was considered, namely (PET/AZO/ETL/$(FAPbI_3)_{0.77}(MAPbBr_3)_{0.14}(CsPbI_3)_{0.09}$/HTL/MXene). As illustrated in Figure III.1, the schematic diagram depicts the layer-by-layer structure of the investigated device, which consists of a flexible PET substrate, an aluminum-doped zinc oxide (AZO) transparent conductive layer, the tested electron transport layers (ETLs), the mixed perovskite absorber, different hole transport layers (HTLs), and the MXene-based back contact. The diagram also highlights the location of the CBz-PAI passivation interlayer, which is inserted in certain configurations to improve interfacial properties and suppress recombination.

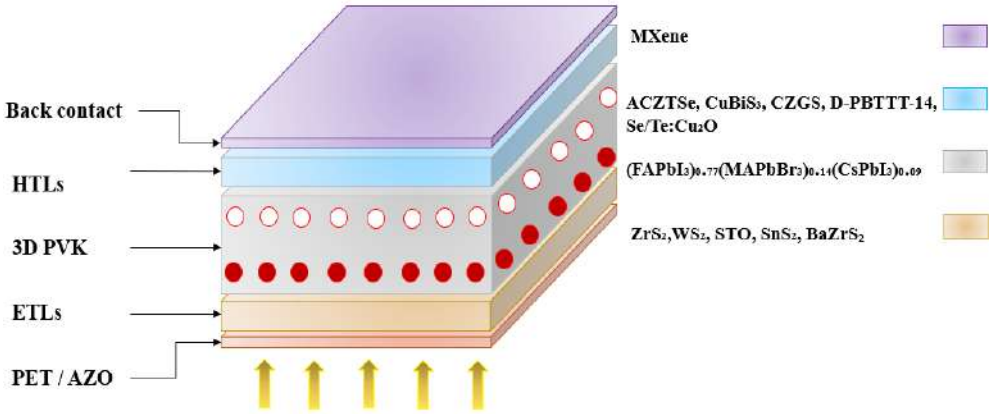


Figure III.1 Schematic architecture of the reference flexible perovskite solar cell structure without the CBz-PAI passivation interlayer, consisting of PET/AZO/ETL/$(FAPbI_3)_{0.77}$ $(MAPbBr_3)_{0.14}(CsPbI_3)_{0.09}$/HTL/MXene.

In the preliminary simulations, the performance of these reference devices was evaluated, as shown in Figure III.2.a, by testing five different HTLs Se/Te: Cu_2O, D-PBTTT-14, CZGS, $CuBiS_3$, and ACZTSe in combination with five ETLs, namely: ZrS_2, WS_2, STO, SnS_2, and $BaZrS_2$. The results demonstrated a wide variation in the power conversion efficiency (PCE), ranging from ≈17% to more than 26%, depending on the interfacial alignment between the selected HTL and ETL.

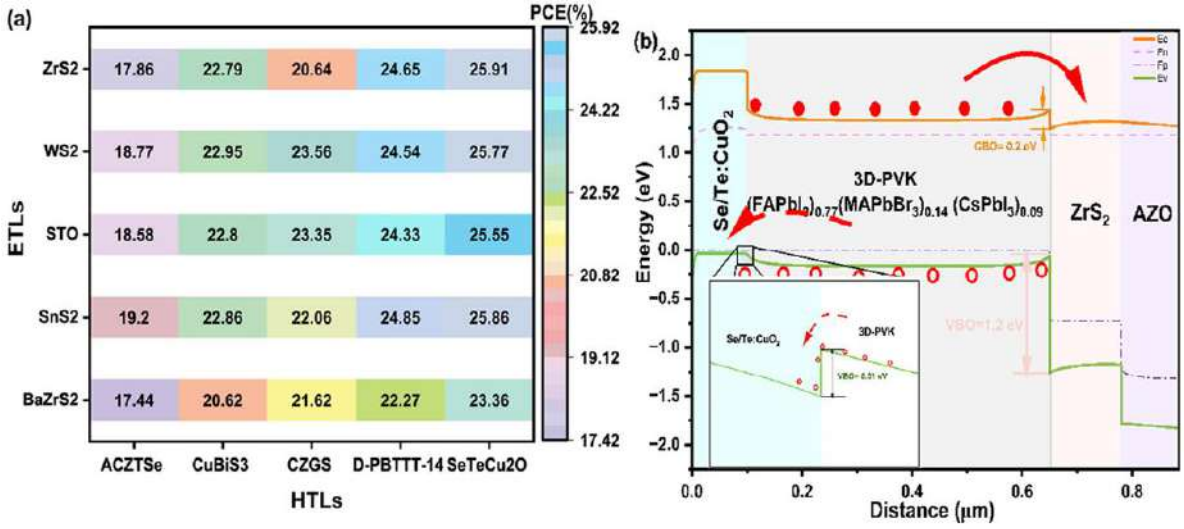


Figure III.2 a) Heat-map of average PCE FPSC devices on n-i-p structure (PET/AZO/ETL/(FAPbI3)0.77(MAPbBr3)0.14(CsPbI3)0.09/HTL/MXene) without CBz-PAI passivation interlayer, b) band diagram energy of AZO/ZrS2/(FAPbI3)0.77(MAPbBr3)0.14 (CsPbI3)0.09/Se/Te: CuO2/ MXene.

Among the investigated materials, Se/Te: Cu_2O stood out as the best-performing HTL, achieving a maximum PCE of 25.91% when paired with ZrS_3, followed by 25.86% with SnS_2, and 25.77% with WS_2. This superior performance is attributed to the nearly ideal energy-level alignment at the PVK/SeTe: Cu_2O interface, as shown in the band diagram (Figure III.2b), where a minimal valence band offset (VBO ≈ -0.01 eV ≈ 100 meV) was observed. Such a small offset facilitates efficient hole extraction, reduces interfacial recombination, suppresses the reverse saturation current (J_0), and consequently enhances both the open-circuit voltage (Voc) and the fill factor (FF). In contrast, the polymer D-PBTTT-14 exhibited relatively stable performance across all ETLs, with efficiencies ranging from 22.27% to 24.65%. The CZGS HTL yielded moderate performance (20.64% - 25.86%), showing strong dependence on the ETL selection. Conversely, $CuBiS_3$ (20.62% - 22.95%) and ACZTSe (≤19.20%) showed the weakest results due to non-ideal band alignment and higher recombination losses.

In addition, the incorporation of the CBz-PAI interlayer plays a crucial role in improving the performance of flexible perovskite solar cells, primarily by suppressing interfacial recombination and facilitating more efficient charge transfer across the perovskite/HTL interface. Figure III.3 illustrates the device structure with the CBz-PAI passivation layer, composed of:

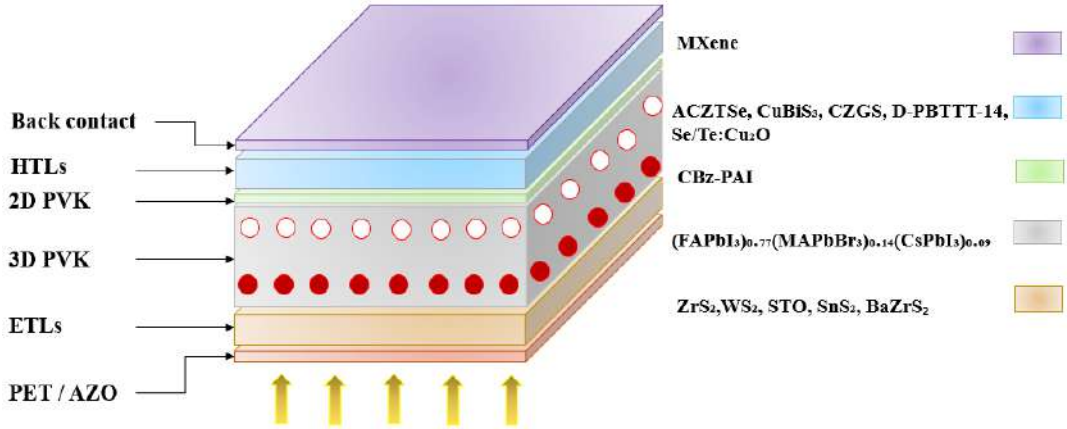


Figure III.3 Schematic architecture of the flexible perovskite solar cell structure with the CBz-PAI passivation interlayer, consisting of PET/AZO/ETL/$(FAPbI_3)_{0.77}(MAPbBr_3)_{0.14}(CsPbI_3)_{0.09}$/CBz-PAI/HTL/MXene.

The results confirm that the presence of this interlayer significantly improves energy-level alignment, reduces the density of interfacial defect states, and lowers the reverse saturation current (J_0), thereby mitigating Voc losses. Furthermore, the CBz-PAI layer enhances the selectivity of charge transport, which collectively contributes to higher overall photovoltaic

performance. Nevertheless, to avoid redundancy with previous studies that had already established the outstanding performance of Se/Te: Cu_2O, this material was excluded from the present work. Instead, the focus was directed toward investigating the effect of HTL thickness and its defect density on the photovoltaic performance of flexible perovskite solar cells.

III.3 Impact of CBz-PAI Interlayer on Various ETLs and HTLs-Based FPSCs Performance

$CuBiS_3$ is excluded from this section due to its incompatibility with the 2D-perovskite architecture, which leads to unfavorable interfacial energetics and poor carrier extraction when paired with the layered absorber. Likewise, Se/Te: Cu_2O is not re-investigated here because its optimal performance has already been established in our previous studies, rendering further analysis redundant within the present scope. Consequently, we concentrate on D-PBTTT-14, CZGS, and ACZTSe to explore new ETL/HTL pairings and to evaluate the role of the CBz-PAI passivation interlayer under configurations that remain compatible with 2D-perovskite.

Across these configurations, introducing CBz-PAI produces a clear, systematic uplift in PCE, most prominently when ZrS_2 is used as the ETL, indicating that the interlayer beneficially re-engineers the perovskite/HTL interface. Quantitatively, the PCE evolves from 24.65% to 24.66% for D-PBTTT-14, from 20.64% to 25.86% for CZGS, and from 17.86% to 24.58% for ACZTSe see Figure III.4 b-d. These gains are consistent with a CBz-PAI induced reduction in interfacial trap density and the formation of a benign interfacial dipole, both of which mitigate non-radiative recombination at the perovskite/HTL boundary and lower the kinetic barrier for hole transfer. In other words, the interlayer chiefly improves charge-transfer kinetics at the buried interface rather than altering the bulk semiconductor properties.

In line with this picture, Voc, Jsc, and FF remain relatively stable overall when devices with and without CBz-PAI are compared, variations are modest and within the configuration-to-configuration spread which further supports the conclusion that CBz-PAI acts primarily by suppressing interfacial recombination current $J_{0,\,int}$ and fine-tuning interfacial band alignment, rather than by changing bulk transport or radiative limits. Thus, to streamline the subsequent optimization, we select the configuration that delivers the highest PCE, namely PET/AZO/ZrS_2/$(FAPbI_3)_{0.77}(MAPbBr_3)_{0.14}(CsPbI_3)_{0.09}$/CZGS/MXene, as the most promising architecture. Focusing on this stack enables a targeted parametric study wherein we fine-tune layer thicknesses, defect density (Nt) in the transport and interfacial regions, parasitic

resistances (R_s, R_{sh}), and interface-specific defect states, with the dual objective of maximizing efficiency while maintaining or improving other critical PV metrics.

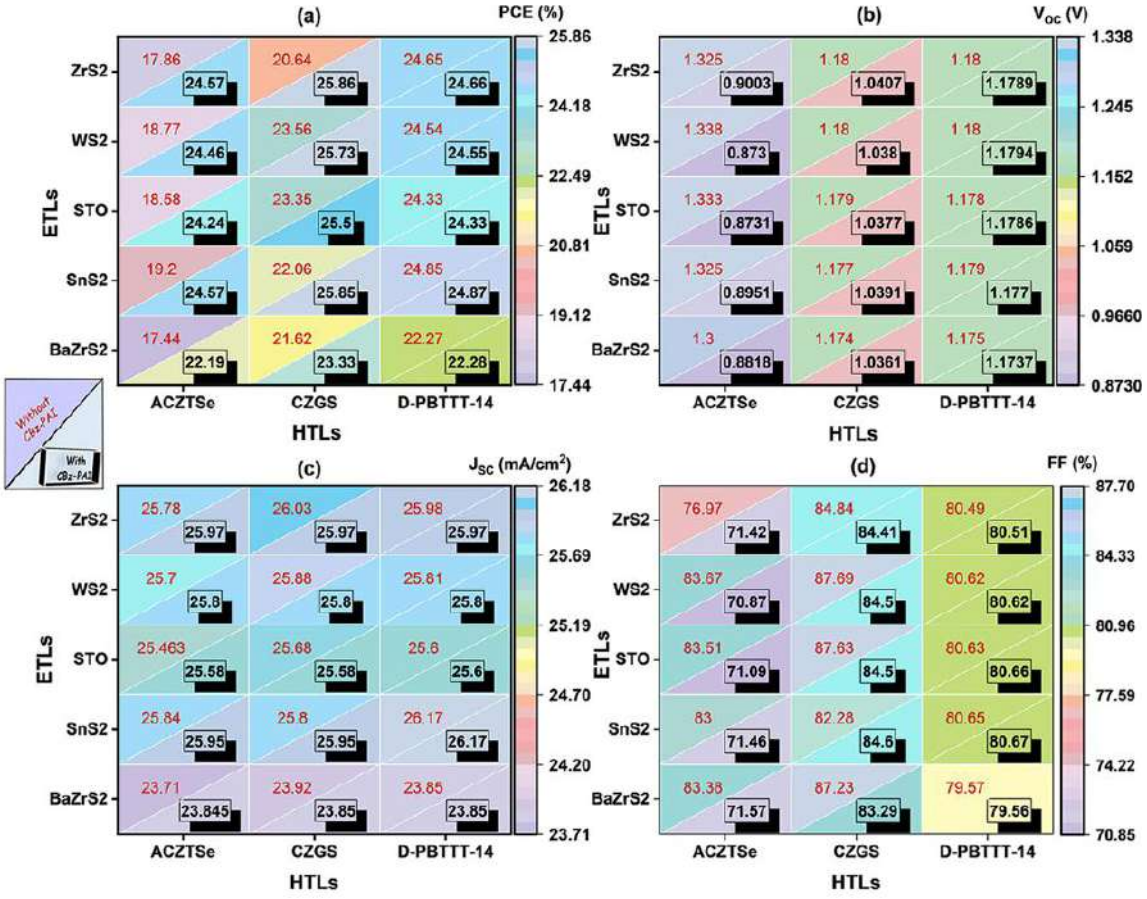


Figure III.4 Heat-map of average PV performance of FPSC devices on n-i-p structure (PET/AZO/ETL/$(FAPbI_3)_{0.77}(MAPbBr_3)_{0.14}(CsPbI_3)_{0.09}$/HTL/MXene) without CBz-PAI passivation interlayer, a) PCE, b) V_{OC}, c) J_{SC}, and d) FF.

III.4 Effect of Layer Thickness and Interfacial Layers on FPSC Performance

As illustrated in Figure III.5, a systematic thickness sweep was performed by varying the thicknesses of the ETL (ZrS_2), HTL (CZGS), and TCO (AZO) within the range of 0.1 - 0.8 µm, while adjusting the thickness of the interfacial passivation layer 2D-PVK (CBz-PAI) between 0.01 - 0.1 µm, in order to evaluate their direct impact on the photovoltaic performance indicators. The results revealed that all parameters PCE, V_{OC}, J_{SC}, and FF reached their highest values at the smallest tested thicknesses across all layers. This can be explained by the fact that thinner transport and interfacial layers reduce the carrier transport distance, thereby lowering the probability of recombination, while simultaneously minimizing parasitic absorption in ETL /HTL / TCO and allowing more photons to reach the perovskite absorber, which enhances V_{OC},

J_{SC}, and FF are closely linked to recombination losses and series resistance, the reduction of the reverse saturation current (J_0) and the decrease in interfacial resistance at smaller thicknesses directly translate into significant improvements in these two parameters. Conversely, increasing the thickness of any of these layers (within 0.1 - 0.8 µm for ETL / HTL / TCO and 0.01 - 0.1 µm for the interlayer) extends the carrier transport path and increases resistive and interfacial losses, ultimately leading to a reduction in efficiency. Therefore, the optimal condition identified in this sweep is to maintain minimal thicknesses for all transport and passivation layers within the specified limits, achieving the optical electrical balance observed in Figure III.5, where PCE, V_{OC}, J_{SC}, and FF were maximized at the smallest studied values.

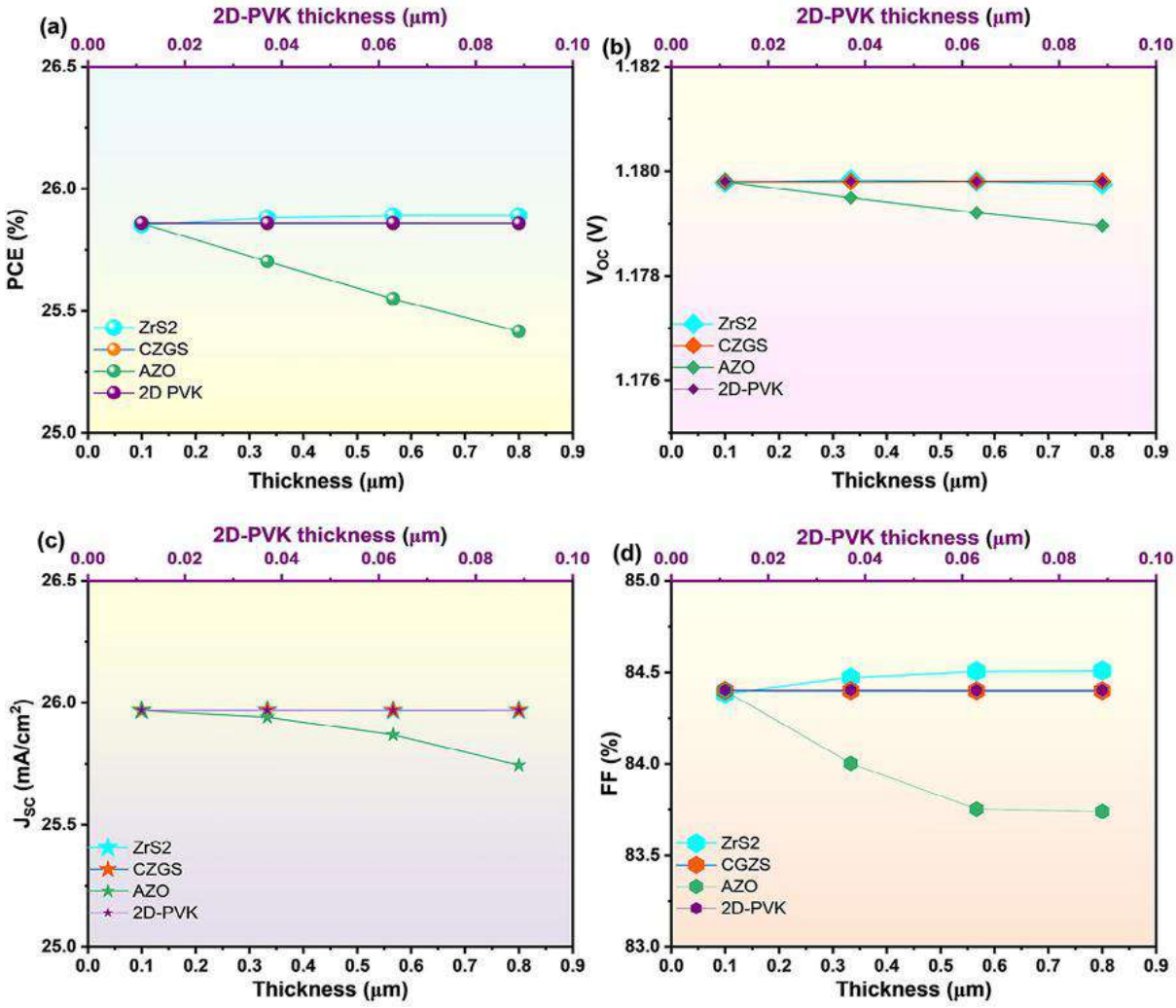


Figure III.5 Analysis of Photovoltaic Parameters (PCE, V_{OC}, J_{SC}, and FF) for a FPSC: Impact of Thickness Variation in 2D-PVK Passivation Interlayer (CBz PAI), ETL (ZrS_2), and HTL (CZGS), and on Solar Cell Efficiency.

III.5 Influence of Absorber Thickness and Defect Density on FPSC Performance

The control of both absorber thickness and defect density (Nt) represents a fundamental factor in determining the photovoltaic performance of flexible perovskite solar cells (FPSCs). The thickness was varied between 0.1 and 0.75 µm, while the defect density was adjusted within the range of 5×10^{13} - 1×10^{16} cm^{-3}, in order to systematically analyze their impact on the main photovoltaic parameters, namely power conversion efficiency (PCE), open-circuit voltage (Voc), short-circuit current density (Jsc), and fill factor (FF).

The simulation results (Figure III.6) revealed that the highest PCE of 27.14% was obtained at

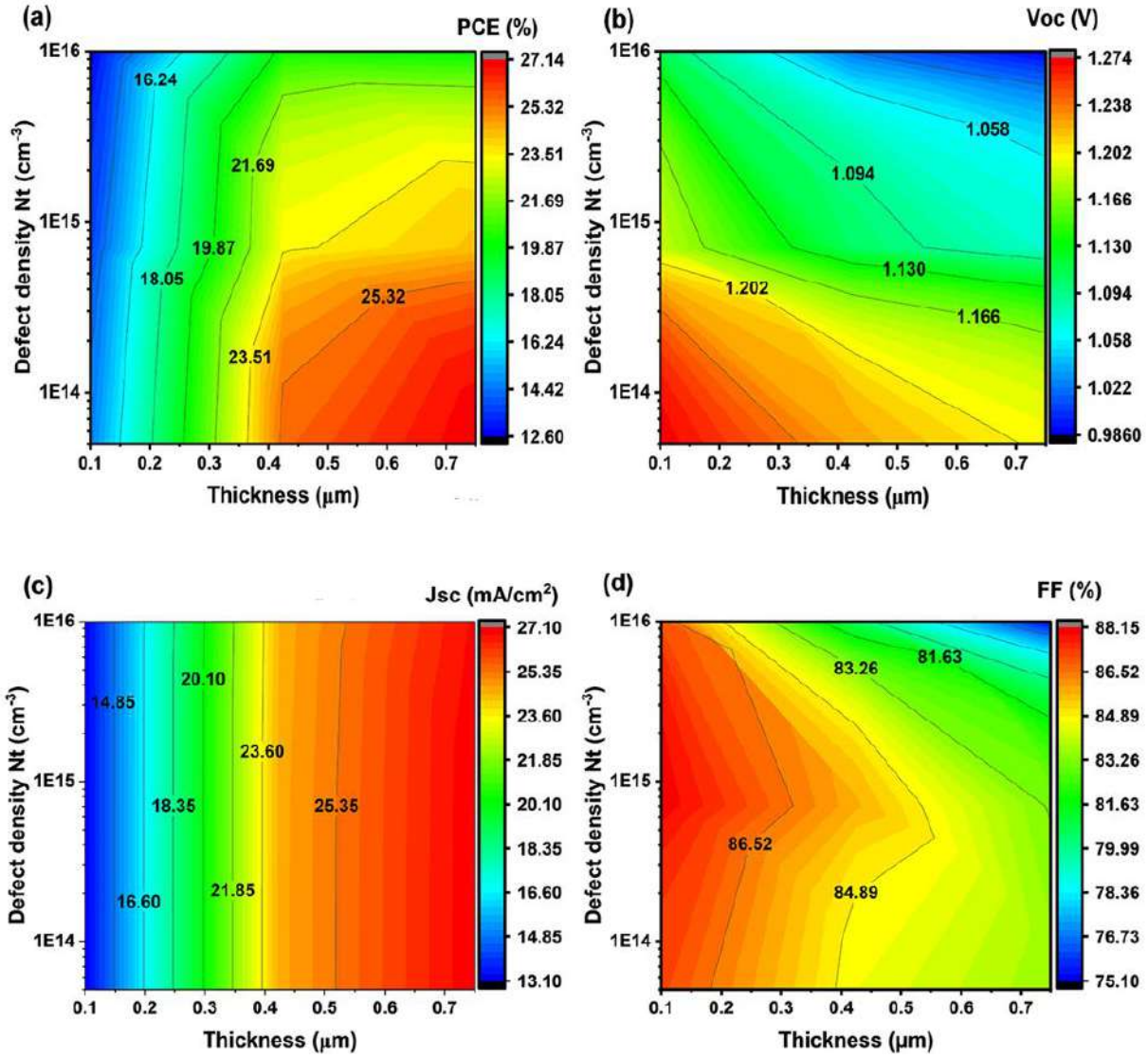


Figure III.6 Contour mapping of PV performances due to the effect of thickness and interface defect density Nt of 3D-PVK $((FAPbI_3)_{0.77}(MAPbBr_3)_{0.14}(CsPbI_3)_{0.09})$ absorber layer.

Nt = 5×10^{13} cm^{-3} combined with absorber thicknesses exceeding 0.5 µm. This improvement reflects the synergistic effect of increased optical absorption in thicker layers and the suppression of non-radiative recombination when defect density is minimized, thereby enabling more efficient charge carrier generation and extraction.

Conversely, when absorber thickness exceeded 0.4 µm while defect density reached Nt = 1×10^{16} cm^{-3}, both Voc and FF drastically decreased from 1.27 V to 0.99 V and from 88.15% to 75.10%, respectively, resulting in a significant reduction of PCE to nearly 12.60%. This degradation is attributed to the high density of recombination centers acting as traps, which severely hinder charge transport and extraction efficiency.

On the other hand, Jsc exhibited a maximum of 57.8 ($mA.cm^{-2}$) for absorber thicknesses greater than 0.4 µm. This rise is primarily explained by enhanced photon absorption in thicker absorber volumes, which increases the generation of electron–hole pairs. Nevertheless, the beneficial effect of thickness is strongly dependent on maintaining low defect densities to prevent recombination losses from dominating the overall device performance.

III.6 Effect of Parasitic Resistances (Rs and Rsh) and Working Temperature on FPSC Performance

Parasitic resistances, namely the series resistance (R_s) and shunt resistance (R_{sh}), represent critical limiting factors in the overall efficiency of flexible perovskite solar cells (FPSCs), as they directly influence charge transport, recombination, and leakage mechanisms. Ideally, high-performance devices require R_s values below 1 $\Omega.cm^2$ to guarantee unhindered carrier transport through the device, while R_{sh} values above 10^7 $\Omega.cm^2$ are necessary to suppress leakage currents arising from pinholes, interface imperfections, or alternative shunt pathways within the cell.

In this work, R_s was varied from 0 to 10 $\Omega.cm^2$ and R_{sh} from 10^4 to 10^{10} $\Omega.cm^2$, and the effect on photovoltaic metrics power conversion efficiency PCE, open-circuit voltage Voc, short-circuit current density Jsc, and fill factor FF was systematically analyzed using contour plots Figure III.7. The simulations revealed that increasing R_s to 8 $\Omega.cm^2$ led to a substantial efficiency loss, with PCE decreasing from ~26% to ~20% and FF from 84% to 64%. This decline stems from additional ohmic losses at the electrode–transport layer interfaces, which dissipate useful power as heat and distort the current-voltage J-V curve, reducing its squareness. Conversely, variations in Rs and Rsh had minimal influence on Voc and Jsc. Voc remained stable because it is primarily determined by the built-in potential and energy band alignment,

which are not directly altered by series or shunt resistances. Similarly, Jsc exhibited negligible changes since carrier generation and collection processes are preserved as long as transport layers remain efficient.

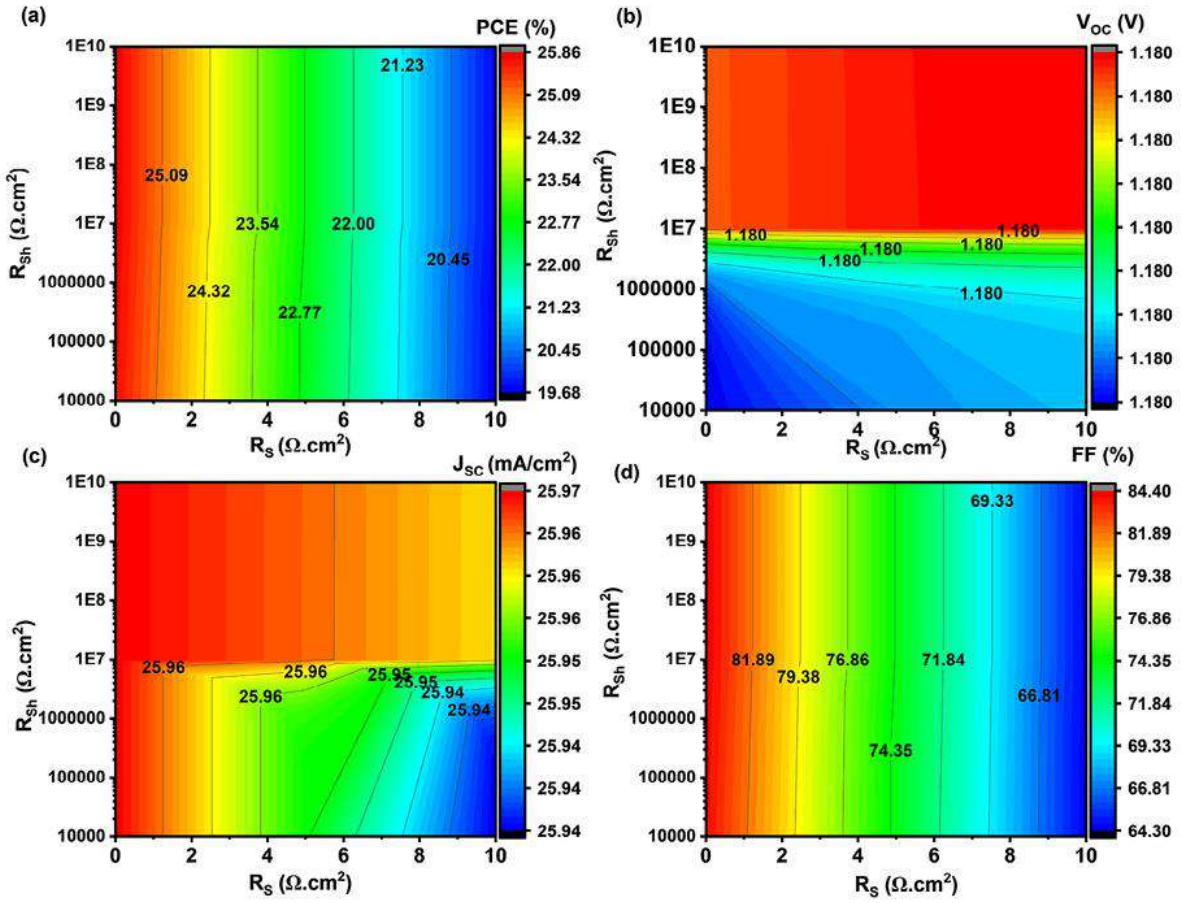


Figure III.7 Contour mapping of PV performances due to the impact of R_S and R_{Sh}.

The effect of operating temperature in Figure III.8.a was also investigated, covering a range from 270K to 450K. As the temperature increased, device performance deteriorated significantly. The PCE dropped from 27% to 19%, Voc declined from 1.20 V to 0.90 V, and FF decreased from 86% to 75%. These losses are attributed to enhanced thermal excitation of charge carriers at higher temperatures, which accelerates non-radiative recombination processes, particularly through defect states, thereby lowering carrier lifetime and effective extraction. Interestingly, Jsc exhibited a marginal increase from 22.968 to 22.976 ($mA.cm^{-2}$). This slight enhancement can be attributed to the increased carrier mobility induced by thermal activation, which improves charge transport and collection despite the concurrent rise in recombination losses. Overall, these results confirm that parasitic resistances primarily impact FF and PCE, while their influence on Voc and Jsc remains secondary. Furthermore, thermal

effects represent a major degradation pathway for FPSCs, underscoring the urgent need for efficient thermal management strategies such as encapsulation, heat dissipation layers, or thermally robust transport materials to ensure operational stability and preserve efficiency under realistic working conditions.

III.7 Impact of the Work Function of Back Contact on FPSC Performances

The selection of an appropriate back contact plays a critical role in determining the photovoltaic performance of flexible perovskite solar cells (FPSCs). Recently, MXene-based materials have emerged as highly promising candidates due to their unique properties, including excellent electrical conductivity, optical transparency, high transmittance, chemical stability, and remarkable mechanical robustness. In 2018, Guo et al. demonstrated that the incorporation of MXene layers into perovskite solar cells significantly enhanced the power conversion efficiency (PCE), thereby opening new perspectives for interface engineering in PSCs.

In the present study, three different MXenes with work functions ranging from 5.0 to 5.65 eV were investigated to identify the most suitable back contact. As illustrated in Figure III.8b, an increase in the MXene work function exhibited a direct correlation with device efficiency. The maximum PCE of 25.88% was obtained with $V_3C_2F_2$, which possesses the highest work function of 5.65 eV.

This improvement can be rationalized by the favorable energy level alignment at the back interface. Specifically, the work function of the 3D-perovskite (3D-PVK) is -5.46 eV, which aligns closely with that of Poly-TPD - 4.95 eV and the valence band maximum of the 2D-PVK interlayer -5.47 eV. Such energetic compatibility minimizes potential barriers at the HTL/perovskite/MXene interfaces, thus facilitating efficient hole extraction. Moreover, the utilization of a high-work-function MXene promotes band bending at the MXene/semiconductor interface, which lowers the Fermi level and contributes to the formation of an ohmic contact. This process enhances carrier collection efficiency and significantly reduces resistive losses within the device.

Consequently, the optimized FPSC configuration was identified as:

PET/AZO/ZrS_2/$(FAPbI_3)_{0.77}(MAPbBr_3)_{0.14}(CsPbI_3)_{0.09}$/CBz-PAI/CZGS/$V_3C_2F_2$

This optimized device architecture emphasizes the decisive role of the back contact in FPSC design, showing that careful selection of high-work-function MXenes is a powerful strategy to enhance photovoltaic performance by enabling efficient charge extraction, minimizing interfacial energy losses, and stabilizing the device operation.

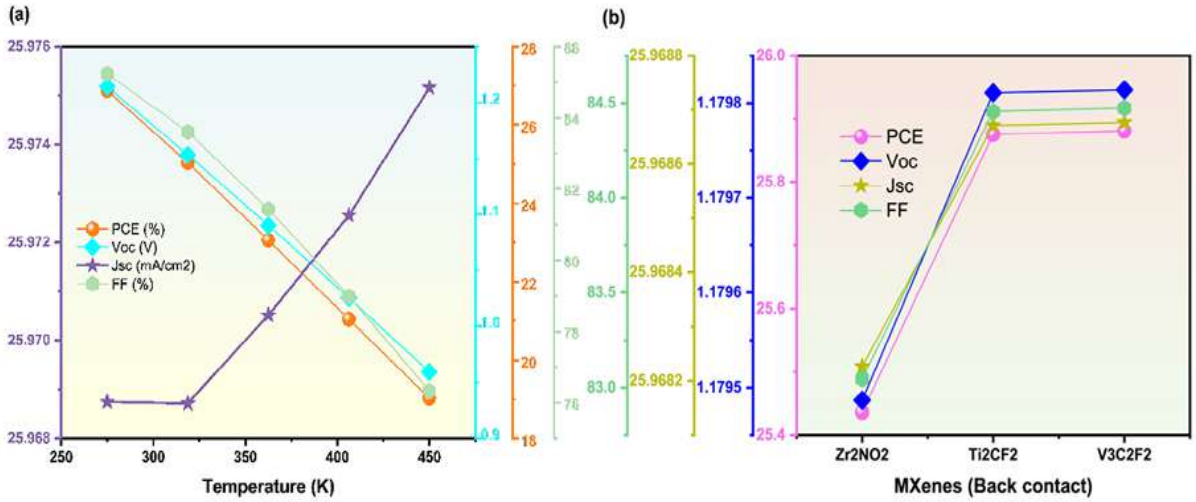


Figure III.8 Variation of FPSC PV parameters as a function of a) temperatures, b) Work function of different MXenes used for left (back) contact.

III.8 Optimized Device

During the study, the optimal parameters for FPSCs were determined, focusing on the thicknesses of key layers and defect densities N_t. The ideal thicknesses identified for achieving the highest PCE were 0.75 µm for the 3D-PVK ($(FAPbI_3)_{0.77}(MAPbBr_3)_{0.14}(CsPbI_3)_{0.09}$) layer, 0.01 µm for the 2D-PVK interlayer (CBz-PAI) layer, 0.1 µm for the ETL (ZrS_2), for HTL (CZGS) and TCO (AZO) layer. In addition to optimizing layer thicknesses, the study also pinpointed the critical N_t at the interfaces of the 3D-PVK layer, which was found to be 5×10^{13} cm^{-3}. This low Nt is essential for minimizing recombination losses, thereby contributing significantly to maximizing the PCE of the FPSCs.

The J-V characteristics comparison between the initial and optimized flexible PSCs is presented in Figure III.8a, highlighting the enhanced efficiency of the optimized FPSC, which incorporates a CBz-PAI interlayer, which is clearly demonstrated. This optimized device, featuring a PET/AZO/ZrS_2/$(FAPbI_3)_{0.77}(MAPbBr_3)_{0.14}(CsPbI_3)_{0.09}$/CBz-PAI/CZGS/MXene-$V_3C_2F_2$

structure, shows significant improvements in key PV parameters. Specifically, the Voc increased from 1.04 to 1.20 V, the Jsc rose from 26.05 to 27.27 mA cm^{-2}, and the PCE improved markedly from 22.98% to 27.18%. Although the FF experienced a slight decrease, from 84.84% to 83.65%, the overall performance enhancements are substantial. Similarly, the final optimized

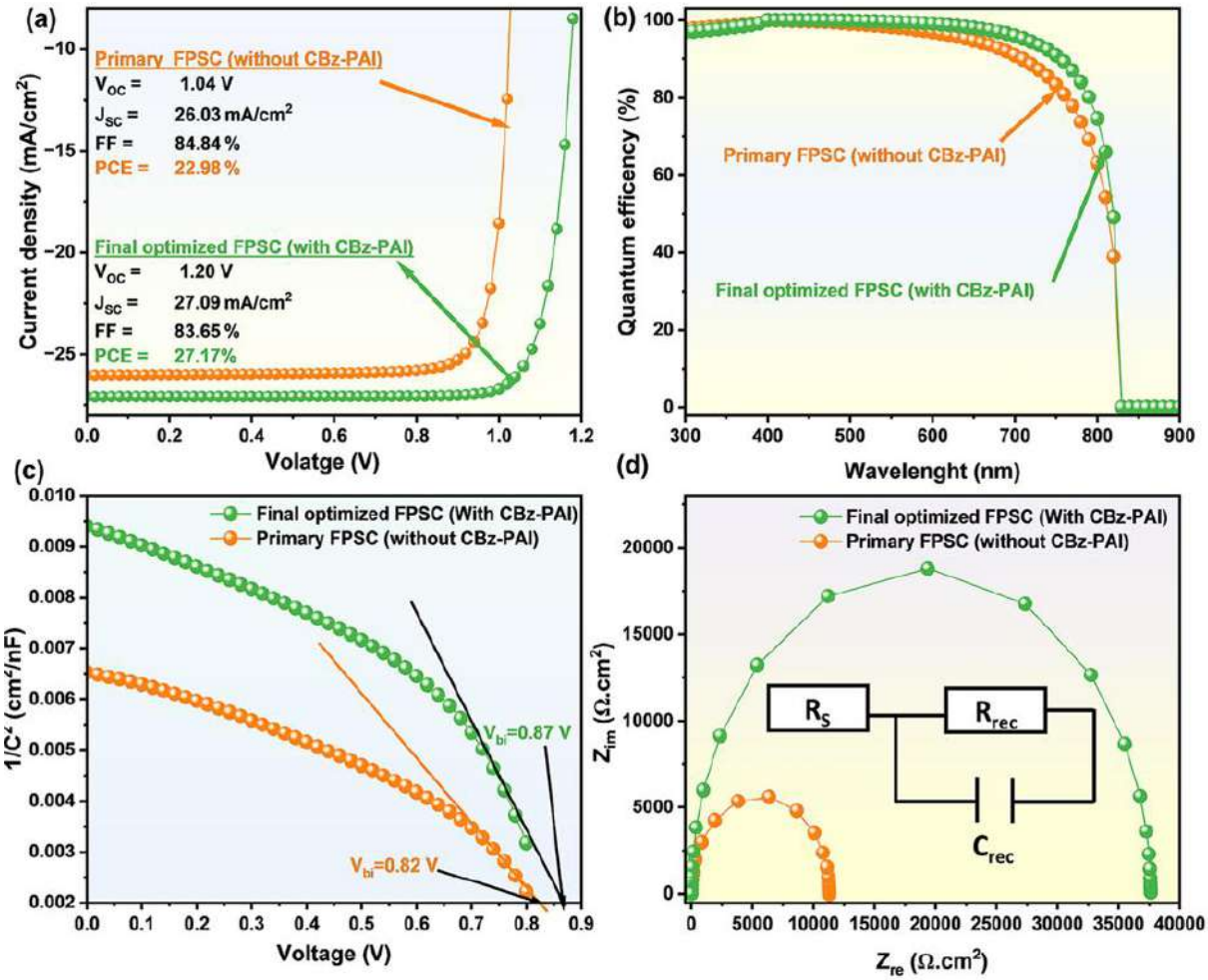


Figure III.9 a) J-V curves with PV parameters presented in the inset, b) QE, c) Mott–Schottky plot, and d) Nyquist plots of the initial (without CBz-PAI interlayer) and final (with CBz-PAI interlayer) FPSCs.

FPSC shows a significant enhancement in the quantum efficiency (QE) across the wavelength range of 400 to nearly 700 nm as shown in Figure 8b. These improvements can be attributed not only to the optimized parameters but also to the positive impact of the CBz-PAI interlayer, which effectively reduces recombination at the interfaces, thereby enhancing device performance. Additionally, the incorporation of MXene as the back contact, known for its excellent physical properties, further contributes to the improved performance by serving as a superior alternative to conventional electrodes.

The built-in potential (V_{bi}), a critical parameter for driving the separation of photo-generated electrons and holes in opposite directions, can be extracted from the Mott–Schottky plot or C-V measurements. Figure III.8c illustrates the Mott–Schottky plot used in this analysis. The

obtained Vbi values are 0.85 and 0.87 V for the primary and final FPSCs devices, respectively (see Figure III.8c). The higher Vbi of the Optimized FPSC device indicates a stronger driving force for charge separation and reduced recombination at the 3D-PVK/2D-PVK interface compared to the 3D-PVK/HTL interface in the primary device, resulting in a higher Voc.

The Nyquist plots provide valuable insights into the electrical impedance (Z) of the devices across various frequencies, where the impedance is a complex quantity consisting of both resistance (R) and reactance (imaginary resistance). This parameter is essential for assessing internal resistances within the devices and is examined using SCAPS 1D to provide a clearer understanding of their electrical behavior. In these plots, FPSCs are modeled as constant phase elements (CPE) arranged in parallel with the recombination resistance (R_{rec}). The R_{rec} represents the charge recombination capability at the interface between the ETL and the perovskite layers, while the series resistance (R_s).

This accounts for resistive losses in the TCO (AZO), the MXene, and other bulk resistances, the equivalent circuit model presented in the inset of Figure III.9d. Figure III.9d illustrates that the semicircle diameter for the final optimized FPSC device is significantly larger than that of the initial device, indicating more efficient hole transport and reduced recombination at the perovskite/HTL interface, this observation aligns with findings in the literature.

Table III.3 Experimental and theoretical efficiencies for FPSCs reported in literature with a comparison of our study.

Devices	**Voc**	**Jsc**	**FF**	**PCE**	**Ref**
Unitis	**V**	**mA.cm^{-2}**	**%**	**%**	
PET/AZO/ZnO-NRs/$CH_3NH_3SnI_3$: xLn^{+3}/PTAA/Au	1.34	22.08	83.95	25.85	[129]
PET/ITO/SnO_2/2D/3D/Spiro/Au	1.15	25.26	76.58	22.30	[150]
PEN/ITO/SnO_2/$(CsPbI_3)_{0.06}((FAPbI_3)_{0.90}(MAPbBr_3)_{0.10})_{0.95}$/LD perovskite/spiro-OMeTAD/Au	1.15	23.5	77.4	21.00	[151]
PET/AgNW/$Ti_3C_2T_x$/MXene/ICSO4$FA_{0.6}MA_{0.4}PbI_3$/PCBM/BPhen/Ag	1.06	25.16	75.52	20.22	[152]
PET/AZO/ZrS_2/$(FAPbI_3)_{0.77}(MAPbBr_3)_{0.14}(CsPbI_3)_{0.09}$ /CBz PAI/ CZGS/MXene-$V_3C_2F_2$	**1.20**	**27.09**	**83.65**	**27.17**	**This study**

Table III.3 demonstrates a comprehensive comparison of the photovoltaic performance between reported experimental and theoretical results for flexible perovskite solar cells, with a specific focus on devices utilizing flexible substrates. The proposed PET/AZO/ZrS_2/$(FAPbI_3)_{0.77}(MAPbBr_3)_{0.14}(CsPbI_3)_{0.09}$/CBz-PAI/CZGS/MXene-$V_3C_2F_2$ device architecture, which incorporates the CBz-PAI interlayer at the perovskite/HTL interface, achieves the highest experimental PCE of 27.17%, a promising result that surpasses the efficiencies reported in previous works in literature, as shown in Table III.3.

Notably, Dubey et al. theoretically reported the use of a lanthanide-doped perovskite absorber (Ln^{+3}: $MAPbI_3$), with a 1.3 eV bandgap, which absorbed more photons than the perovskite in our present work (with an energy gap above 1.5 eV). However, their theoretical work achieved a PCE of ≈26%, while our proposed device delivered the highest experimental efficiency (above 27%). In contrast, Yang et al. in their experimental work on 2D/3D heterostructure perovskite composites (using amidino-based Dion-Jacobson 2D-perovskites combined with 3D-perovskites), achieved an experimental efficiency of ≈ 22%.

This is lower than the performance of our proposed device, which emphasizes the importance of selecting suitable ETL, HTL, and TCO materials to maximize PCE. Similarly, Dong et al. experimentally developed a low-dimensional (LD) metal-halide perovskite (MHP) thin capping layer deposited over the 3D MHP light absorber in FPSCs. This approach led to remarkable improvements in operational stability (T90, with over 800 h of retention of 90% of the initial PCE), bending durability (T80 = 20,000 tension-only bending cycles), and achieved a good experimental PCE of 21.0%.

These results suggest that further advancements in this approach can potentially surpass the PCE achieved in our work. Furthermore, Chet al. experimentally developed flexible transparent electrodes (FTEs) by merging AgNWs with 2D transition-metal carbide ($Ti_3C_3T_x$ MXene) for integration in PSCs. Their experimental work on AgNW-based PSCs achieved a PCE of 20.22% with improved stability and mechanical properties for flexible devices.

Conclusion:

The performance of flexible PSCs is investigated in this study, by focusing on the effects of the CBz-PAI interlayer at the perovskite absorber/HTL interface, through drift-diffusion simulations conducted with SCAPS 1D. Initially, to extract the suitable architecture of FPSCs with the maximum photovoltaic performance, we tested 50 configurations to select the most suit able ETL ssuchas $BaZrS_3$, SnS_2, STO, WS_2, and ZrS_2 and various materials HTLs, including ACZTSe, $CuBiS_3$, CZGS, D-PBTTT 14, and Se/Te: Cu_2O. Subsequently, we integrated the CBz-PAI interlayer into appropriate configurations, which established that devices with CBz-PAI achieved a higher PCE compared to standard configurations. This enhancement is attributed to the interlayer's ability to enhance interface quality by reducing interfacial charge carrier recombination at the perovskite/HTL interface, thereby minimizing VOC losses. Later, after extracting the optimal restrictions and the incorporation of the most suitable MXene as back contact, the appropriate FPSC structure ($PET/ITO/AZO/ZrS_2/(FAPbI_3)_{0.77}(MAPbBr_3)_{0.14}(CsPbI_3)_{0.09}$/CBz-PAI/CZGS/MXene-$V_3C_2F_2$) establishes a maximum efficiency of 27.17%, which is a promising result.

Chapter

IV

Bifacial Perovskite Solar Cells

The primary objective of this chapter is to design and numerically investigate bifacial perovskite solar cells (b-PSCs) by means of SCAPS 1D simulations. The study focuses on:

- Evaluating the impact of different electron transport layers (ETLs) and hole transport layers (HTLs) on device performance under dual-side illumination.
- Investigating the role of a 2D-perovskite (2D-PVK) interlayer in passivating interface defects and enhancing charge extraction in combination with a 3D-perovskite (3D-PVK) absorber.
- Performing parametric analyses to study the influence of layer thicknesses, defect densities (Nt), carrier concentrations (N_D, N_A), and operating temperature.

This objective builds on the outcomes of Chapter III (Flexible PSCs) and extends the investigation towards bifacial architectures, providing a broader understanding of perovskite device design strategies for next-generation photovoltaics.

Introduction

In Chapter III, flexible perovskite solar cells (Flexible PSCs) were examined as promising devices for lightweight and portable applications. The study highlighted the role of novel hole and electron transport layers, as well as interfacial engineering strategies, in improving the photovoltaic performance of such single-side illuminated architectures. However, despite their potential for wearable and flexible electronics, flexible PSCs remain inherently limited by their inability to utilize incident light from both sides of the device, which restricts their overall energy harvesting capability in large-scale applications.

Building upon these findings, the present chapter shifts the focus towards bifacial perovskite solar cells (b-PSCs). This emerging architecture enables light absorption from both the front and rear sides by incorporating transparent electrodes and carefully engineered transport layers. Such devices provide an opportunity to increase the energy yield per unit area and to enhance the competitiveness of perovskite photovoltaics with respect to conventional bifacial silicon modules.

To this end, this chapter proposes and numerically investigates a 2D/3D hybrid perovskite configuration. The structure combines a three-dimensional perovskite (3D-PVK) absorber with a thin two-dimensional perovskite (2D-PVK) interlayer, which is expected to suppress non-radiative recombination and improve charge extraction at critical interfaces. Several electron transport layers (ETLs) and hole transport layers (HTLs) are systematically explored using SCAPS 1D simulations. Furthermore, parametric analyses are conducted to evaluate the impact of layer thicknesses, defect densities (Nt), doping concentrations (N_D, N_A), and operating temperature on bifacial device behavior.

This introduction therefore establishes the rationale and framework for the subsequent analysis and discussion, positioning bifacial perovskite solar cells as a complementary research pathway to flexible devices, with distinct advantages for next-generation photovoltaic applications.

IV.1 Selection of Materials and Parameters for Simulation

The selection of materials for each layer in the proposed bifacial perovskite solar cell (b-PSC) structure was guided by strict physical, electronic, and optical criteria. Particular emphasis was placed on ensuring efficient dual-side light harvesting, requiring transparent electrodes with high conductivity and optical transmittance, as well as absorber layers with optimal band gap values for broad-spectrum absorption. Additional considerations included appropriate energy-level alignment for efficient charge extraction, high carrier mobility, low defect densities to suppress non-radiative recombination, and robust chemical and thermal stability. These requirements are crucial for enabling the integration of hybrid 3D/2D perovskite absorbers with selective transport layers and transparent contacts suitable for bifacial operation.

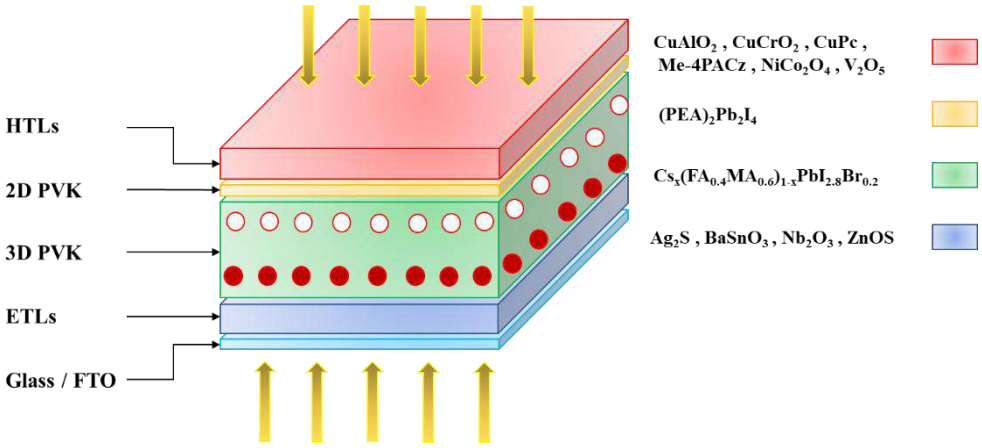


Figure IV.1 Layered Structure of bifacial Perovskite Solar Cell : FTO Substrate, ETL ($BaSnO_3$, Nb_2O_5, ZnOS, Ag_2S), 3D-PVK Layer, 2D-PVK Interlayer Passivation, and HTL (Me-4PACz, $CuAlO_2$, $CuCrO_2$, CuPc, $NiCo_2O_4$, V_4O_5)

IV.1.1 Physical and Electronic Properties of Selected Materials

Table IV.1, Table IV.2 provides a summarized overview of the essential physical and electronic properties of the materials employed in the bifacial solar cell configuration. The selection of these materials was motivated by their ability to enhance charge transport, minimize interfacial losses, and ensure effective dual-side operation. The absorber layer combines three-dimensional (3D) perovskite with a two-dimensional (2D) passivation layer to mitigate defect-assisted recombination and improve long-term stability. In addition, a variety of electron transport layers (ETLs) and hole transport layers (HTLs) were considered based on their band alignment, transparency, and process compatibility. This comprehensive material set forms the foundation for the numerical simulations carried out with the SCAPS 1D tool.

Table IV.1 Input parameters for TCO, ETL, 3D-PVK($C_{SX}(FA_{0.4}\ MA_{0.6})_{1-x}\ PbI_{2.8}\ Br_{0.2}$), χ: electron affinity, ϵ: dielectric permittivity, C_B: conduction band effective densityof states, V_B: valance band effective density of states, μ_p: electron mobility, μ_N: hole mobility.

Parametre	TCO	ETLs				Absorber layer
	FTO	$BaSnO_3$	Nb_2O_5	ZnOS	Ag_2S	3D-PVK
Thickness(nm)	10	50	20	25	20	500
Eg (eV)	3.5	3.5	3.4	2.83	1.46	1.6
X(eV)	4	3.8	3.9	3.6	4.5	3.9
ϵr (eV)	9	17	10	9	10	6.5
$C_b\ (cm^{-3})$	1.00×10^{19}	$2.00\ E{+}17$	$2.20\ E{+}18$	$2.2\ E{+}18$	$2.00\ E{+}18$	$1.00\ E{+}17$
$V_b\ (cm^{-3})$	$1.00\ E{+}19$	$1.200\ E{+}18$	$1.8\ E{+}19$	$1.80\ E{+}19$	$1.50\ E{+}19$	$1.00\ E{+}17$
$\mu_n\ (cm^2V{-}1s{-}1)$	$1.00\ E{+}2$	150	20	100	50	2
$\mu p\ (cm^2V{-}1s{-}1)$	$2.50\ E{+}1$	150	0.1	25	20	2
$N_D\ (cm^{-3})$	$2.00\ E{+}19$	$1.00\ E{+}22$	$1.00\ E{+}16$	$1.00\ E{+}18$	$1.00\ E{+}7$	0
$N_A\ (cm^{-3})$	0	$1.00\ E{+}21$	0	0	0	$1.00\ E{+}13$
$Nt\ (cm^{-3})$	$1.00\ E{+}14$	$2.00\ E{+}16$	$1.00\ E{+}15$	$1.00\ E{+}15$	$1.00\ E{+}15$	$1.00\ E{+}14$
Referance	[153]	[154]	[155]	[156],[157]	[158]	[159]

Table IV.2 Input parameters for 2D-PVK (PEA2-Pb_2I_4), and organic and inorganic HTLs,

Parametre	Inter layer passivation	HTL				
	2D-PVK	$CuAlO_2$	Me-4PACz	$NiCo_2O_4$	CuPc	$CuCrO_2$
Thickness (nm)	20	150	100	70	100	100
Eg (eV)	2.4	3.46	3.3	2.3	17	3.3
X(eV)	3	2.5	2.5	3.48	3.5	3.5
ϵr (eV)	5	60	10	11.9	10	10

C_b (cm^{-3})	1.010 E^{+18}	2.20 E^{+18}	1.00 E^{+19}	2.20 E^{+18}	4.386 E^{+19}	4.386 E^{+19}
V_b (cm^{-3})	1.010 E^{+19}	1.80 E^{+19}	1.00 E^{+19}	1.00 E^{+19}	4.343 E^{+18}	4.343 E^{+18}
μ_n ($cm^2V{-}1s{-}1$)	2.00 E^{-4}	2	50	1.05	7.7	7.7
μ_p ($cm^2V{-}1s{-}1$)	2.00 E^{-4}	8.6	50	1.61	7.7	7.7
N_D (cm^{-3})	0	0	0	0	0	0
N_A (cm^{-3})	1.50 E^{+17}	3.00 E^{+18}	2.00 E^{+18}	1.00 E^{+18}	1.00 E^{+18}	1.00 E^{+18}
N_t (cm^{-3})	2.50 E^{+14}	1.00 E^{+15}	1.00 E^{+13}	1.00 E^{+15}	1.00 E^{+14}	1.00 E^{+14}
Reference	**[160]**	**[161]**	**[162]**	**[163]**	**[164]**	**[161]**

IV.1.2 Detailed Description of Selected Materials

- **Transparent Conducting Oxide (TCO):** Fluorine-doped Tin Oxide (FTO) Fluorine-doped tin oxide (FTO) is one of the most widely used transparent conducting oxides in photovoltaic applications. It combines high optical transmittance (>80% in the visible range) with low sheet resistance, ensuring efficient current collection. For bifacial operation, FTO is particularly suitable due to its chemical stability and wide band gap, which minimizes parasitic absorption and enables efficient dual-side light harvesting.[165]
- **Absorber Layer: 3D-Perovskite ($CSx(FA_{0.4}MA_{0.6})_{1-x}PbI_{2.8}Br_{0.2}$) :**The proposed 3D-perovskite absorber is based on a mixed cation/halide composition combining Cs^+, FA^+, and MA^+ partially substituted with Br^-. Such mixed formulations have been shown to enhance phase stability, improve crystallinity, and yield an optimal band gap (~1.55-1.60 eV) close to the Shockley-Queisser limit. Cesium incorporation suppresses unwanted phase transitions, while bromide addition further stabilizes the perovskite lattice and reduces non-radiative losses.[166]
- **2D-Perovskite Passivation Layer ($PEA_2Pb_2I_4$):** Two-dimensional perovskites, such as $PEA_2Pb_2I_4$, act as surface passivation layers in hybrid 2D/3D absorber structures. The insertion of a 2D-perovskite mitigates trap states at the interface, suppresses non-radiative recombination, and improves open-circuit voltage (Voc) and fill factor (FF). In addition, the hydrophobic phenylethylammonium (PEA^+) spacer enhances environmental stability by providing moisture resistance. These advantages have been widely demonstrated in recent studies exploring 2D/3D hybrid perovskite devices.[167]

- **Electron Transport Layers (ETLs)**

  a. **$BaSnO_3$:** This perovskite oxide (Eg ≈ 3.1 eV) exhibits high electron mobility and excellent chemical stability. Studies have demonstrated its effectiveness as an ETL in perovskite solar cells, with potential for high performance and low-temperature processability.[168]
  b. **Nb_2O_5:** A wide-band-gap oxide with a high dielectric constant, Nb_2O_5 serves as an efficient electron-selective material while providing UV resistance, outperforming conventional TiO_2 under prolonged illumination.
  c. **ZnOS:** A modified zinc oxide material incorporating sulfur, ZnOS offers tunable conduction band alignment, reduced surface states, and excellent transparency, making it a strong ETL candidate.[169]
  d. **Ag_2S:** A chalcogenide semiconductor that has been engineered in nanostructured form to improve charge extraction and interfacial light absorption, further enhancing device performance.[170]

- **Hole Transport Layers (HTLs)**

  a. **$CuAlO_2$:** A transparent delafossite oxide with p-type conductivity, showing suitable valence band alignment with perovskite absorbers and high thermal stability.[171]
  b. **Me-4PACz:** A self-assembled monolayer (SAM) that has recently emerged as an efficient HTL. It enhances interfacial energy alignment, reduces non-radiative recombination, and improves long-term device stability[172].
  c. **$NiCo_2O_4$:** A p-type spinel oxide with high conductivity, low-cost synthesis, and excellent stability, increasingly investigated as a robust HTL alternative.[173]
  d. **CuPc:** Copper phthalocyanine is a thermally stable organic HTL with favorable energy alignment, widely used in thin-film solar cells.[174]
  e. **$CuCrO_2$:** Another delafossite oxide with a wide band gap and high optical transparency, $CuCrO_2$ provides efficient hole transport and long-term operational stability .[175]

IV.2 Results and Discussion

Simulations were performed using SCAPS1D (version 3.3.12) to evaluate the performance of bifacial perovskite solar cells by analyzing the influence of four electron transport layers ETLs and five hole transport layers HTLs . In total, 40 device configurations were investigated, and the results were visualized using a heat map Figure IV.2 to highlight the emerging performance trends. In this representation, downward triangular markers correspond to the power conversion efficiency (PCE) under front-side illumination, whereas upward triangular markers denote the PCE under rear-side illumination. The primary purpose of this analysis is to compare the photovoltaic response across different ETL/HTL combinations.

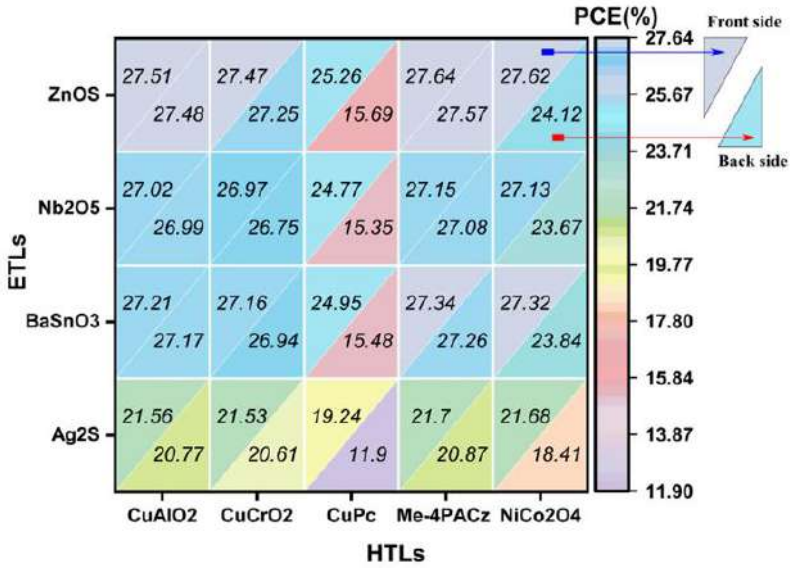


Figure IV.2 Heat-maps for different configurations of bifacial perovskite solar cells.

The results revealed that the use of ZnOS as the ETL consistently yielded the highest efficiencies under both front and back illumination, regardless of the HTL employed. This superior performance is attributed to the favorable energy-level alignment between ZnOS and the HTLs, which reduces interfacial energy losses and promotes efficient charge separation and transport. Notably, the device incorporating Me-4PACz as the HTL achieved the best overall performance, with a PCE of 27.65% for front-side illumination and 27.57% for rear-side illumination. The nearly identical efficiencies between both sides, combined with the consistently high performance across all ETLs, demonstrate the excellent optoelectronic properties of Me-4PACz and confirm its strong potential as a promising HTL candidate for bifacial perovskite solar cells.

To enable a precise comparative analysis, solar cells exhibiting closely matched front and rear photovoltaic performance were selected, with the bifaciality factor (Bf) serving as the key evaluation metric. These findings are systematically summarized in Table IV.3 Devices employing $CuAlO_2$ as the HTL, when paired with ZnOS and Nb_2O_5 as ETLs, achieved the highest Bf value of 99.89%, indicating near-perfect symmetry. Similarly, the configuration based on $BaSnO_3$ as the ETL combined with $CuAlO_2$ as the HTL demonstrated a high (Bf) of 99.85%, highlighting its well-balanced performance under both front and rear illumination.

Table IV.3 Bifaciality factor of highest performance device configuration for both sides.

Optimized devices	Structure	Illumination side	V_{OC} (V)	J_{SC} (mA/cm^2)	FF (%)	PCE (%)	B_f (%)
FTO/ZnSO/3D-PVK/2D-PVK/Me-4PACz	I	Front side	1.456	22.23	85.38	27.64	**99.75**
		Rear side	1.456	22.13	85.58	27.57	
FTO/ZnSO/3D-PVK/2D-PVK/$CuAlO_2$	II	Front side	1.456	22.23	84.98	27.51	**99.89**
		Rear side	1.456	22.16	85.20	27.48	
FTO/Nb_2O_5/3D-PVK/2D-PVK/$CuAlO_2$	III	Front side	1.453	22.24	83.59	27.02	**99.89**
		Rear side	1.453	22.15	83.84	26.99	
FTO/$BaSnO_3$/3D-PVK/2D-PVK/ $CuAlO_2$	IV	Front side	1.452	22.25	83.94	27.21	**99.85**
		Rear side	1.452	22.15	84.46	27.17	

On the other hand, certain HTL materials, such as $CuCrO_2$ and $NiCo_2O_4$, exhibited reasonable performance, with efficiencies of approximately 26% (front) and 23% (rear), attributed to their chemical stability and favorable energy-level alignment. In contrast, CuPc showed only moderate performance: while the PCE under front illumination reached 25.26%, it dropped drastically to 15.69% under rear illumination, rendering it unsuitable for bifacial solar cells. The weakest performance was observed in all configurations incorporating Ag_2S as the ETL, where the PCE declined from about 22% (front) to only 11% (rear). This degradation is attributed to the narrow bandgap and poor electronic transport properties of Ag_2S, which enhance recombination losses.

These results clearly underscore the crucial role of energy-level alignment and material stability in optimizing the efficiency of bifacial perovskite solar cells under both front and rear illumination.

As presented in Table 3, the selected device configurations achieved a high open-circuit voltage (Voc) of 1.45 V with a perovskite bandgap of 1.6 eV, corresponding to a remarkably low voltage deficit of 0.15 V. This improvement is primarily attributed to the incorporation of the 2D-PVK $(PEA)_2Pb_2I_4$ interlayer, which effectively suppresses non-radiative recombination and enhances interfacial charge extraction. The significant reduction in energy losses highlights the

effectiveness of interfacial engineering in minimizing recombination pathways, thereby demonstrating the potential of 2D/3D perovskite architectures in achieving high-efficiency photovoltaic devices.

Furthermore, the short-circuit current density (Jsc) remained nearly constant across all optimized configurations (≈ 22.2 mA/cm²), confirming efficient light absorption and charge-carrier generation. Similarly, the highest fill factor (FF) values, reaching up to 85%, indicate efficient charge transport and minimal recombination losses, further validating the robustness of the proposed device architecture.

IV.2.1 Energy Band Alignment and Its Influence on Device Performance

A clear understanding of energy-level alignment is essential for interpreting how bifacial perovskite solar cells achieve their highest or lowest power conversion efficiencies PCEs. The band diagrams presented in Figure IV.3 illustrate the interfacial energy alignment for devices where ZnOS, Nb_2O_5, and $BaSnO_3$ serve as ETLs in contact with the 3D-perovskite absorber $Cs_x(FA_{0.4}MA_{0.6})_{1-x}PbI_{2.8}Br_{0.2}$. At the ETL/PVK interfaces, conduction band offsets (CBOs) of -0.39 eV, -0.07 eV, and -0.10 eV were observed, alongside valence band offsets (VBOs) of 1.09 eV, 1.80 eV, and 1.09 eV, respectively. Although the presence of a small spike in the conduction band introduces a minor barrier for electron transport, it remains sufficiently low to allow efficient charge extraction, thereby suppressing non-radiative recombination losses. While VBOs at the ETL/PVK interfaces can also affect performance, they are generally less critical than CBOs in determining ETL functionality.

In contrast, when Me-4PACz and $CuAlO_2$ are employed as HTLs in contact with the 2D-PVK $(PEA)_2Pb_2I_4$, they exhibit cliff-like VBOs of 0.41 eV and 0.56 eV, respectively. This favorable alignment facilitates efficient hole transfer from the 2D-perovskite layer into the HTLs. The relatively larger VBO in $CuAlO_2$ provides an additional barrier against hole leakage, thereby improving hole extraction efficiency. Conversely, the Me-4PACz-based HTL device, which exhibits a smaller VBO, shows slightly reduced performance under rear illumination, leading to a marginally lower Bf compared to the other configurations see Table IV.3.

Overall, these interfacial band alignments confirm that the n-i-p device configuration effectively promotes charge separation, minimizes recombination pathways, and enhances device efficiency, thus establishing it as the most suitable architecture for high-performance bifacial perovskite solar cells.

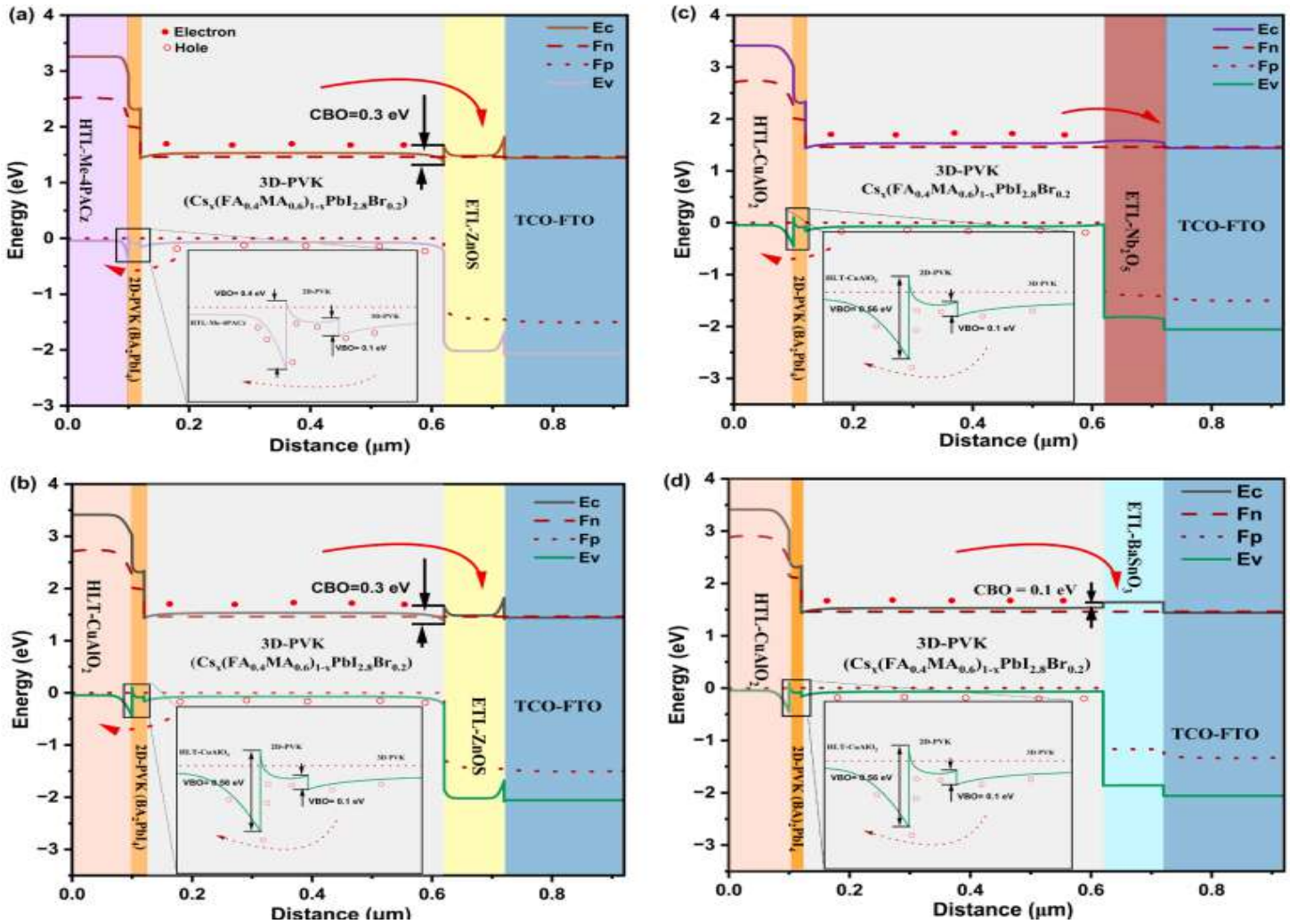


Figure IV.3 Energy band diagram of a best device incorporating Multiple Materials: FTO, ETLs, 3D-PVK-$Cs_x(FA_{0.4}MA_{0.6})_{1-X}PbI_{2.8}Br_{0.2}$, 2D-PVK- $(PEA)_2Pb_2I_4$, and HTLs.

IV.2.2 Spectral Response Analysis through Quantum Efficiency (QE) Curves

In Figure IV.4, the quantum efficiency (QE) as a function of wavelength provides critical insights into the optoelectronic behavior of the bifacial perovskite solar cells under different HTL (Me-4PACz and $CuAlO_2$) and ETL (ZnOS, Nb_2O_5, $BaSnO_3$) configurations and illumination conditions. QE represents the percentage of incident photons effectively converted into current in the device. Ideally, this corresponds to complete light absorption in the active layer without reflection or parasitic losses.[176]

The slightly lower QE observed under front illumination in the 300-400 nm range is attributed to ultraviolet absorption by the FTO or ETL layers, whereas back illumination exhibits enhanced response in this region, suggesting high transparency of the HTL and the 2D-

perovskite layer. Between 360 nm and 700 nm, the QE remains close to 100%, reflecting nearly optimal light harvesting by the 3D-perovskite absorber and efficient charge extraction, further promoted by the interfacial role of the 2D-perovskite.

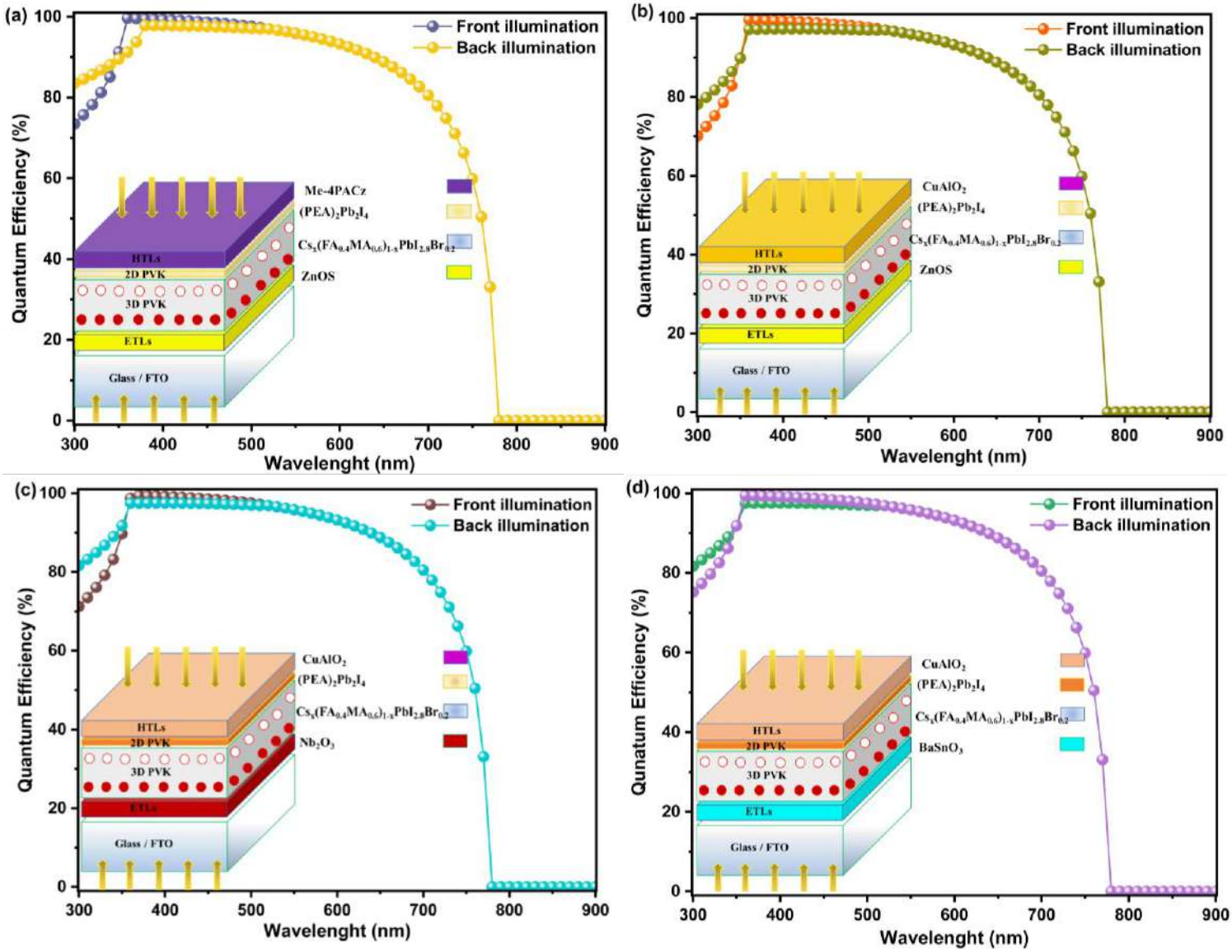


Figure IV.4 Quantum efficiency of a best device incorporating Multiple Materials: FTO, ETLs, 3D-PVK-$Cs_x(FA_{0.4}MA_{0.6})_{1-X}PbI_{2.8}Br_{0.2}$, 2D-PVK- $(PEA)_2Pb_2I_4$, and HTLs, the insets present the structure of each configurations as mentioned in Table IV.1.

Beyond 700 nm, a gradual QE decrease is observed as the photon energy approaches the bandgap of the absorber layer $Cs_x(FA_{0.4}MA_{0.6})_{1-X}PbI_{2.8}Br_{0.2}$ (~1.6 eV, corresponding to ~775 nm). The sharp decline beyond 800 nm is expected, since photon energies become insufficient for absorption.[177] Importantly, the smooth decay near the band edge indicates the presence

of sub-bandgap states or defects that allow low-energy photon absorption but simultaneously increase non-radiative recombination, reducing efficiency.[178] In contrast, a sharper cutoff would denote higher material quality and fewer defect states.

Possible optimizations include adjusting the thickness of the 2D-perovskite layer or integrating a reflective back contact to enhance near-bandgap absorption. Despite these minor losses, the overall spectral response is highly stable and consistent across all devices, confirming the effectiveness of the selected material stack (ETL/3D-PVK/2D-PVK/HTL/TCO) in enabling robust and high-performance bifacial operation.

IV.2.3 Influence of Layer Thickness on Photovoltaic Performance

In this section, the influence of the thickness of all constituent layers on the photovoltaic performance of bifacial perovskite solar cells is systematically investigated. Optimizing the thickness of the ETL, HTL, absorber, and passivation layers is a critical factor in enhancing device efficiency, as it directly governs the balance between charge generation, transport, and recombination. Numerical simulations were performed using four different configurations, as illustrated in Figure 5, to determine the optimal thickness ranges.

The results indicate that the highest PCE values were obtained for relatively thin ETL and HTL layers (≈ 0.1 µm, Figure IV.5a-b) and an ultra-thin 2D-PVK interlayer (≈ 0.01 µm, Figure IV.5c). This improvement can be attributed to the reduction in charge carrier transport distances, which minimizes recombination losses and facilitates efficient charge extraction.[10] In contrast, the variation in ETL, HTL, and 2D-PVK thicknesses showed negligible effects on other photovoltaic parameters (V_{OC}, J_{SC}, and FF), with only minor deviations compared to the significant changes observed in PCE.

For the 3D-PVK absorber, however, a thicker layer was required to achieve enhanced J_{SC} and PCE (Figure IV.5d), owing to the increased light-harvesting capability of a thicker absorber. This trend was found to saturate at a thickness of ≈ 0.5 µm, beyond which further increases no longer improved PCE or J_{SC}.[179] At this stage, the absorber is already capable of absorbing most of the incident light, while additional thickness primarily introduces higher recombination rates and series resistance. Furthermore, a gradual decrease in V_{OC} and FF was observed with increasing absorber thickness, which can be attributed to recombination-dominated processes that outweigh the benefits of enhanced absorption.

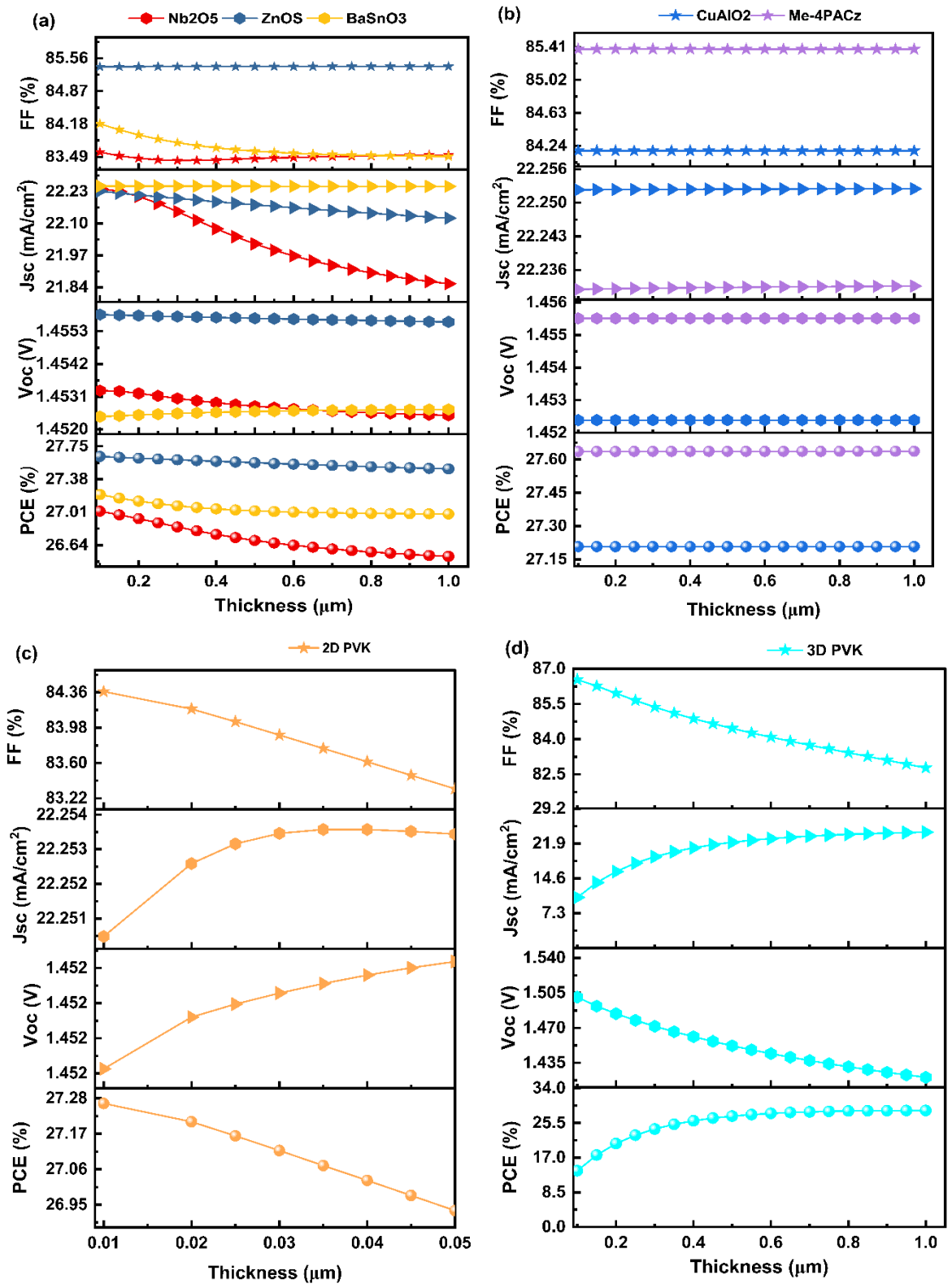


Figure IV.5 Analysis of Photovoltaic Parameters (PCE, V_{OC}, J_{SC}, and FF) in PSCB Solar Cells: The Impact of Thickness Variation in Electron Transport Layers (ETLs), 3D-Perovskite $Cs_x(FA_{0.4}MA_{0.6})_{1-x}PbI_{2.8}Br_{0.2}$, 2D-Perovskite $(PEA)_2Pb_2I$, and Hole Transport Layers (HTLs) on Solar Cell Efficiency.

IV.2.4 Influence of Total Defect Density (N_t) on Photovoltaic Performance

Total defect density (N_t) is a critical parameter that can significantly impact PV performance, as it directly influences charge carrier dynamics, recombination rates, and overall device efficiency.[180] As a result, high defect densities can severely degrade key performance parameters such as V_{OC}, J_{SC}, FF, PCE. Transport layers, such as ETLs and HTLs, generally exhibit a higher tolerance to defects since they primarily facilitate charge extraction rather than charge generation.[181] As shown in Figure IV.6a-b, variations in the defect density of ETLs, and HTLs, layers exhibit no noticeable impact on PV performance, as all photovoltaic parameters remain stable. Even with 2D-PVK see Figure IV.6c, there is no observed impact of N_t on PV performance.

This suggests that these layers can tolerate a range of defect densities without significantly affecting efficiency.[133] In contrast, defects in the perovskite absorber layer, particularly in the 3D-PVK layer, have a far more detrimental effect on device performance. The perovskite material is responsible for light absorption and charge carrier generation; therefore, an increase in its defect density can lead to substantial non-radiative losses, increased carrier recombination, and a sharp decline in photovoltaic parameters.[182] This is particularly critical for lead halide perovskites, where deep-level defects can trap carriers and drastically limit the achievable efficiency.

This effect is reflected in a strong negative correlation between the defect density of the 3D-PVK layer and PV performance, as depicted in Figure IV.6d. As N_t increases, PCE drops dramatically from 31% which is close to the reported theoretical efficiency limit of $MAPbI_3$-based PSCs (~31%) down to 0%.[183] This sharp decline can be attributed to high defect density impeding charge transport from the perovskite layer to the transport layers, leading to severe recombination losses. Similarly, other key PV parameters also deteriorate significantly. V_{OC} decreases from 1.47 V to 0.84 V, J_{SC} plummets from (22 mA/cm^2) to 0 (mA/cm^2), and FF drops from 84% to 21%. These results highlight the crucial role of minimizing defect density in the 3D-PVK layer to maintain high photovoltaic performance. After this analysis the optimal value of N_t for all layers it should be around $10E^{14}$ cm^{-2} leading to achieve higher PCE (around 28%).

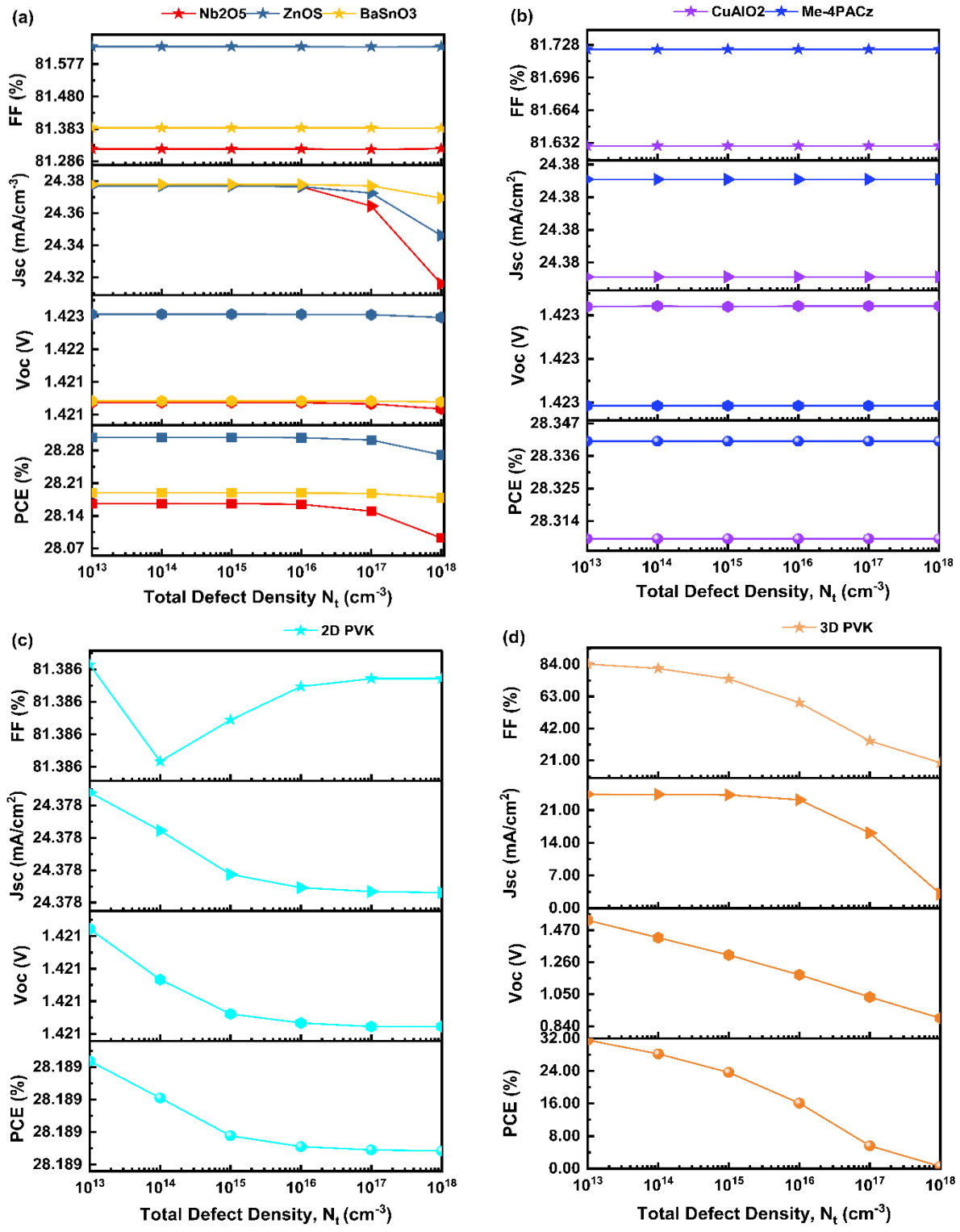


Figure IV.6 Analysis of Photovoltaic Parameters (PCE, V_{OC}, J_{SC}, and FF) in PSCB Solar Cells: The Impact of Total defect density N_t Variation in Electron Transport Layers ETLs, 3D-Perovskite $Cs_x(FA_{0.4}MA_{0.6})_{1-x}PbI_{2.8}Br_{0.2}$, 2D-Perovskite $(PEA)_2Pb_2I_4$, and Hole Transport Layers HTLs on Solar Cell Efficiency.

IV.2.5 Influence of Carrier Concentration of HTLs and ETLs on Photovoltaic Performance

The carrier concentration of hole transport layers HTLs and electron transport layers ETLs plays a pivotal role in defining the efficiency and overall performance of perovskite solar cells PSCs. These transport layers not only facilitate the selective extraction of charge carriers from the perovskite absorber toward the external circuit but also act as barriers against interfacial recombination. Hence, tuning their carrier concentrations is critical for optimizing device performance.

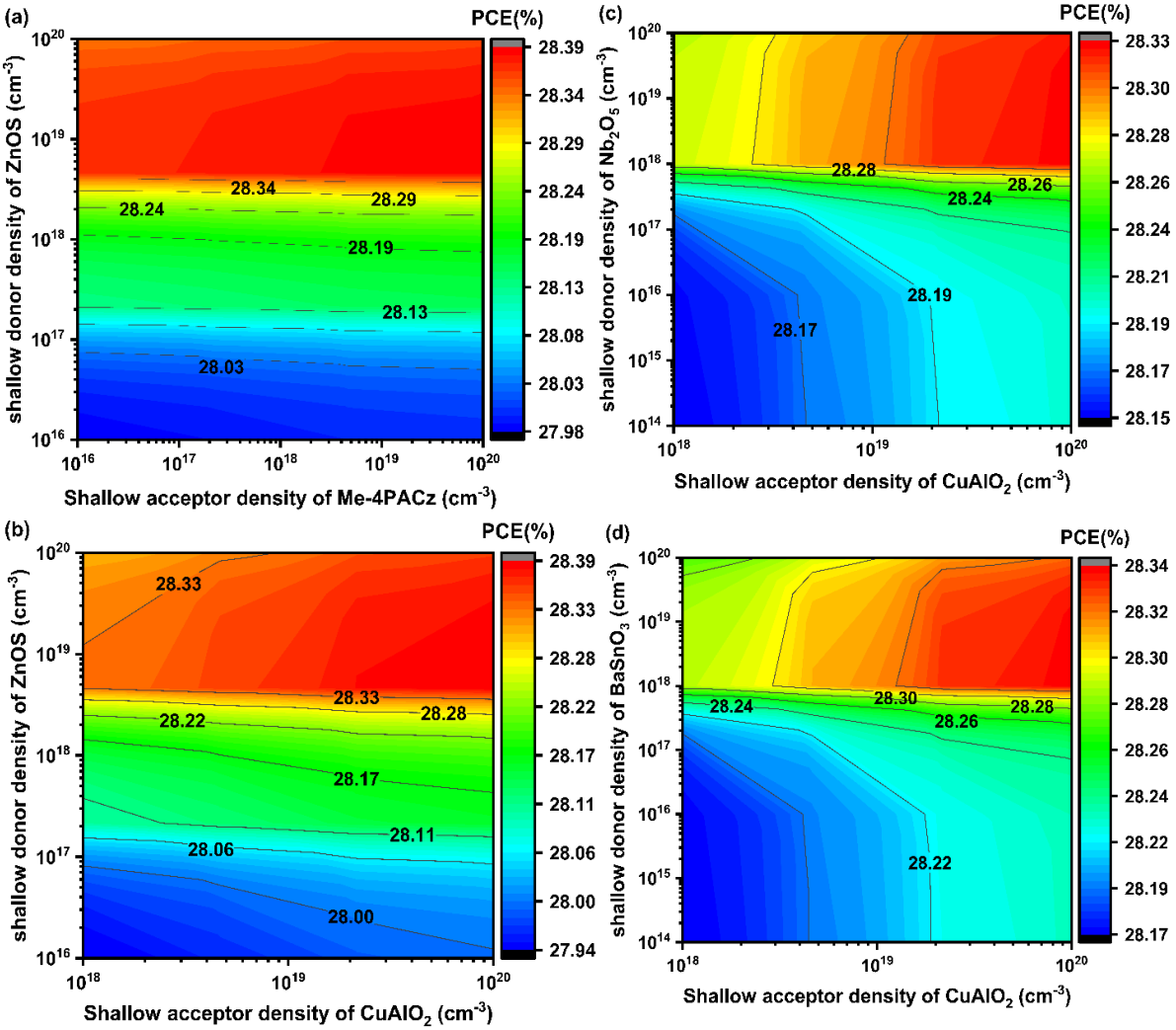


Figure IV.7 Contour Mapping of PCE (%) Performance as a Function of Shallow Donor Density (N_D) and Shallow Acceptor Density (N_A)Variations in Electron Transport Layers (ETLs) and Hole Transport Layers (HTLs).

As illustrated in Figure IV.7, the contour plots reveal a clear correlation between carrier concentration and the power conversion efficiency PCE of bifacial inverted PSCs. Specifically, shallow-to-moderate carrier densities in HTLs (Me-4PACz and $CuAlO_2$) and ETLs (ZnOS, Nb_2O_5, and $BaSnO_3$) significantly enhance efficiency, with values ranging between 28% and 28.4%. The highest efficiencies were observed in the upper-central region of the plots, where both HTL and ETL possess moderate-to-high carrier densities.

This improvement can be attributed to enhanced electrical conductivity: higher hole concentrations in HTLs accelerate hole extraction and reduce resistive losses, while increased electron concentrations in ETLs facilitate faster electron transport and suppress charge accumulation at the perovskite/ETL interface. Importantly, this balance minimizes recombination pathways and maintains steady-state charge flow.

In summary, achieving optimal carrier concentrations in both HTLs and ETLs is essential for ensuring balanced charge transport, effective carrier extraction, and improved operational stability of bifacial PSCs.

IV.2.6 Influence of Temperature on Photovoltaic Parameters

Temperature is one of the most critical environmental stressors influencing the stability and efficiency of perovskite solar cells PSCs. Continuous exposure to solar radiation elevates the device temperature, thereby altering its structural, physical, and electronic properties. A rise in temperature leads to a reduction in the bandgap energy,[184] which results in a linear decrease in the open-circuit voltage V_{OC} and an increase in non-radiative electron-hole recombination, both of which contribute to a significant reduction in the power conversion efficiency PCE.

Although additional thermal energy can generate more electron-hole pairs, this effect is counterbalanced by increased internal resistance and enhanced recombination, which undermine overall device performance.

Furthermore, the elevated kinetic energy of charge carriers increases the probability of recombination before reaching the depletion region, thereby reducing current collection efficiency. Simulation results, illustrated in Figure 8, show the effect of temperature variation between 300 K and 500 K on four different PSC configurations (I, II, III, IV; see Table IV.3). The fill factor FF decreases from 83.7% to 75.6%, while the VOC declines linearly from 1.431 V to 1.234 V. Similarly, the PCE drops sharply from 28.5% to 22.8%. In contrast, the short-circuit current density J_{SC} remains nearly constant with temperature, exhibiting only a negligible increase of 0.01 (mA/cm^2).

This stability of J_{SC} highlights that light absorption and photogeneration processes are not significantly impacted by temperature within the investigated range. However, the overall degradation of V_{OC}, FF, and consequently PCE, underscores that elevated temperatures primarily exacerbate non-radiative recombination and internal resistive losses. These findings confirm that thermal management strategies are essential for maintaining long-term stability and efficiency of PSCs under real-world operating conditions.

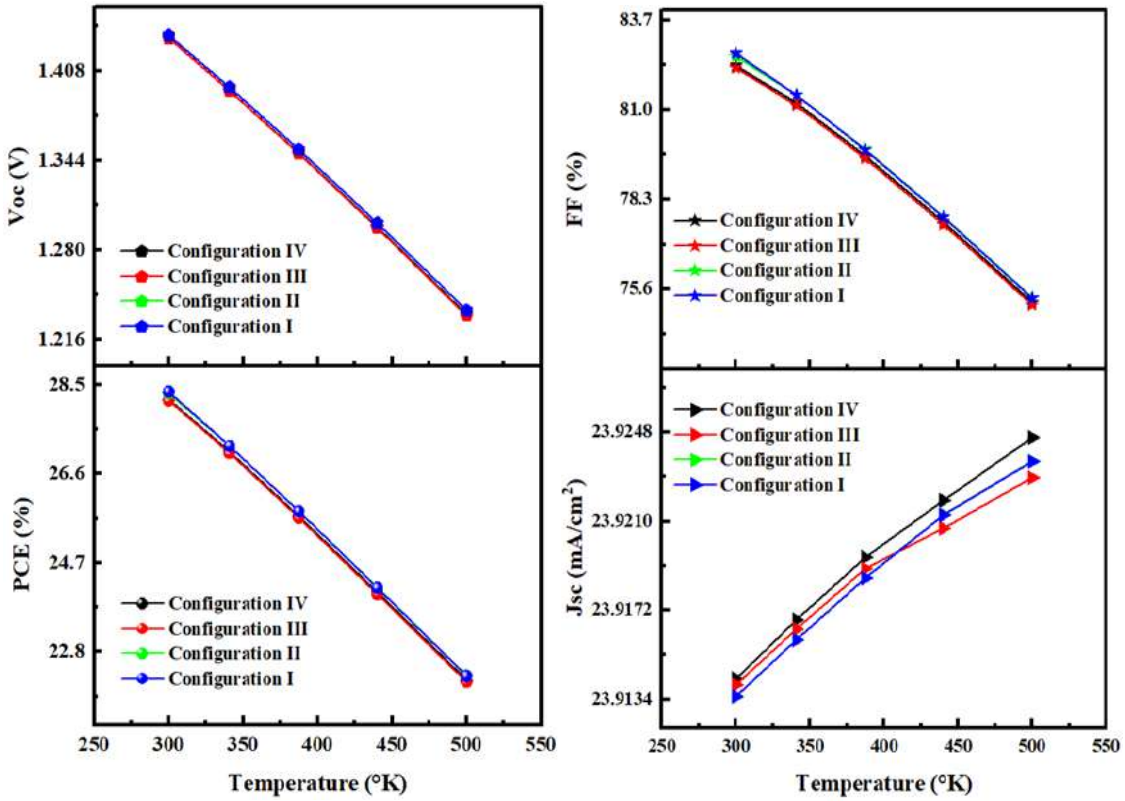


Figure IV.8 Analysis of Photovoltaic Parameters (PCE, V_{OC}, J_{SC}, and FF) in PSCB Solar Cells: The Impact of Temperature (°K) Variation in Electron Transport Layers (ETLs), 3D-Perovskite $Cs_x(FA_{0.4}MA_{0.6})_{1-x}PbI_{2.8}Br_{0.2}$, 2D-Perovskite $(PEA)_2Pb_2I_4$, and Hole Transport Layers (HTLs) on Solar Cell Efficiency**.**

IV.3 Final Optimized Devices

After completing the parametric investigations, the optimal values identified for layer thicknesses, total defect density (N_t), and doping concentrations (N_A for HTLs and N_D for ETLs) were implemented to maximize the photovoltaic performance of the bifacial perovskite solar cells. Before discussing the improvements achieved with these optimized parameters, it is important to first analyze the generation and recombination mechanisms within the different device configurations, as illustrated in Figure IV.9.

Across all four configurations, a similar behavior is observed, primarily because the ETLs and HTLs share comparable physical and electronic properties. As depicted in Figure IV.9, the photogeneration rate remains nearly uniform throughout the perovskite absorber layer, peaking at approximately ~9.5 × 10^{21} $cm^{-3}.s^{-1}$. This uniformity reflects efficient photon absorption and effective charge carrier generation within the bulk absorber. Sharp variations, however, are noted at the (ETL/perovskite) and (perovskite/HTL) interfaces, indicating strong optical absorption in these interfacial regions.[185]

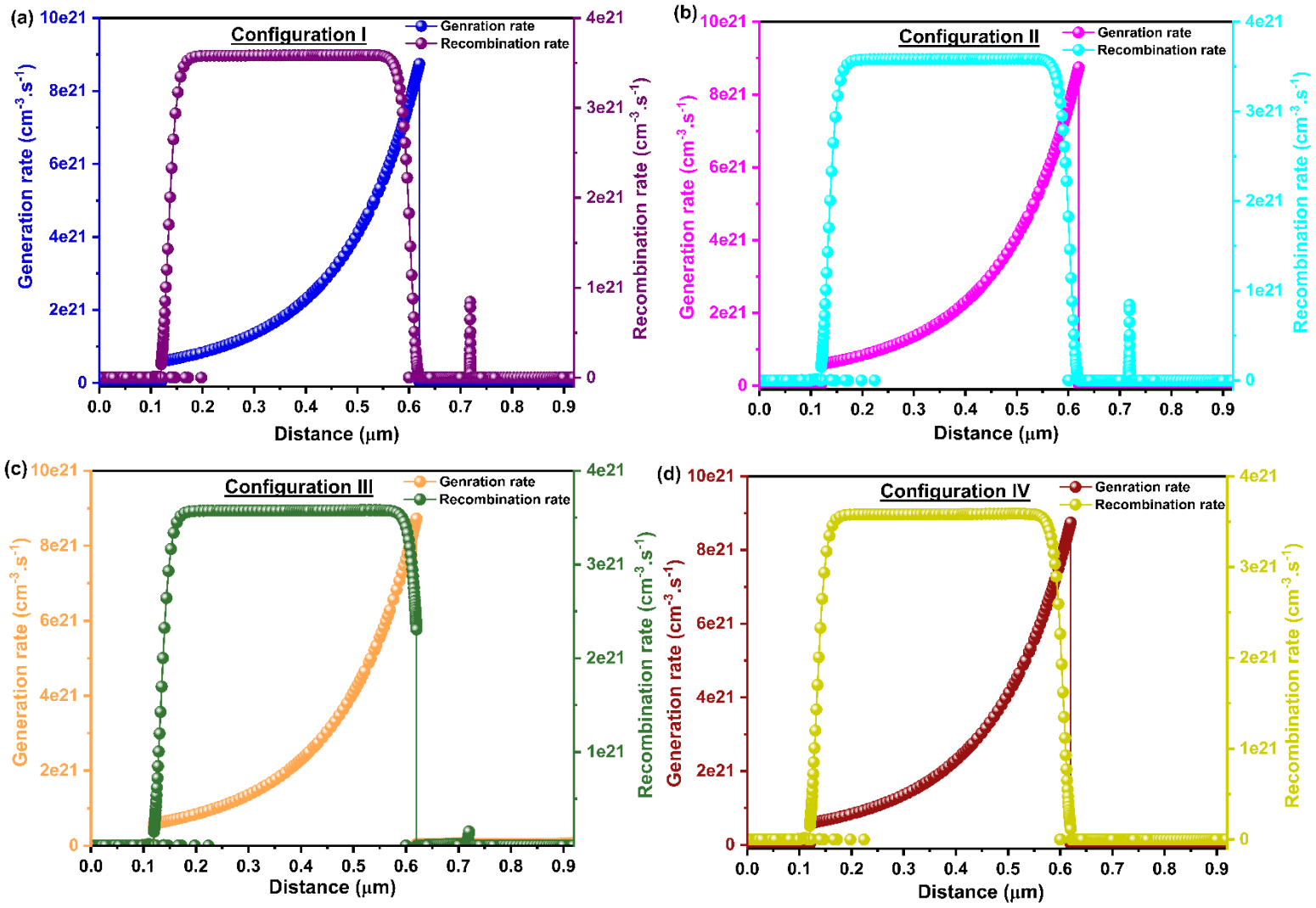


Figure IV.9 Curves Analyzing the Generation rate and Recombination rate of Photogenerated Carriers in Different Devices (I, II, III, IV).

On the other hand, the recombination rate is generally low within most of the active layer but rises significantly at the 3D-PVK/2D-PVK interface, reaching ~3.8 × 10^{21} $cm^{-3}.s^{-1}$. This pronounced peak suggests notable non-radiative recombination losses, which may arise from

interfacial defect states, energy level mismatches, or insufficiently optimized charge transfer pathways.[186] In contrast, the relatively low recombination observed at the ETL/perovskite and (perovskite/HTL) interfaces highlights efficient charge extraction and minimized carrier losses.

These findings emphasize the pivotal role of interfacial engineering in suppressing recombination, optimizing charge transfer, and ultimately achieving enhanced photovoltaic performance in the final optimized device structures.

IV.3.1 Influence of Absorber Density on Charge Carrier Diffusion Length and Lifetime

The diffusion length of charge carriers, defined as the average distance an excited electron or hole travels before recombination, is a fundamental parameter for assessing charge transport in semiconductors and photovoltaic materials. Figure IV.10a illustrates the variation of diffusion length with absorber density. At low densities, the limited number of charge carriers reduces recombination probability, resulting in longer diffusion lengths and more efficient charge transport.[187] As the density increases, carrier generation improves; however, the probability of recombination events also rises, gradually shortening the diffusion length. In highly dense absorber layers, excessive carrier-carrier interactions and defect-related processes dominate, leading to a sharp reduction in diffusion length.

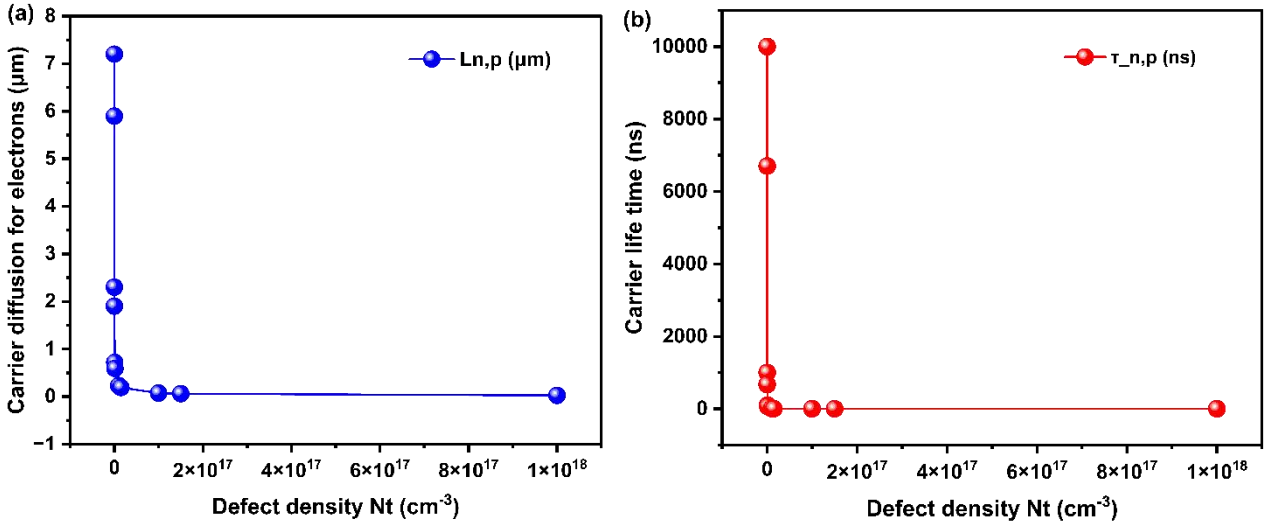


Figure IV.10 Carrier Diffusion Length (Ln, Ln) and Carrier Lifetime (T_n, T_p) as Functions of Defect Density (N_t) in the Optimal PSCB Solar Cell.

Similarly, Figure IV.10b shows the correlation between carrier lifetime and absorber density. At lower densities, reduced carrier interactions allow for longer lifetimes, reflecting suppressed recombination. As density increases, recombination events become more frequent, leading to shorter lifetimes. At very high densities, recombination dominates transport dynamics, drastically reducing carrier lifetime and thereby limiting overall photovoltaic performance.

IV.3.2 Electrical Impedance Analysis of Optimized Bifacial PSCs

The electrical impedance characteristics of bifacial inverted perovskite solar cells (PSCs) in the four studied configurations were analyzed using Nyquist plots to probe charge transport dynamics, interfacial recombination processes, and series and shunt resistances.[188] Nyquist plots provide critical insights into parameters such as charge transfer resistance (Rct), recombination resistance (Rrec), and capacitance (C), all of which directly influence carrier extraction efficiency and overall photovoltaic performance.

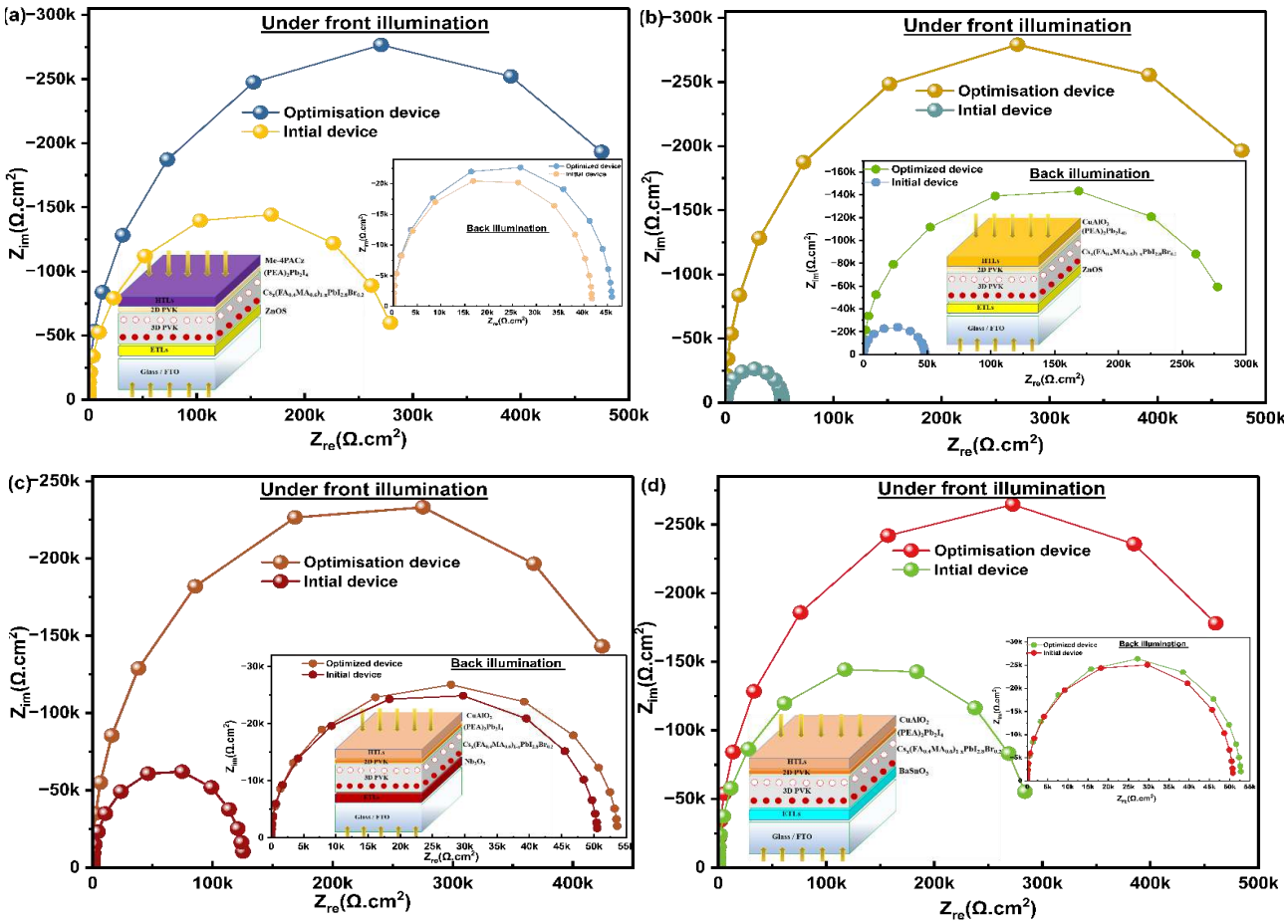


Figure IV.11 Nyquist impedance plot of PSCB with different types of an Optimized Device incorporating Multiple Materials: ETLs, 3D-PVK-$Cs_x(FA_{0.4}MA_{0.6})_{1-x}PbI_{2.8}Br_{0.2}$, 2D-PVK-$(PEA)_2Pb_2I_4$, and HTLs.

The relative contribution of Rrec and Rct is reflected in the diameter of the semicircle: a larger Rrec corresponds to lower recombination losses, thereby enhancing device efficiency.[189] Comparative analysis of the impedance spectra across the four configurations highlights the strong impact of interface quality and layer optimization on charge transport and recombination behavior.

As illustrated in Figure IV. 11, the optimized devices outperform their initial counterparts under both front and rear illumination, clearly demonstrating the effectiveness of the applied modifications. Despite slight variations in impedance responses, all devices exhibit a similar behavior characterized by a large semicircle, which reflects dominant charge transfer and recombination mechanisms. Notably, the enlarged semicircle signifies suppressed recombination losses and more efficient photovoltaic operation.

IV.3.3 Comparative Photovoltaic Performance of Initial and Optimized Bifacial Perovskite Solar Cell Configurations

In summary, our optimized devices exhibit superior PVK parameters compared to the initial ones, as presented in Figure IV.12, which shows a comparison of the J-V characteristics of the initial and optimized devices under front illumination, along with insets of the studied structures and a table summarizing all PVK parameters of the devices under both front and back scans for the initial and optimized states. All configurations after optimization exhibit enhanced photovoltaic performance.

Configuration (I) (FTO/ZnSO/3D-PVK/2D-PVK/Me-4PACz) under front illumination demonstrates an improvement in photovoltaic performance, with V_{OC} increasing from 1.462 V to 1.489 V, while J_{SC} remains stable at 22.22 (mA/cm²). Additionally, FF improves from 85.01% to 85.70%, leading to an enhancement in PCE from 27.64% to 28.36%. Similarly, under rear illumination, V_{OC} increases from 1.462 V to 1.489 V, J_{SC} remains stable at 22.13 (mA/cm²), FF improves from 85.22% to 85.72%, and PCE increases from 27.57% to 28.25%, confirming the beneficial impact of optimization on both illumination conditions see Figure IV.12a.

For Configuration (II) (i.e., FTO/ZnSO/3D-PVK/2D-PVK/$CuAlO_2$), the photovoltaic performance remains unchanged before and after optimization see Figure IV.12b. This stability could be attributed to intrinsic material constraints, already optimized interfaces, or persistent recombination pathways. Further improvements may therefore require advanced interface engineering, defect passivation, or the use of alternative HTL materials to enhance charge extraction and reduce losses.

Moreover, in Configuration (III) (i.e., FTO/Nb_2O_5/3D-PVK/2D-PVK/$CuAlO_2$), optimization leads to improved photovoltaic performance under front illumination, with V_{OC} increasing from 1.457 V to 1.487 V, FF improving from 83.36% to 85.60%, and PCE rising from 27.02% to 28.28%. Similarly, under rear illumination, V_{OC} increases from 1.457 V to 1.487 V, while J_{SC} remains stable at 22.15 (mA/cm²), FF improves from 83.61% to 85.65%, and PCE increases from 26.99% to 28.21%. These results clearly demonstrate the positive impact of optimization under both illumination conditions see Figure IV.12c.

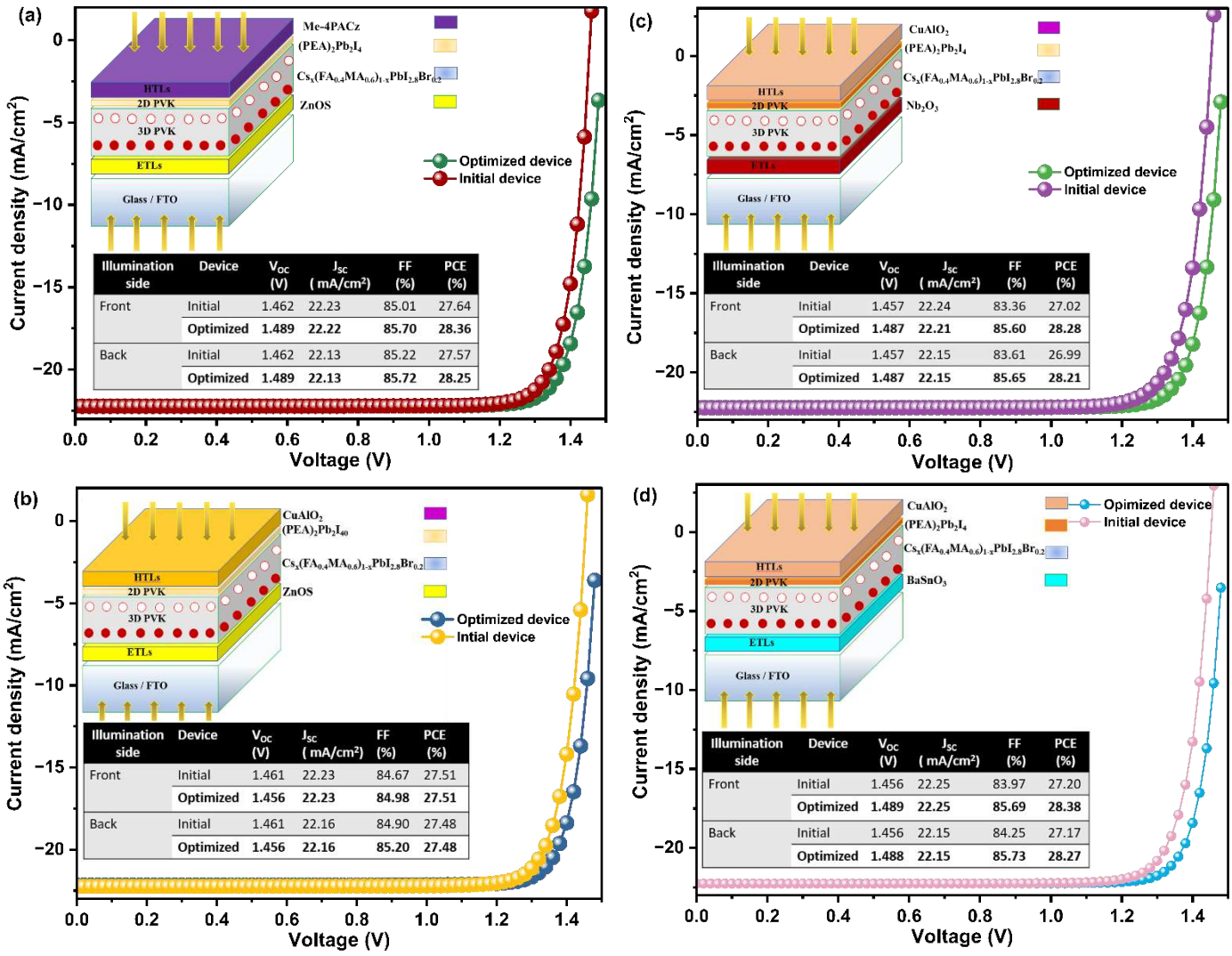


Figure IV.12 I-V Curves of an Optimized Device Incorporating Multiple Materials: FTO, ETLs, 3D-PVK-$Cs_x(FA_{0.4}MA_{0.6})_{1-X}PbI_{2.8}Br_{0.2}$, 2D-PVK- $(PEA)_2Pb_2I_4$, and HTLs.

Finally, Configuration (IV) (i.e., FTO/$BaSnO_3$/3D-PVK/2D-PVK/$CuAlO_2$) also exhibits enhanced photovoltaic performance under front illumination. V_{OC} rises from 1.459 V to 1.489

V, while J_{SC} remains consistent at 22.25 (mA/cm²). FF improves from 83.97% to 85.69%, resulting in a higher PCE of 28.38%, up from 27.20%. A similar trend is observed under rear illumination: V_{OC} increases from 1.456 V to 1.488 V, J_{SC} remains steady at 22.15 (mA/cm²), FF climbs from 84.25% to 85.73%, and PCE improves from 27.17% to 28.27%. These findings highlight the positive impact of optimization under both illumination conditions see Figure IV.12d.

Table IV.4 presents a comparative analysis of performance metrics across different configurations from prior studies on triple-cation bifacial perovskite solar cells. Notably, PCE achieved in this work surpasses previously reported values, highlighting the superior performance of the optimized absorber.

Table IV.4 Performance comparison of the final optimized device configuration (front and back illumination) against previously reported triple cation-devices.

Devices	Light illuminated side	V_{OC} (V)	J_{SC} (mA/cm²)	FF (%)	PCE (%)	References
Glass/FTO/MeO-2PACz/$Cs_{0.05}Rb_{0.05}MA_{0.05}FA_{0.85}Pb(I_{0.95}Br_{0.05})_3$/ LiF/C60/$SnO_2$/IZO	FTO	1.15	24.04	77.50	21.40	[190]
	IZO	1.14	22.08	22.80	20.01	
ITO/SnO_2/$Cs_{0.1}MA_{0.15}FA_{0.75}PbI_{2.49}Br_{0.51}$/Spiro-OMeTAD/$MoO_X$/Cu-seed/ Ag/$MoO_X$	ITO	1.08	19.72	0.63	13.44	[187]
	Ag/MoOx	1.10	13.8	0.68	10.25	
FTO/ZnSO/ $Cs_x(FA_{0.4}MA_{0.6})_{1-X}PbI_{2.8}Br_{0.2}$/2D-PVK/Me-4PACz	FTO	1.489	22.22	85.70	28.36	**This study**
	Me-4PACz	1.489	22.13	85.72	28.25	
FTO/ZnSO/ $Cs_x(FA_{0.4}MA_{0.6})_{1-X}PbI_{2.8}Br_{0.2}$/2D-PVK/$CuAlO_2$	FTO	1.456	22.23	84.98	27.51	**This study**
	$CuAlO_2$	1.456	22.16	85.20	27.48	
FTO/Nb_2O_5/ $Cs_x(FA_{0.4}MA_{0.6})_{1-X}PbI_{2.8}Br_{0.2}$/2D-PVK/$CuAlO_2$	FTO	1.487	22.21	85.60	28.28	**This study**
	$CuAlO_2$	1.487	22.15	85.65	28.21	
FTO/$BaSnO_3$/ $Cs_x(FA_{0.4}MA_{0.6})_{1-X}PbI_{2.8}Br_{0.2}$/2D-PVK/ $CuAlO_2$	**FTO**	**1.489**	**22.25**	**85.69**	**28.38**	**This study**
	$CuAlO_2$	**1.488**	**22.15**	**85.73**	**28.27**	

Conclusion

In this study, we analyzed the performance of bifacial perovskite inverter solar cells (PSCBs) using the SCAPS 1D simulation tool (version 3.1.1.12). The investigation focused on the effect of different Electron Transport Layers (ETLs) and Hole Transport Layers (HTLs), with FTO as

the front contact, 3D-PVK as the perovskite absorber, and 2D-PVK as an interfacial passivation layer to enhance Power Conversion Efficiency (PCE%) and device stability. The preliminary analysis identified four optimized configurations (I, II, III, IV), where the selected devices exhibited close PCE% values between the front and rear sides, with the highest efficiency recorded at 27.64% (front) and 27.57% (rear), indicating balanced performance and excellent optoelectronic stability. To further optimize the performance, we investigated the influence of the bandgap (E_g) on light absorption and spectral compatibility, as well as the effect of layer thickness variations (ETLs, HTLs, 2D-PVK, 3D-PVK). The results showed that tuning the thickness significantly improved charge extraction and overall efficiency. Additionally, we examined the impact of defect density (N_t), where reducing trap states led to lower recombination losses and enhanced stability. The study also explored carrier density (N_A - N_D) and the effect of temperature (T) on device performance. It was observed that increasing temperature caused a decline in open-circuit voltage (V_{OC}) due to enhanced recombination, emphasizing the importance of thermal stability. Moreover, the carrier diffusion length (L_n, L_p) and carrier lifetime (τ_n, τ_p) were analyzed, revealing that improved material quality and reduced defect states contributed to extended diffusion lengths, resulting in better charge extraction and efficiency. Through Nyquist analysis, it was observed that optimized devices exhibited lower internal resistance and weaker recombination, signifying improved charge transport and reduced energy losses.When comparing the obtained results with previous works, the optimized device architecture FTO/ZnSO/3D-PVK-$Cs_x(FA_{0.4}MA_{0.6})_{1-X}PbI_{2.8}Br_{0.2}$/2D-PVK/Me-4PACz achieved an outstanding PCE of 28.36%, positioning it among the most efficient perovskite solar cells reported. The key performance metrics showed a V_{OC} of 1.489 V, short-circuit current density (J_{SC}) of 22.22 (mA/cm²), and a fill factor (FF) of ~85.7%, reflecting enhanced charge extraction and minimized energy losses. Similarly, the FTO/Nb_2O_5/3D-PVK-$Cs_x(FA_{0.4}MA_{0.6})_{1-X}PbI_{2.8}Br_{0.2}$/2D-PVK/$CuAlO_2$ structure exhibited a PCE of 28.28% with V_{OC} of 1.487 V, while the FTO/$BaSnO_3$/3D-PVK-$Cs_x(FA_{0.4}MA_{0.6})_{1-X}PbI_{2.8}Br_{0.2}$/2D-PVK/$CuAlO_2$ achieved the highest efficiency of 28.38%, with an FF of 85.69%. These results highlight that selecting appropriate materials and reducing defect densities significantly contribute to the enhancement of photovoltaic performance, making these designs promising candidates for next-generation high-efficiency solar energy applications

General Conclusion

General Overview

This doctoral thesis focused on the numerical investigation and optimization of perovskite solar cells (PSCs) using the SCAPS-1D simulation platform. The principal objective of this work was to improve photovoltaic conversion efficiency, suppress non-radiative recombination losses, and enhance operational stability through advanced transport layer engineering, interface passivation strategies, and optimized device architectures. Particular attention was devoted to flexible and bifacial PSC technologies due to their strong potential for next-generation photovoltaic applications.

Main Contributions of Chapter II

Chapter II established the theoretical and methodological framework of the SCAPS-1D simulation environment employed throughout this thesis. The chapter presented the fundamental semiconductor equations governing photovoltaic device operation, including Poisson's equation, continuity equations, and drift–diffusion transport equations. In addition, the principal photovoltaic performance parameters and numerical modeling methodologies used for device optimization and performance evaluation were discussed in detail.

Main Results Obtained in Chapter III

Chapter III focused on the numerical investigation and optimization of flexible perovskite solar cells through the integration of novel hole transport layers (HTLs), electron transport layers (ETLs), CBz-PAI interfacial passivation layers, and MXene-based back contacts. Different material combinations were systematically investigated in order to analyze their influence on charge transport mechanisms, recombination dynamics, and photovoltaic performance. The obtained results demonstrated that transport layer engineering and interface optimization significantly improved carrier extraction efficiency and reduced interfacial recombination losses. The incorporation of CBz-PAI interlayers enhanced interface quality and reduced defect-assisted recombination mechanisms, while MXene-based back contacts improved electrical conductivity and energy-level alignment. The optimized flexible PSC achieved a

power conversion efficiency (PCE) of 27.17%, indicating a substantial improvement compared with the initial device configurations investigated in this work.

Confrontation of the Obtained Results with the Literature (Chapter III)

The optimized flexible PSC architecture developed in this thesis demonstrated highly competitive photovoltaic performance compared with several previously reported SCAPS-based flexible perovskite solar cells available in the literature. Previous numerical studies generally reported efficiencies ranging between 22% and 26%, depending on device architecture, transport materials, and interface quality. The superior performance obtained in this work can be attributed to the combined effect of optimized HTLs/ETLs, reduced interfacial defect density, improved energy-band alignment, and enhanced carrier transport dynamics.Furthermore, the incorporation of CBz-PAI interfacial layers and MXene-based contacts provided additional improvements in charge extraction efficiency and operational stability, confirming the effectiveness of advanced interface engineering strategies for high-efficiency flexible PSC applications.

Main Results Obtained in Chapter IV

Chapter IV was devoted to the numerical optimization of bifacial inverted perovskite solar cells incorporating hybrid 2D/3D perovskite absorbers. Detailed investigations were performed on the influence of absorber thickness, defect density, carrier concentration, operating temperature, generation–recombination mechanisms, and impedance characteristics. The obtained results confirmed that hybrid 2D/3D absorber engineering significantly improved carrier separation and reduced recombination losses within the active layer. In addition, impedance analysis demonstrated improved charge transport behavior and enhanced interfacial properties. The optimized bifacial PSC achieved front and rear power conversion efficiencies of 28.38% and 28.27%, respectively, confirming the excellent photovoltaic capability of the proposed bifacial architecture.

Confrontation of the Obtained Results with the Literature (Chapter IV)

Compared with previously published bifacial PSC configurations reported in the literature, the proposed architecture demonstrated highly competitive photovoltaic performance under both front-side and rear-side illumination conditions. Several reported bifacial PSC structures exhibited lower bifacial response and increased recombination losses due to interface instability and inefficient carrier transport mechanisms. The superior performance obtained in this work confirms the effectiveness of combining hybrid 2D/3D perovskite absorbers with optimized transport layers and interface engineering strategies. The reduced difference between front and rear efficiencies also demonstrates the high bifaciality and balanced charge transport characteristics of the proposed structure.

Scientific Contributions of the Thesis

This doctoral thesis provides important theoretical and numerical contributions toward the development of next-generation high-efficiency perovskite solar cells. The principal scientific contributions of this work can be summarized as follows:

- Development of optimized flexible PSC architectures incorporating novel HTLs and ETLs.
- Integration of CBz-PAI interfacial passivation layers for suppressing defect-assisted recombination and improving interface stability.
- Investigation of MXene-based back contacts as advanced conductive electrodes for enhanced carrier extraction.
- Numerical optimization of bifacial inverted PSCs incorporating hybrid 2D/3D absorbers.
- Comprehensive SCAPS-1D analyses of charge transport, recombination dynamics, impedance behavior, and thermal effects in advanced PSC architectures.

- Overall, the obtained results contribute to bridging the gap between numerical simulation and future experimental implementation of high-performance and stable PSC technologies.

- Future Perspectives.

Future research perspectives may include the experimental fabrication and validation of the proposed device architectures, investigation of lead-free perovskite absorber materials, large-scale module integration, and long-term environmental stability studies under realistic operating conditions. Additional studies may also focus on the application of artificial intelligence and machine learning techniques for predictive optimization and accelerated design of advanced photovoltaic materials and device structures.

References

References

[1] M. J. B. Kabeyi et O. A. Olanrewaju, « Sustainable Energy Transition for Renewable and Low Carbon Grid Electricity Generation and Supply », *Front. Energy Res.*, vol. 9, mars 2022, doi: 10.3389/fenrg.2021.743114.

[2] E. Kabir, P. Kumar, S. Kumar, A. A. Adelodun, et K.-H. Kim, « Solar energy: Potential and future prospects », *Renew. Sustain. Energy Rev.*, vol. 82, p. 894-900, févr. 2018, doi: 10.1016/j.rser.2017.09.094.

[3] T. D. Brown, K. A. Whitehead, et S. Mitragotri, « Materials for oral delivery of proteins and peptides », *Nat. Rev. Mater.*, vol. 5, nº 2, p. 127-148, févr. 2020, doi: 10.1038/s41578-019-0156-6.

[4] « An open-access database and analysis tool for perovskite solar cells based on the FAIR data principles | Nature Energy ». Consulté le: 20 mai 2026. [En ligne]. Disponible sur: https://www.nature.com/articles/s41560-021-00941-3?utm_source=chatgpt.com

[5] A. Polman, M. Knight, E. C. Garnett, B. Ehrler, et W. C. Sinke, « Photovoltaic materials: Present efficiencies and future challenges », *Science*, vol. 352, nº 6283, p. aad4424, avr. 2016, doi: 10.1126/science.aad4424.

[6] L. C. Palilis *et al.*, « Inorganic and Hybrid Interfacial Materials for Organic and Perovskite Solar Cells », *Adv. Energy Mater.*, vol. 10, nº 27, p. 2000910, 2020, doi: 10.1002/aenm.202000910.

[7] « Achievements, challenges, and future prospects for industrialization of perovskite solar cells | Light: Science & Applications ». Consulté le: 20 mai 2026. [En ligne]. Disponible sur: https://www.nature.com/articles/s41377-024-01461-x?utm_source=chatgpt.com

[8] « Suppressing non-radiative recombination for efficient and stable perovskite solar cells - Energy & Environmental Science (RSC Publishing) DOI:10.1039/D4EE02917H ». Consulté le: 20 mai 2026. [En ligne]. Disponible sur: https://pubs.rsc.org/en/content/articlehtml/2024/ee/d4ee02917h?utm_source=chatgpt.com

[9] « Optimizing Inorganic Cs4CuSb2Cl12/Cs2TiI6 Dual-Absorber Solar Cells: SCAPS-1D Simulations and Machine Learning ». Consulté le: 20 mai 2026. [En ligne]. Disponible sur: https://www.mdpi.com/2079-4991/15/16/1245?utm_source=chatgpt.com

[10] M. A. Benatallah, A. Elmohri, Y. I. Bouderbala, M. W. Alam, et S. Rabhi, « Boosting Efficiency in Flexible Perovskite Solar Cells with Novel HTLs and ETLs: A drift-diffusion numerical study of CBz-PAI Interlayers and MXene Back Contacts », *Adv. Theory Simul.*, vol. 8, nº 5, p. 2401161, 2025, doi: 10.1002/adts.202401161.

[11] S. Rabhi *et al.*, « Machine learning–enhanced SCAPS optimization of 28.38%-efficient bifacial triple-cation perovskite solar cells for building integration », *Surf. Interfaces*, vol. 91, p. 109216, juin 2026, doi: 10.1016/j.surfin.2026.109216.

[12] « IEA, Net Zero by 2050.pdf ». Consulté le: 30 août 2025. [En ligne]. Disponible sur: https://www.energy.gov/sites/default/files/2021-12/IEA,%20Net%20Zero%20by%202050.pdf

[13] « Net Zero by 2050 – Analysis », IEA. Consulté le: 30 août 2025. [En ligne]. Disponible sur: https://www.iea.org/reports/net-zero-by-2050

[14] « Energy Outlook | Energy economics | Home », bp global. Consulté le: 30 août 2025. [En ligne]. Disponible sur: https://www.bp.com/en/global/corporate/energy-economics/energy-outlook.html

[15] *Energy, Electricity and Nuclear Power Estimates for the Period up To 2050*, 1st ed. in Reference Data Series No Series, no. v. 1. Vienna: International Atomic Energy Agency, 2024.

[16] M. Fleck, H. Hirwa, et E. Wason, « On the Issues: Surging US Energy Demand, Cap-and-Trade Vote, and More », Resources for the Future. Consulté le: 30 août 2025. [En ligne]. Disponible sur: https://www.resources.org/on-the-issues/surging-us-energy-demand-cap-and-trade-vote-and-more/

[17] « Global industrial energy consumption 2050 », Statista. Consulté le: 30 août 2025. [En ligne]. Disponible sur: https://www.statista.com/statistics/263471/industrial-energy-consumption-worldwide/

[18] L. Myllyvirta, « Analysis: Record solar growth keeps China's CO2 falling in first half of 2025 », Carbon Brief. Consulté le: 30 août 2025. [En ligne]. Disponible sur: https://www.carbonbrief.org/analysis-record-solar-growth-keeps-chinas-co2-falling-in-first-half-of-2025/

[19] « EIA projects global energy consumption will outpace efficiency gains in most cases - U.S. Energy Information Administration (EIA) ». Consulté le: 30 août 2025. [En ligne]. Disponible sur: https://www.eia.gov/todayinenergy/detail.php?id=60642

[20] « World Energy Outlook 2019 – Analysis », IEA. Consulté le: 30 août 2025. [En ligne]. Disponible sur: https://www.iea.org/reports/world-energy-outlook-2019

[21] « EDGAR - The Emissions Database for Global Atmospheric Research ». Consulté le: 30 août 2025. [En ligne]. Disponible sur: https://edgar.jrc.ec.europa.eu/

[22] G. W. Crabtree et N. S. Lewis, « Solar energy conversion », *Phys. Today*, vol. 60, nº 3, p. 37-42, mars 2007, doi: 10.1063/1.2718755.

[23] « Sustainable Electricity Generation Through Solar Energy Technologies | SpringerLink ». Consulté le: 30 août 2025. [En ligne]. Disponible sur: https://link.springer.com/chapter/10.1007/978-981-97-9626-7_8

[24] T. S. Kishore, P. U. Kumar, et V. Ippili, « Review of global sustainable solar energy policies: Significance and impact », *Innov. Green Dev.*, vol. 4, nº 2, p. 100224, avr. 2025, doi: 10.1016/j.igd.2025.100224.

[25] T. Saga, « Advances in crystalline silicon solar cell technology for industrial mass production », *NPG Asia Mater.*, vol. 2, nº 3, p. 96-102, juill. 2010, doi: 10.1038/asiamat.2010.82.

[26] N. V. R. Naidu, G. M. Madhu, N. Kottam, et G. N. A. Kumar, Éd., *Advanced Materials in Engineering Applications: Proceedings of International Conference on Advanced Materials in Engineering Sciences*. London: CRC Press, 2024. doi: 10.1201/9781003545941.

[27] « Interactive Best Research-Cell Efficiency Chart | Photovoltaic Research | NLR ». Consulté le: 20 mai 2026. [En ligne]. Disponible sur: https://www.nlr.gov/pv/interactive-cell-efficiency

[28] « Photovoltaics Report - Fraunhofer ISE », Fraunhofer Institute for Solar Energy Systems ISE. Consulté le: 20 mai 2026. [En ligne]. Disponible sur: https://www.ise.fraunhofer.de/en/publications/studies/photovoltaics-report.html

[29] P. Mei, L. Wu, H. Zhang, et Z. Liu, « A Hybrid Multi-Objective Crisscross Optimization for Dynamic Economic/Emission Dispatch Considering Plug-In Electric Vehicles Penetration », *Energies*, vol. 12, nº 20, p. 3847, janv. 2019, doi: 10.3390/en12203847.

[30] A. J. Wiley, « LEWIS FRAAS LARRY PARTAIN ».

[31] « Third generation photovoltaics - Brown - 2009 - Laser & Photonics Reviews - Wiley Online Library ». Consulté le: 31 août 2025. [En ligne]. Disponible sur: https://onlinelibrary.wiley.com/doi/abs/10.1002/lpor.200810039

[32] « Handbook of Photovoltaic Science and Engineering | Wiley Online Books ». Consulté le: 31 août 2025. [En ligne]. Disponible sur: https://onlinelibrary.wiley.com/doi/book/10.1002/9780470974704

[33] « Anti-reflective coatings: A critical, in-depth review - Energy & Environmental Science (RSC Publishing) ». Consulté le: 31 août 2025. [En ligne]. Disponible sur: https://pubs.rsc.org/en/content/articlelanding/2011/ee/c1ee01297e

[34] H. Korichi, A. Boucheham, A. Bensdira, et M. Kezrane, « Optimization of the Back Metallization of Mono-crystalline Si Solar Cells Using Ag/Al Alloy Deposited by PVD », 2025, p. 37-42. doi: 10.1007/978-3-031-71926-4_6.

[35] « What is a thin film polycrystalline silicon solar cell? - Solar Panels and PV Battery ». Consulté le: 21 septembre 2025. [En ligne]. Disponible sur: https://laukiksolar.com/what-is-a-thin-film-polycrystalline-silicon-solar-cell/

[36] A. Maalouf, T. Okoroafor, Z. Jehl, V. Babu, et S. Resalati, « A comprehensive review on life cycle assessment of commercial and emerging thin-film solar cell systems », *Renew. Sustain. Energy Rev.*, vol. 186, p. 113652, oct. 2023, doi: 10.1016/j.rser.2023.113652.

[37] « A Review of Third Generation Solar Cells ». Consulté le: 19 juin 2025. [En ligne]. Disponible sur: https://www.mdpi.com/2227-9717/11/6/1852

[38] M. Giannouli, « Current Status of Emerging PV Technologies: A Comparative Study of Dye-Sensitized, Organic, and Perovskite Solar Cells », *Int. J. Photoenergy*, vol. 2021, nº 1, p. 6692858, 2021, doi: 10.1155/2021/6692858.

[39] P. Levermore, « Organic Solar Panels », Savvy Science. Consulté le: 21 septembre 2025. [En ligne]. Disponible sur: https://www.savvyscience.org/organic-solar-panels/

[40] C. the T.-O. B. L. Losses et device sturdiness E. Bellini, « Semitransparent dye-sensitized solar module for BIPV applications », pv magazine International. Consulté le: 21 septembre 2025. [En ligne]. Disponible sur: https://www.pv-magazine.com/2022/06/02/semitransparent-dye-sensitized-solar-module-for-bipv-applications/

[41] C. Bell, A. Olukemi, et A. Gracias, *Advanced Perovskite-Silicon Tandem Solar Cells: Enhancing Efficiency and Stability*. 2024. doi: 10.20944/preprints202408.0002.v1.

[42] X. Liang *et al.*, « Flexible Perovskite Solar Cells: Progress and Prospects », *Front. Mater.*, vol. 8, p. 634353, mars 2021, doi: 10.3389/fmats.2021.634353.

[43] J. S. Manser, J. A. Christians, et P. V. Kamat, « Intriguing Optoelectronic Properties of Metal Halide Perovskites », *Chem. Rev.*, vol. 116, nº 21, p. 12956-13008, nov. 2016, doi: 10.1021/acs.chemrev.6b00136.

[44] « Die Gesetze der Krystallochemie | The Science of Nature ». Consulté le: 31 août 2025. [En ligne]. Disponible sur: https://link.springer.com/article/10.1007/BF01507527

[45] « Crystal Structure of Barium Titanate », *Nature*, vol. 155, p. 484-485, avr. 1945, doi: 10.1038/155484b0.

[46] A. Kojima, K. Teshima, Y. Shirai, et T. Miyasaka, « Organometal Halide Perovskites as Visible-Light Sensitizers for Photovoltaic Cells », *J. Am. Chem. Soc.*, vol. 131, nº 17, p. 6050-6051, mai 2009, doi: 10.1021/ja809598r.

[47] « (PDF) Organic–inorganic metal halide hybrids beyond perovskites ». Consulté le: 31 août 2025. [En ligne]. Disponible sur: https://www.researchgate.net/publication/326583688_Organic-inorganic_metal_halide_hybrids_beyond_perovskites

[48] J. W. Turnley, S. Agarwal, et R. Agrawal, « Rethinking tolerance factor analysis for chalcogenide perovskites », *Mater. Horiz.*, vol. 11, nº 19, p. 4802-4808, sept. 2024, doi: 10.1039/D4MH00689E.

[49] « Lead Iodide Perovskite Sensitized All-Solid-State Submicron Thin Film Mesoscopic Solar Cell with Efficiency Exceeding 9% | Scientific Reports ». Consulté le: 31 août 2025. [En ligne]. Disponible sur: https://www.nature.com/articles/srep00591?utm_source=chatgpt.com

[50] « Best Research-Cell Efficiency Chart | Photovoltaic Research | NREL ». Consulté le: 31 août 2025. [En ligne]. Disponible sur: https://www.nrel.gov/pv/cell-efficiency?utm_source=chatgpt.com

[51] « Efficient planar heterojunction perovskite solar cells by vapour deposition | Nature ». Consulté le: 31 août 2025. [En ligne]. Disponible sur: https://www.nature.com/articles/nature12509

[52] « High-performance photovoltaic perovskite layers fabricated through intramolecular exchange | Science ». Consulté le: 31 août 2025. [En ligne]. Disponible sur: https://www.science.org/doi/10.1126/science.aaa9272

[53] « A fluorene-terminated hole-transporting material for highly efficient and stable perovskite solar cells | Nature Energy ». Consulté le: 31 août 2025. [En ligne]. Disponible sur: https://www.nature.com/articles/s41560-018-0200-6

[54] C. Zhong *et al.*, « Decoupling electrolytes towards stable and high-energy rechargeable aqueous zinc–manganese dioxide batteries », *Nat. Energy*, vol. 5, nº 6, p. 440-449, juin 2020, doi: 10.1038/s41560-020-0584-y.

[55] H. Yu *et al.*, « Reversible adsorption with oriented arrangement of a zwitterionic additive stabilizes electrodes for ultralong-life Zn-ion batteries », *Energy Environ. Sci.*, vol. 16, nº 6, p. 2684-2695, juin 2023, doi: 10.1039/D3EE00982C.

[56] Y. Chen *et al.*, « Stabilizing Efficient Perovskite/Silicon Tandem Solar Cells With Amorphous and Asymmetric Hole-Selective Contacts », *Adv. Mater.*, vol. 38, nº 28, p. e73106, 2026, doi: 10.1002/adma.73106.

[57] « Incorporation of rubidium cations into perovskite solar cells improves photovoltaic performance | Science ». Consulté le: 31 août 2025. [En ligne]. Disponible sur: https://www.science.org/doi/10.1126/science.aah5557

[58] M. Büchs, N. Cass, C. Mullen, K. Lucas, et D. Ivanova, « Emissions savings from equitable energy demand reduction », *Nat. Energy*, vol. 8, nº 7, p. 758-769, juill. 2023, doi: 10.1038/s41560-023-01283-y.

[59] A. K. Jena, A. Kulkarni, et T. Miyasaka, « Halide Perovskite Photovoltaics: Background, Status, and Future Prospects », *Chem. Rev.*, vol. 119, nº 5, p. 3036-3103, mars 2019, doi: 10.1021/acs.chemrev.8b00539.

[60] J.-P. Correa-Baena *et al.*, « Promises and challenges of perovskite solar cells », *Science*, vol. 358, nº 6364, p. 739-744, nov. 2017, doi: 10.1126/science.aam6323.

[61] « (PDF) Optical characterization of ZnO thin films prepared by Chemical bath deposition method ». Consulté le: 31 août 2025. [En ligne]. Disponible sur:

https://www.researchgate.net/publication/326375024_Optical_characterization_of_ZnO_thin_films_prepared_by_Chemical_bath_deposition_method

[62] L. Du Plessis et C.-R. Loth, « Transforming the Linguistic Landscape of South Africa - More of the Same? Chapter 22 of Handbook of Linguistic Landscapes and Multilingualism Editors: Durk Gorter and Jasone Cenoz 2025, Wiley (New York) », 2025, p. 355-374. doi: 10.1002/9781394231805.ch22.

[63] « Transition of Perovskite Solar Technologies to Being Flexible - Castriotta - 2025 - Advanced Materials - Wiley Online Library ». Consulté le: 31 août 2025. [En ligne]. Disponible sur: https://advanced.onlinelibrary.wiley.com/doi/abs/10.1002/adma.202408036

[64] « La-Doped BaSnO 3 Electron Transport Layer for Perovskite Solar Cells | Request PDF ». Consulté le: 31 août 2025. [En ligne]. Disponible sur: https://www.researchgate.net/publication/328486180_La-Doped_BaSnO_3_Electron_Transport_Layer_for_Perovskite_Solar_Cells

[65] N.-G. Park, « Perovskite solar cells: an emerging photovoltaic technology », *Mater. Today*, vol. 18, nº 2, p. 65-72, mars 2015, doi: 10.1016/j.mattod.2014.07.007.

[66] J.-P. Correa-Baena *et al.*, « The rapid evolution of highly efficient perovskite solar cells », *Energy Environ. Sci.*, vol. 10, nº 3, p. 710-727, 2017, doi: 10.1039/C6EE03397K.

[67] « Stimuli-Responsive Materials: From Molecules to Nature Mimicking Materials Design Marek W. Urban », *MRS Bull.*, vol. 42, nº 10, p. 766-766, oct. 2017, doi: 10.1557/mrs.2017.229.

[68] Z. Liu, H. Li, H. Wang, D. Shen, X. Wang, et P. F. A. Alkemade, « Favored Structure of Ag Nanoparticles Embedded in SiO2 by Implantation: Single Crystal with Contracted (111) Lattice », *J. Mater. Res.*, vol. 15, nº 6, p. 1245-1247, juin 2000, doi: 10.1557/JMR.2000.0179.

[69] « Effect of different device parameters on tin-based perovskite solar cell coupled with In2S3 electron transport layer and CuSCN and Spiro-OMeTAD alternative hole transport layers for high-efficiency performance: Energy Sources, Part A: Recovery, Utilization, and Environmental Effects: Vol 46, No 1 ». Consulté le: 31 août 2025. [En ligne]. Disponible sur: https://www.tandfonline.com/doi/abs/10.1080/15567036.2020.1820628

[70] « Inorganic perovskite photocatalysts for solar energy utilization - Chemical Society Reviews (RSC Publishing) ». Consulté le: 31 août 2025. [En ligne]. Disponible sur: https://pubs.rsc.org/en/content/articlelanding/2022/ap/c5cs00769k/unauth

[71] L. Hu, R. H. Wei, X. W. Tang, W. J. Lu, X. B. Zhu, et Y. P. Sun, « Design strategy for p-type transparent conducting oxides », *J. Appl. Phys.*, vol. 128, nº 14, p. 140902, oct. 2020, doi: 10.1063/5.0023656.

[72] « SnO2: A Wonderful Electron Transport Layer for Perovskite Solar Cells - Jiang - 2018 - Small - Wiley Online Library ». Consulté le: 2 septembre 2025. [En ligne]. Disponible sur: https://onlinelibrary.wiley.com/doi/abs/10.1002/smll.201801154

[73] S. Huang, P. Li, J. Wang, J. C.-C. Huang, Q. Xue, et N. Fu, « Modification of SnO2 electron transport Layer: Brilliant strategies to make perovskite solar cells stronger », *Chem. Eng. J.*, vol. 439, p. 135687, juill. 2022, doi: 10.1016/j.cej.2022.135687.

[74] M. F. M. Noh *et al.*, « The architecture of the electron transport layer for a perovskite solar cell », *J. Mater. Chem. C*, vol. 6, nº 4, p. 682-712, janv. 2018, doi: 10.1039/C7TC04649A.

[75] H. Shao, N. H. Ladi, H. Pan, X. L. Zhang, Y. Shen, et M. Wang, « 2D Materials as Electron Transport Layer for Low-Temperature Solution-Processed Perovskite Solar Cells », *Sol. RRL*, vol. 5, nº 3, p. 2000566, 2021, doi: 10.1002/solr.202000566.

[76] J. Tan, H. Li, Y. Sun, G. Li, Y. Zhao, et H. Yu, « A ZnO&GeSe composite electron transport layer for organic solar cells », *J. Mater. Chem. A*, vol. 12, nº 3, p. 1530-1542, janv. 2024, doi: 10.1039/D3TA05900F.

[77] Z. Xu *et al.*, « La-doped SnO2 as ETL for efficient planar-structure hybrid perovskite solar cells », *Org. Electron.*, vol. 73, p. 62-68, oct. 2019, doi: 10.1016/j.orgel.2019.03.053.

[78] « Understanding Detrimental and Beneficial Grain Boundary Effects in Halide Perovskites | Request PDF ». Consulté le: 2 septembre 2025. [En ligne]. Disponible sur: https://www.researchgate.net/publication/328573219_Understanding_Detrimental_and_Beneficial_Grain_Boundary_Effects_in_Halide_Perovskites

[79] « Solvent engineering for high-performance inorganic–organic hybrid perovskite solar cells | Nature Materials ». Consulté le: 2 septembre 2025. [En ligne]. Disponible sur: https://www.nature.com/articles/nmat4014

[80] Y. Li *et al.*, « Grain boundary passivation as an optimal strategy for perovskite solar cells with improved stability », *Sustain. Energy Fuels*, vol. 9, nº 11, p. 3078-3087, mai 2025, doi: 10.1039/D5SE00426H.

[81] L. Fu, H. Li, L. Wang, R. Yin, B. Li, et L. Yin, « Defect passivation strategies in perovskites for an enhanced photovoltaic performance », *Energy Environ. Sci.*, vol. 13, nº 11, p. 4017-4056, nov. 2020, doi: 10.1039/D0EE01767A.

[82] B. Chen *et al.*, « Grain Engineering for Perovskite/Silicon Monolithic Tandem Solar Cells with Efficiency of 25.4% », *Joule*, vol. 3, nº 1, p. 177-190, janv. 2019, doi: 10.1016/j.joule.2018.10.003.

[83] J. T. Matondo, H. Hu, Y. Ding, M. Mateen, G. Cheng, et J. Ding, « Slot-Die Coating for Scalable Fabrication of Perovskite Solar Cells and Modules », *Adv. Mater. Technol.*, vol. 9, nº 10, p. 2302082, 2024, doi: 10.1002/admt.202302082.

[84] « Hole transport layers for organic solar cells: recent progress and prospects - Journal of Materials Chemistry A (RSC Publishing) ». Consulté le: 2 septembre 2025. [En ligne]. Disponible sur: https://pubs.rsc.org/en/content/articlelanding/2020/ta/d0ta03511d

[85] Y. Yao, C. Cheng, C. Zhang, H. Hu, K. Wang, et S. De Wolf, « Organic Hole-Transport Layers for Efficient, Stable, and Scalable Inverted Perovskite Solar Cells », *Adv. Mater.*, vol. 34, nº 44, p. 2203794, 2022, doi: 10.1002/adma.202203794.

[86] « A Review of Inorganic Hole Transport Materials for Perovskite Solar Cells - Kung - 2018 - Advanced Materials Interfaces - Wiley Online Library ». Consulté le: 2 septembre 2025. [En ligne]. Disponible sur: https://advanced.onlinelibrary.wiley.com/doi/abs/10.1002/admi.201800882

[87] « (PDF) Charge-transport layer engineering in perovskite solar cells ». Consulté le: 2 septembre 2025. [En ligne]. Disponible sur: https://www.researchgate.net/publication/340691948_Charge-transport_layer_engineering_in_perovskite_solar_cells

[88] M. Li *et al.*, « Graphene quantum dots as the hole transport layer material for high-performance organic solar cells », *Phys. Chem. Chem. Phys.*, vol. 15, nº 43, p. 18973-18978, oct. 2013, doi: 10.1039/C3CP53283F.

[89] W. Xiang, S. (Frank) Liu, et W. Tress, « A review on the stability of inorganic metal halide perovskites: challenges and opportunities for stable solar cells », *Energy Environ. Sci.*, vol. 14, nº 4, p. 2090-2113, avr. 2021, doi: 10.1039/D1EE00157D.

[90] T. Leijtens, G. E. Eperon, N. K. Noel, S. N. Habisreutinger, A. Petrozza, et H. J. Snaith, « Stability of Metal Halide Perovskite Solar Cells », *Adv. Energy Mater.*, vol. 5, nº 20, p. 1500963, 2015, doi: 10.1002/aenm.201500963.

[91] J. Tao *et al.*, « Precisely adjusting the organic/electrode interface charge barrier for efficient and stable Ag-based regular perovskite solar cells with >23% efficiency », *Chem. Eng. J.*, vol. 463, p. 142445, mai 2023, doi: 10.1016/j.cej.2023.142445.

[92] B. Lyu, L. Yang, Y. Luo, X. Zhang, et J. Zhang, « Counter electrodes for perovskite solar cells: materials, interfaces and device stability », *J. Mater. Chem. C*, vol. 10, nº 30, p. 10775-10798, août 2022, doi: 10.1039/D2TC02182J.

[93] A. Zeinidenov, T. Mukametkali, B. Ilyassov, A. Aimukhanov, et D. Valiev, « The effect of MoO3 interlayer on electro-physical characteristics of the perovskite solar cells », *Synth. Met.*, vol. 281, p. 116903, nov. 2021, doi: 10.1016/j.synthmet.2021.116903.

[94] J. Zhou *et al.*, « Ultra-low-cost all-air processed carbon-based perovskite solar cells from bottom electrode to counter electrode », *J. Power Sources*, vol. 478, p. 228764, déc. 2020, doi: 10.1016/j.jpowsour.2020.228764.

[95] D. Zheng, F. Raffin, P. Volovitch, et T. Pauporté, « Control of perovskite film crystallization and growth direction to target homogeneous monolithic structures », *Nat. Commun.*, vol. 13, nº 1, p. 6655, nov. 2022, doi: 10.1038/s41467-022-34332-3.

[96] S. Zhou, « Rapid separation and purification of lead halide perovskite quantum dots through differential centrifugation in nonpolar solvent », *RSC Adv.*, vol. 11, nº 45, p. 28410-28419, 2021, doi: 10.1039/D1RA04578D.

[97] « Compact nanostructured TiO 2 deposited by aerosol spray pyrolysis for the hole-blocking layer in a CH 3 NH 3 PbI 3 perovskite solar cell | Request PDF ». Consulté le: 3 septembre 2025. [En ligne]. Disponible sur: https://www.researchgate.net/publication/305699549_Compact_nanostructured_TiO_2_deposited_by_aerosol_spray_pyrolysis_for_the_hole-blocking_layer_in_a_CH_3_NH_3_PbI_3_perovskite_solar_cell

[98] S. Razza *et al.*, « Perovskite solar cells and large area modules (100 cm2) based on an air flow-assisted PbI2 blade coating deposition process », *J. Power Sources*, vol. 277, p. 286-291, mars 2015, doi: 10.1016/j.jpowsour.2014.12.008.

[99] G. O. Prado, L. G. M. Vieira, et J. J. R. Damasceno, « Solar dish concentrator for desalting water », *Sol. Energy*, vol. 136, p. 659-667, oct. 2016, doi: 10.1016/j.solener.2016.07.039.

[100] A. V. Mikhaylovskaya, M. S. Kishchik, A. D. Kotov, et N. Yu. Tabachkova, « Grain refinement during isothermal multidirectional forging due to β-phase heterogenization in Al-Mg-based alloys », *Mater. Lett.*, vol. 321, p. 132412, août 2022, doi: 10.1016/j.matlet.2022.132412.

[101] « (PDF) Processing Temperature Effect on Optical and Morphological Parameters of Organic Perovskite CH3NH3PbI3 Prepared Using Spray Pyrolysis Method ». Consulté le: 3 septembre 2025. [En ligne]. Disponible sur:

https://www.researchgate.net/publication/333985252_Processing_Temperature_Effect_on_Optical_and_Morphological_Parameters_of_Organic_Perovskite_CH3NH3PbI3_Prepared_Using_Spray_Pyrolysis_Method

[102] J. B. Whitaker *et al.*, « Scalable slot-die coating of high performance perovskite solar cells », *Sustain. Energy Fuels*, vol. 2, nº 11, p. 2442-2449, oct. 2018, doi: 10.1039/C8SE00368H.

[103] A. Vijayan, M. B. Johansson, S. Svanström, U. B. Cappel, H. Rensmo, et G. Boschloo, « Simple Method for Efficient Slot-Die Coating of MAPbI3 Perovskite Thin Films in Ambient Air Conditions », *ACS Appl. Energy Mater.*, vol. 3, nº 5, p. 4331-4337, mai 2020, doi: 10.1021/acsaem.0c00039.

[104] L. Gao, K. Huang, C. Long, F. Zeng, B. Liu, et J. Yang, « Fully slot-die-coated perovskite solar cells in ambient condition », *Appl. Phys. A*, vol. 126, mai 2020, doi: 10.1007/s00339-020-03628-w.

[105] Z. Zhang *et al.*, « Progress on Inkjet Printing Technique for Perovskite Films and Their Optoelectronic and Optical Applications », *ACS Photonics*, vol. 10, sept. 2023, doi: 10.1021/acsphotonics.3c00897.

[106] F. Mathies, E. List-Kratochvil, et E. Unger, « Advances in Inkjet-Printed Metal Halide Perovskite Photovoltaic and Optoelectronic Devices », *Energy Technol.*, vol. 8, déc. 2019, doi: 10.1002/ente.201900991.

[107] X. Peng *et al.*, « Solar Cells: Perovskite and Organic Solar Cells Fabricated by Inkjet Printing: Progress and Prospects (Adv. Funct. Mater. 41/2017) », *Adv. Funct. Mater.*, vol. 27, nº 41, 2017, doi: 10.1002/adfm.201770246.

[108] Z. Li *et al.*, « Ink Engineering of Inkjet Printing Perovskite », *ACS Appl. Mater. Interfaces*, vol. 12, nº 35, p. 39082-39091, sept. 2020, doi: 10.1021/acsami.0c09485.

[109] « An Overview of Current Printing Technologies for Large-Scale Perovskite Solar Cell Development ». Consulté le: 6 septembre 2025. [En ligne]. Disponible sur: https://www.mdpi.com/1996-1073/16/1/190

[110] « Challenges for commercializing perovskite solar cells | Science ». Consulté le: 6 septembre 2025. [En ligne]. Disponible sur: https://www.science.org/doi/10.1126/science.aat8235

[111] « Long-term operating stability in perovskite photovoltaics | Nature Reviews Materials ». Consulté le: 6 septembre 2025. [En ligne]. Disponible sur: https://www.nature.com/articles/s41578-023-00582-w

[112] « Mitigating Lead Toxicity in Halide Perovskite Solar Cells: Strategies for Sustainable Development ». Consulté le: 6 septembre 2025. [En ligne]. Disponible sur: https://www.mdpi.com/2304-6740/13/4/123

[113] J. Yan, T. J. Savenije, L. Mazzarella, et O. Isabella, « Progress and challenges on scaling up of perovskite solar cell technology », *Sustain. Energy Fuels*, vol. 6, nº 2, p. 243-266, 2022, doi: 10.1039/D1SE01045J.

[114] D. Chen *et al.*, « An efficient TeO2/Ag transparent top electrode for 20%-efficiency bifacial perovskite solar cells with a bifaciality factor exceeding 80% », *J. Mater. Chem. A*, vol. 7, nº 25, p. 15156-15163, juin 2019, doi: 10.1039/C9TA02389E.

[115] S. A. Hashemi, S. Ramakrishna, et A. G. Aberle, « Recent progress in flexible–wearable solar cells for self-powered electronic devices », *Energy Environ. Sci.*, vol. 13, nº 3, p. 685-743, mars 2020, doi: 10.1039/C9EE03046H.

[116] « Recent Development of Lead-Free Perovskite Solar Cells | IntechOpen ». Consulté le: 6 septembre 2025. [En ligne]. Disponible sur: https://www.intechopen.com/chapters/83565

[117] A. W. Y. Ho-Baillie, J. Zheng, M. A. Mahmud, F.-J. Ma, D. R. McKenzie, et M. A. Green, « Recent progress and future prospects of perovskite tandem solar cells », *Appl. Phys. Rev.*, vol. 8, nº 4, p. 041307, oct. 2021, doi: 10.1063/5.0061483.

[118] Y. Tu *et al.*, « Perovskite Solar Cells for Space Applications: Progress and Challenges », *Adv. Mater.*, vol. 33, p. 2006545, avr. 2021, doi: 10.1002/adma.202006545.

[119] G. Tang, L. Chen, X. Cao, Y. Wang, H. Zhang, et Q. Tai, « A Review on Recent Advances in Flexible Perovskite Solar Cells », *Sol. RRL*, vol. 9, nº 5, p. 2400844, 2025, doi: 10.1002/solr.202400844.

[120] « Recent Advances in Flexible Perovskite Solar Cells: Fabrication and Applications - Yang - 2019 - Angewandte Chemie International Edition - Wiley Online Library ». Consulté le: 13 septembre 2025. [En ligne]. Disponible sur: https://onlinelibrary.wiley.com/doi/full/10.1002/anie.201809781

[121] W. Tress, N. Marinova, T. Moehl, S. Zakeeruddin, M. Nazeeruddin, et M. Graetzel, « Understanding the rate-dependent J-V hysteresis, slow time component, and aging in CH3NH3PbI3 perovskite solar cells: The role of a compensated electric field », *Energy Env. Sci*, vol. 8, janv. 2015, doi: 10.1039/C4EE03664F.

[122] « Transparent Conducting Oxide Semiconductors for Transparent Electrodes | Request PDF ». Consulté le: 13 septembre 2025. [En ligne]. Disponible sur: https://www.researchgate.net/publication/230977466_Transparent_Conducting_Oxide_Semiconductors_for_Transparent_Electrodes

[123] Q. Jiang *et al.*, « Surface passivation of perovskite film for efficient solar cells », *Nat. Photonics*, vol. 13, p. 1, juill. 2019, doi: 10.1038/s41566-019-0398-2.

[124] M. Ghidiu, M. Lukatskaya, M.-Q. Zhao, Y. Gogotsi, et M. Barsoum, « Conductive Two-Dimensional Titanium Carbide 'Clay' with High Volumetric Capacitance », *Nature*, vol. advance online publication, nov. 2014, doi: 10.1038/nature13970.

[125] « 2D metal carbides and nitrides (MXenes) for energy storage | Nature Reviews Materials ». Consulté le: 13 septembre 2025. [En ligne]. Disponible sur: https://www.nature.com/articles/natrevmats201698

[126] Y. Li *et al.*, « MXene-based materials for efficient applications in perovskite solar cells: A review », *J. Mater. Sci. Technol.*, vol. 215, p. 214-232, avr. 2025, doi: 10.1016/j.jmst.2024.07.022.

[127] « Tunable physical properties of Al-doped ZnO thin films by O2 and Ar plasma treatments - IOPscience ». Consulté le: 13 septembre 2025. [En ligne]. Disponible sur: https://iopscience.iop.org/article/10.1088/2053-1591/ac3f0a?utm_source=wiley&getft_integrator=wiley

[128] « Schottky-Barrier-Free Contacts with Two-Dimensional Semiconductors by Surface-Engineered MXenes | Journal of the American Chemical Society ». Consulté le: 13 septembre 2025. [En ligne]. Disponible sur: https://pubs.acs.org/doi/10.1021/jacs.6b10834

[129] C. Dubey, D. K. Jarwal, H. Kumar, Y. Kumar, K. Mummaneni, et G. Rawat, « Development of Highly Efficient ZnO Nanorod-Based Nontoxic Perovskite Solar Cell Using AZO Buffer Layer and Lanthanide Doping », *IEEE Trans. Electron Devices*, vol. 69, nº 2, p. 622-630, févr. 2022, doi: 10.1109/TED.2021.3138375.

[130] « Numerical Investigation of Electron/Hole Transport Layer for Enhancement of Ecofriendly Tin-Ge Based Perovskite Solar Cell: Energy Sources, Part A: Recovery, Utilization, and Environmental Effects: Vol 45 , No 1 - Get Access ». Consulté le: 13 septembre 2025. [En ligne]. Disponible sur: https://www.tandfonline.com/doi/full/10.1080/15567036.2023.2192182

[131] « A Comparative Study of Quantum Dot Solar Cell with Two Different ETLs of WS2 and IGZO Using SCAPS-1D Simulator ». Consulté le: 13 septembre 2025. [En ligne]. Disponible sur: https://www.mdpi.com/2673-9941/2/3/20

[132] « Emerging BaZrS3 and Ba(Zr,Ti)S3 Chalcogenide Perovskite Solar Cells: A Numerical Approach Toward Device Engineering and Unlocking Efficiency | ACS Omega ». Consulté le: 13 septembre 2025. [En ligne]. Disponible sur: https://pubs.acs.org/doi/10.1021/acsomega.3c06627?src=getftr&utm_source=wiley&getft_integrator=wiley

[133] « CuSCN as Hole Transport Material with 3D/2D Perovskite Solar Cells | ACS Applied Energy Materials ». Consulté le: 13 septembre 2025. [En ligne]. Disponible sur: https://pubs.acs.org/doi/10.1021/acsaem.9b01692

[134] « Bifunctional hole-shuttle molecule for improved interfacial energy level alignment and defect passivation in perovskite solar cells | Nature Energy ». Consulté le: 13 septembre 2025. [En ligne]. Disponible sur: https://www.nature.com/articles/s41560-023-01249-0

[135] B. Bibi, B. Farhadi, W. U. Rahman, et A. Liu, « Numerical modeling and performance analysis of a novel Cd-free all-Kesterite tandem solar cell using SCAPS-1D », *Mater.*, vol. 2, p. 100068, janv. 2024, doi: 10.1016/j.nxmate.2023.100068.

[136] N. Rono, A. E. Merad, J. K. Kibet, B. S. Martincigh, et V. O. Nyamori, « Optimization of Hole Transport Layer Materials for a Lead-Free Perovskite Solar Cell Based on Formamidinium Tin Iodide », *Energy Technol.*, vol. 9, nº 12, p. 2100859, 2021, doi: 10.1002/ente.202100859.

[137] « Study of Se/Te-doped Cu2O as a hole transport material in perovskite solar cells - RSC Advances (RSC Publishing) ». Consulté le: 13 septembre 2025. [En ligne]. Disponible sur: https://pubs.rsc.org/en/content/articlelanding/2023/ra/d2ra04659h

[138] « Past achievements and future challenges in the development of optically transparent electrodes | Nature Photonics ». Consulté le: 13 septembre 2025. [En ligne]. Disponible sur: https://www.nature.com/articles/nphoton.2012.282

[139] « Bandgap Control via Structural and Chemical Tuning of Transition Metal Perovskite Chalcogenides - Niu - 2017 - Advanced Materials - Wiley Online Library ». Consulté le: 13 septembre 2025. [En ligne]. Disponible sur: https://advanced.onlinelibrary.wiley.com/doi/abs/10.1002/adma.201604733

[140] « A review of tin disulfide (SnS2) composite electrode materials for supercapacitors - Setayeshmehr - 2022 - Energy Storage - Wiley Online Library ». Consulté le: 13 septembre 2025. [En ligne]. Disponible sur: https://onlinelibrary.wiley.com/doi/abs/10.1002/est2.295

[141] « Tin Disulfide Nanosheet as Cathode Materials for Rechargeable Aluminum Ion Batteries: Synthesis, Electrochemical Performance, and Mechanism ». Consulté le: 13 septembre 2025. [En ligne]. Disponible sur: https://www.mdpi.com/1420-3049/30/8/1649

[142] « SrTiO3 based high temperature solid oxide solar cells: Photovoltages, photocurrents and mechanistic insight ». Consulté le: 14 septembre 2025. [En ligne]. Disponible sur: https://www.researchgate.net/publication/353232567_SrTiO3_based_high_temperature_solid_oxide_solar_cells_Photovoltages_photocurrents_and_mechanistic_insight

[143] P. Bhujbal *et al.*, « Unlocking the Potential of WS2 as an Electron Transport Layer in Flexible and Lead-Free Methylammonium Tin Iodide -Based Perovskite Solar Cells: A Comprehensive Defect Study Using the SCAPS-1D Framework », *ES Energy Environ.*, janv. 2024, doi: 10.30919/esee1225.

[144] Y. Shimazu, Y. Fujisawa, K. Arai, T. Iwabuchi, et K. Suzuki, « Synthesis and Characterization of Zirconium Disulfide Single Crystals and Thin-Film Transistors Based on Multilayer Zirconium Disulfide Flakes », *ChemNanoMat*, vol. 4, sept. 2018, doi: 10.1002/cnma.201800426.

[145] A. Walsh, S.-H. Wei, S. Chen, et X. Gong, *Design of quaternary chalcogenide photovoltaic absorbers through cation mutation*, vol. 1. 2009, p. 001878. doi: 10.1109/PVSC.2009.5411555.

[146] N. J. Cook, C. L. Ciobanu, L. V. Danyushevsky, et S. Gilbert, « Minor and trace elements in bornite and associated Cu–(Fe)-sulfides: A LA-ICP-MS studyBornite mineral chemistry », *Geochim. Cosmochim. Acta*, vol. 75, nº 21, p. 6473-6496, nov. 2011, doi: 10.1016/j.gca.2011.08.021.

[147] V. M. H. Cao, J. Bae, J. Shim, B. Hong, H. Jee, et J. Lee, « Fabrication of the Cu2ZnSnS4 Thin Film Solar Cell via a Photo-Sintering Technique », *Appl. Sci.*, vol. 12, nº 1, p. 38, janv. 2022, doi: 10.3390/app12010038.

[148] R. Ranjan, S. Verma, et N. M. Tripathi, « The organic HTL in highly efficient germanium-alloyed CsSnI3 perovskite solar cell: a modelling and computational analysis », *Phys. Scr.*, vol. 99, nº 6, p. 066010, mai 2024, doi: 10.1088/1402-4896/ad4e15.

[149] « (PDF) Copper |Oxide (Cu2O) Sheet Based Solar Cell ». Consulté le: 14 septembre 2025. [En ligne]. Disponible sur: https://www.researchgate.net/publication/377240961_Copper_Oxide_Cu2O_Sheet_Based_Solar_Cell

[150] T. Yang *et al.*, « Amidino-based Dion-Jacobson 2D perovskite for efficient and stable 2D/3D heterostructure perovskite solar cells », *Joule*, vol. 7, nº 3, p. 574-586, mars 2023, doi: 10.1016/j.joule.2023.02.003.

[151] Q. Dong *et al.*, « Flexible perovskite solar cells with simultaneously improved efficiency, operational stability, and mechanical reliability », *Joule*, vol. 5, nº 6, p. 1587-1601, juin 2021, doi: 10.1016/j.joule.2021.04.014.

[152] W. Chen *et al.*, « A 1D:2D structured AgNW:MXene composite transparent electrode with high mechanical robustness for flexible photovoltaics », *J. Mater. Chem. C*, vol. 10, nº 22, p. 8625-8633, juin 2022, doi: 10.1039/D2TC01178F.

[153] Q. T. Aljwari, A. M. A. Sabaawi, et Q. T. Aljwari, « A Comprehensive Study on the Effect of Defects on Perovskite Solar Cell Performance », 5 juin 2023, *Preprints*: 2023060344. doi: 10.20944/preprints202306.0344.v1.

[154] E. Priyanka et D. Muchahary, « Performance improvement of perovskite/CIGS tandem solar cell using barium stannate charge transport layer and achieving PCE of 39 % numerically », *Sol. Energy*, vol. 267, p. 112218, janv. 2024, doi: 10.1016/j.solener.2023.112218.

[155] F. Kherrat *et al.*, « Performance enhancement of eco-friendly Cs3Sb2I9-based perovskite solar cell employing Nb2O5 and CuI as efficient charge transport layers », *Micro Nanostructures*, vol. 183, p. 207676, nov. 2023, doi: 10.1016/j.micrna.2023.207676.

[156] N. Singh, A. Agarwal, et M. Agarwal, « Highly efficient lead-free ethyl ammonium substituted perovskite solar cell simulated using SCAPS 1D », *J. Phys. Chem. Solids*, vol. 186, p. 111834, mars 2024, doi: 10.1016/j.jpcs.2023.111834.

[157] « Numerical Simulation and Optimization of Highly Stable and Efficient Lead-Free Perovskite FA1−xCsxSnI3-Based Solar Cells Using SCAPS ». Consulté le: 2 octobre 2025. [En ligne]. Disponible sur: https://www.mdpi.com/1996-1944/15/14/4761

[158] K. Pandey, Sadanand, P. K. Dakua, D. K. Panda, P. K. Singh, et B. K. Pandey, « Investigation of suitable buffer layer for PbS-TBAI/PbS-EDT colloidal quantum dot solar cell using SCAPS-1D », *Optik*, vol. 298, p. 171593, mars 2024, doi: 10.1016/j.ijleo.2023.171593.

[159] E. Raza *et al.*, « Numerical modeling and performance optimization of carbon-based hole transport layer free perovskite solar cells », *Opt. Mater.*, vol. 125, p. 112075, mars 2022, doi: 10.1016/j.optmat.2022.112075.

[160] A. Kumar, S. Singh, M. K. A. Mohammed, et A. Esmail Shalan, « Effect of 2D perovskite layer and multivalent defect on the performance of 3D/2D bilayered perovskite solar cells through computational simulation studies », *Sol. Energy*, vol. 223, nº March, p. 193-201, 2021, doi: 10.1016/j.solener.2021.05.042.

[161] S. Karthick, J. Bouclé, et S. Velumani, « Effect of bismuth iodide (BiI3) interfacial layer with different HTL's in FAPI based perovskite solar cell – SCAPS – 1D study », *Sol. Energy*, vol. 218, nº March, p. 157-168, 2021, doi: 10.1016/j.solener.2021.02.041.

[162] N. Shrivastav *et al.*, « Perovskite-CIGS Monolithic Tandem Solar Cells with 29.7% Efficiency: A Numerical Study », *Energy Fuels*, vol. 37, nº 4, p. 3083-3090, 2023, doi: 10.1021/acs.energyfuels.2c03973.

[163] M. Mottakin *et al.*, « Photoelectric performance of environmentally benign Cs2TiBr6-based perovskite solar cell using spinel NiCo2O4 as HTL », *Optik*, vol. 272, nº November 2022, p. 170232, 2023, doi: 10.1016/j.ijleo.2022.170232.

[164] N. Singh, A. Agarwal, et M. Agarwal, « Highly efficient lead-free ethyl ammonium substituted perovskite solar cell simulated using SCAPS 1D », *J. Phys. Chem. Solids*, vol. 186, nº December 2023, p. 111834, 2024, doi: 10.1016/j.jpcs.2023.111834.

[165] H. Heffner, M. Soldera, et A. F. Lasagni, « Optical Enhancement of Fluorine-Doped Tin Oxide Thin Films using Infrared Picosecond Direct Laser Interference Patterning », *Adv. Eng. Mater.*, vol. 24, nº 11, p. 2200266, 2022, doi: 10.1002/adem.202200266.

[166] M. Saliba *et al.*, « Cesium-containing triple cation perovskite solar cells: improved stability, reproducibility and high efficiency », *Energy Environ. Sci.*, vol. 9, nº 6, p. 1989-1997, 2016, doi: 10.1039/C5EE03874J.

[167] W. Dou, Z. Yin, Y. Zhang, H. Deng, et N. Dai, « Two-Dimensional Perovskite (PEA)2PbI4 Two-Color Blue-Green Photodetector », *Nanomaterials*, vol. 12, nº 15, p. 2556, juill. 2022, doi: 10.3390/nano12152556.

[168] L. Zhu *et al.*, « Performance enhancement of perovskite solar cells using a La-doped BaSnO3 electron transport layer », *J. Mater. Chem. A*, vol. 5, nº 7, p. 3675-3682, févr. 2017, doi: 10.1039/C6TA09689A.

[169] X. Ling *et al.*, « Room-Temperature Processed Nb2O5 as the Electron-Transporting Layer for Efficient Planar Perovskite Solar Cells », *ACS Appl. Mater. Interfaces*, vol. 9, nº 27, p. 23181-23188, juill. 2017, doi: 10.1021/acsami.7b05113.

[170] T. AlZoubi, B. Mourched, M. Al Gharram, G. Makhadmeh, et O. Abu Noqta, « Improving Photovoltaic Performance of Hybrid Organic-Inorganic MAGeI3 Perovskite Solar Cells via Numerical Optimization of Carrier Transport Materials (HTLs/ETLs) », *Nanomaterials*, vol. 13, nº 15, p. 2221, juill. 2023, doi: 10.3390/nano13152221.

[171] F. Igbari, M. Li, Y. Hu, Z.-K. Wang, et L.-S. Liao, « A room-temperature CuAlO2 hole interfacial layer for efficient and stable planar perovskite solar cells », *J. Mater. Chem. A*, vol. 4, nº 4, p. 1326-1335, janv. 2016, doi: 10.1039/C5TA07957H.

[172] K. Hossain *et al.*, « Resolving the Hydrophobicity of the Me-4PACz Hole Transport Layer for Inverted Perovskite Solar Cells with Efficiency >20% », *ACS Energy Lett.*, vol. 8, nº 9, p. 3860-3867, sept. 2023, doi: 10.1021/acsenergylett.3c01385.

[173] S. Wang, L. Wang, C. Liu, Y. Shan, F. Li, et L. Sun, « NiCo2O4 thin film prepared by electrochemical deposition as a hole-transport layer for efficient inverted perovskite solar cells », *RSC Adv.*, vol. 12, nº 20, p. 12544-12551, avr. 2022, doi: 10.1039/D2RA01816K.

[174] W. Ke, D. Zhao, C. R. Grice, A. J. Cimaroli, G. Fang, et Y. Yan, « Efficient fully-vacuum-processed perovskite solar cells using copper phthalocyanine as hole selective layers », *J. Mater. Chem. A*, vol. 3, nº 47, p. 23888-23894, nov. 2015, doi: 10.1039/C5TA07829F.

[175] H. Zhang *et al.*, « Low-Temperature Solution-Processed CuCrO2 Hole-Transporting Layer for Efficient and Photostable Perovskite Solar Cells », *Adv. Energy Mater.*, vol. 8, nº 13, p. 1702762, 2018, doi: 10.1002/aenm.201702762.

[176] S. Rabhi, T. Hidouri, S. Goumri-Said, H. J. Alathlawi, G. M. Alsulaim, et M. Waqas Alam, « Bifacial perovskite solar cells with >21 % efficiency: Computational insights into novel HTLs materials and architectures », *Sol. Energy*, vol. 284, p. 113083, déc. 2024, doi: 10.1016/j.solener.2024.113083.

[177] Y. S. Lee *et al.*, « Cu2ZnSnSe4 Thin-Film Solar Cells by Thermal Co-evaporation with 11.6% Efficiency and Improved Minority Carrier Diffusion Length », *Adv. Energy Mater.*, vol. 5, nº 7, p. 1401372, 2015, doi: 10.1002/aenm.201401372.

[178] « Analysis of Optical and Recombination Losses in Solar Cells | SpringerLink ». Consulté le: 3 octobre 2025. [En ligne]. Disponible sur: https://link.springer.com/chapter/10.1007/978-3-319-95138-6_2

[179] N. R. Pochont et Y. R. Sekhar, « Numerical Simulation of Nitrogen-Doped Titanium Dioxide as an Inorganic Hole Transport Layer in Mixed Halide Perovskite Structures Using SCAPS 1-D », *Inorganics*, vol. 11, nº 1, p. 3, janv. 2023, doi: 10.3390/inorganics11010003.

[180] S. Rabhi, G. M. Alsulaim, Y. I. Bouderbala, et M. W. Alam, « Enhancing inverted perovskite solar cells: The role of o-OMe-PEAI interlayer in performance with MXene as alternative front contacts », *Inorg. Chem. Commun.*, vol. 175, p. 114096, mai 2025, doi: 10.1016/j.inoche.2025.114096.

[181] N. Bouri *et al.*, « Comparative study of solar cells based on triple and graded absorber layers with the compound CsSn1-xGexI3: Numerical study and optimization », *J. Phys. Chem. Solids*, vol. 199, p. 112561, avr. 2025, doi: 10.1016/j.jpcs.2025.112561.

[182] D. E. Tareq, S. M. AbdulAlmohsin, et H. H. Waried, « Efficiency of TiO2/Perovskites/Cu2O Solar Cells with Optimal Thickness at Varying of Environment Temperature », *IOP Conf. Ser. Mater. Sci. Eng.*, vol. 928, nº 7, p. 072044, nov. 2020, doi: 10.1088/1757-899X/928/7/072044.

[183] W. E. I. Sha, X. Ren, L. Chen, et W. C. H. Choy, « The efficiency limit of CH3NH3PbI3 perovskite solar cells », *Appl. Phys. Lett.*, vol. 106, nº 22, p. 221104, juin 2015, doi: 10.1063/1.4922150.

[184] H. El-assib *et al.*, « High-performance optimization and analysis of $Cs_2CuSbCl_6$-Based lead-free double perovskite solar cells with theoretical efficiency exceeding 27 % », *Renew. Energy*, vol. 239, p. 122092, févr. 2025, doi: 10.1016/j.renene.2024.122092.

[185] « Evaluating CZTS Solar Cell Performance Based on Generation and Recombination Models for Possible ETLs Through Numerical Analysis | Journal of Electronic Materials ». Consulté le: 3 octobre 2025. [En ligne]. Disponible sur: https://link.springer.com/article/10.1007/s11664-024-10930-3

[186] N. K. Sinha, D. S. Ghosh, et A. Khare, « A Comprehensive Guide to Bifacial Perovskite Solar Cells: Simulation and Optimization », *Adv. Theory Simul.*, vol. 7, nº 1, p. 2300633, 2024, doi: 10.1002/adts.202300633.

[187] K. Sekar, L. Marasamy, S. Mayarambakam, P. Selvarajan, et J. Bouclé, « Highly efficient lead-free silver bismuth iodide (Ag3BiI6) rudorffite solar cells with novel device architecture: A numerical study », *Mater. Today Commun.*, vol. 38, p. 108347, mars 2024, doi: 10.1016/j.mtcomm.2024.108347.

[188] A. Mortadi, E. M. El Hafidi, Hamid. Nasrellah, M. Monkade, et R. El Moznine, « Investigation of bandgap grading on performances of perovskite solar cell using SCAPS-1D and impedance spectroscopy », *Sol. Energy Adv.*, vol. 4, p. 100056, janv. 2024, doi: 10.1016/j.seja.2024.100056.

[189] F. Behrouznejad, S. Shahbazi, N. Taghavinia, H.-P. Wu, et E. W.-G. Diau, « A study on utilizing different metals as the back contact of CH3NH3PbI3 perovskite solar cells », *J. Mater. Chem. A*, vol. 4, nº 35, p. 13488-13498, août 2016, doi: 10.1039/C6TA05938D.

[190] Q. Jiang *et al.*, « Highly efficient bifacial single-junction perovskite solar cells », *Joule*, vol. 7, nº 7, p. 1543-1555, juill. 2023, doi: 10.1016/j.joule.2023.06.001.

[191] M. Burgelman, P. Nollet, et S. Degrave, « Modelling polycrystalline semiconductor solar cells », *Thin Solid Films*, vol. 361-362, p. 527-532, févr. 2000, doi: 10.1016/S0040-6090(99)00825-1.

[192] M. A. Shafi, H. Ullah, S. Ullah, L. Khan, S. Bibi, et B. M. Soucase, « Numerical Simulation of Lead-Free Sn-Based Perovskite Solar Cell by Using SCAPS-1D », *Eng. Proc.*, vol. 12, nº 1, p. 92, 2022, doi: 10.3390/engproc2021012092.

[193] S. Kaynak, B. Kaynak, et A. Özmen, « A software tool development study for solar energy potential analysis », *Energy Build.*, vol. 162, p. 134-143, mars 2018, doi: 10.1016/j.enbuild.2017.12.033.

[194] M. Koivisto *et al.*, « Using time series simulation tools for assessing the effects of variable renewable energy generation on power and energy systems », *Wiley Interdiscip. Rev. Energy Environ.*, vol. 8, p. e329, oct. 2018, doi: 10.1002/wene.329.

[195] S. R. Hosseini *et al.*, « Investigating the effect of non-ideal conditions on the performance of a planar CH3NH3PbI3-based perovskite solar cell through SCAPS-1D simulation », *Heliyon*, vol. 8, nº 11, p. e11471, nov. 2022, doi: 10.1016/j.heliyon.2022.e11471.

[196] S. Banik, A. Das, B. K. Das, et N. Islam, « Numerical simulation and performance optimization of a lead-free inorganic perovskite solar cell using SCAPS-1D », *Heliyon*, vol. 10, nº 1, p. e23985, janv. 2024, doi: 10.1016/j.heliyon.2024.e23985.

[197] « SCAPS Empowered Machine Learning Modelling of Perovskite Solar Cells: Predictive Design of Active Layer and Hole Transport Materials ». Consulté le: 11 septembre 2025. [En ligne]. Disponible sur: https://www.mdpi.com/2304-6732/10/3/271

[198] E. Paz Totolhua *et al.*, « Numerical Simulation of an Inverted Perovskite Solar Cell Using a SiOx Layer as Down-Conversion Energy Material to Improve Efficiency and Stability », *Materials*, vol. 16, nº 23, p. 7445, janv. 2023, doi: 10.3390/ma16237445.

Annex

SCAPS 1D Simulation Workflow and Functional Setup

Following the analytical examination of photovoltaic performance indicators in Section 2.4 such as the open-circuit voltage (V_{OC}), short-circuit current density (J_{SC}), fill factor (FF), and power conversion efficiency (PCE) it becomes essential to shift from theoretical formulations to their practical implementation within a dedicated simulation environment. Although analytical expressions provide valuable insights into the fundamental physical processes, they are limited in their ability to describe the full complexity of real photovoltaic devices, particularly those with multilayer architectures, material imperfections, and nonlinear behavior under varying operating conditions.

Numerical simulation tools such as SCAPS 1D offer an advanced framework to bridge this gap by solving the governing semiconductor equations (Poisson and continuity) under realistic boundary conditions and material parameters. This approach enables accurate modeling of carrier transport, recombination dynamics, and optical absorption within user-defined device structures. In this way, theoretical concepts are translated into a numerical multilayer model capable of generating electrical and optical responses that closely mimic experimental conditions.

To initiate this practical dimension, Figure A.1 presents the general interface of SCAPS 1D, specifically the Action Panel, which serves as the core control center for setting operating conditions, selecting simulation types, and executing the corresponding numerical calculations.

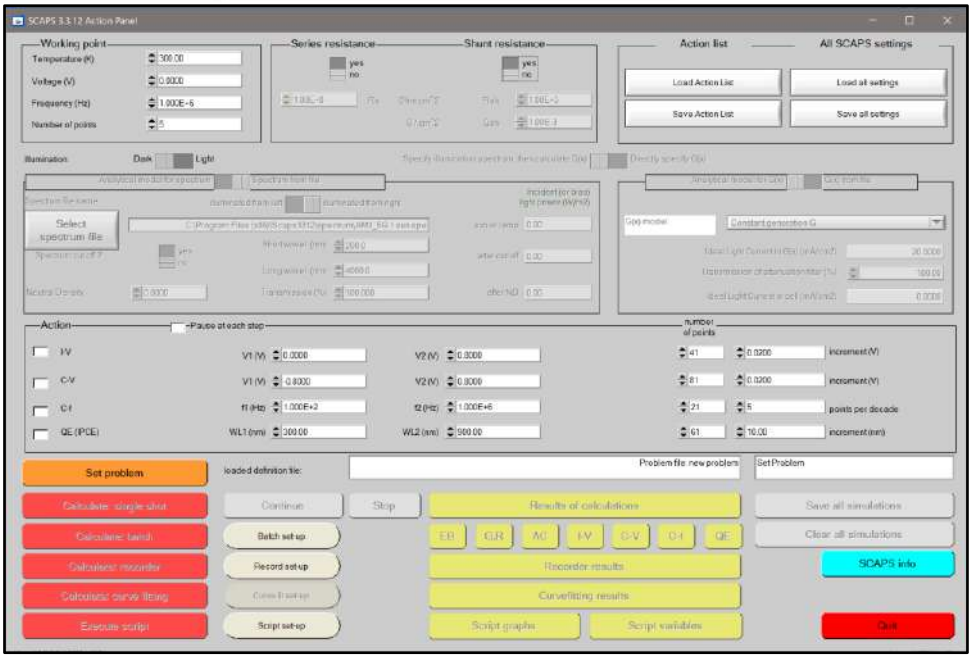


Figure A.1 General view of the SCAPS 1D Action Panel interface.

For a clearer and more structured understanding, the interface is subdivided into ten functional zones, each responsible for a distinct aspect of simulation setup or control. These zones are illustrated and numbered in Figure A.2.

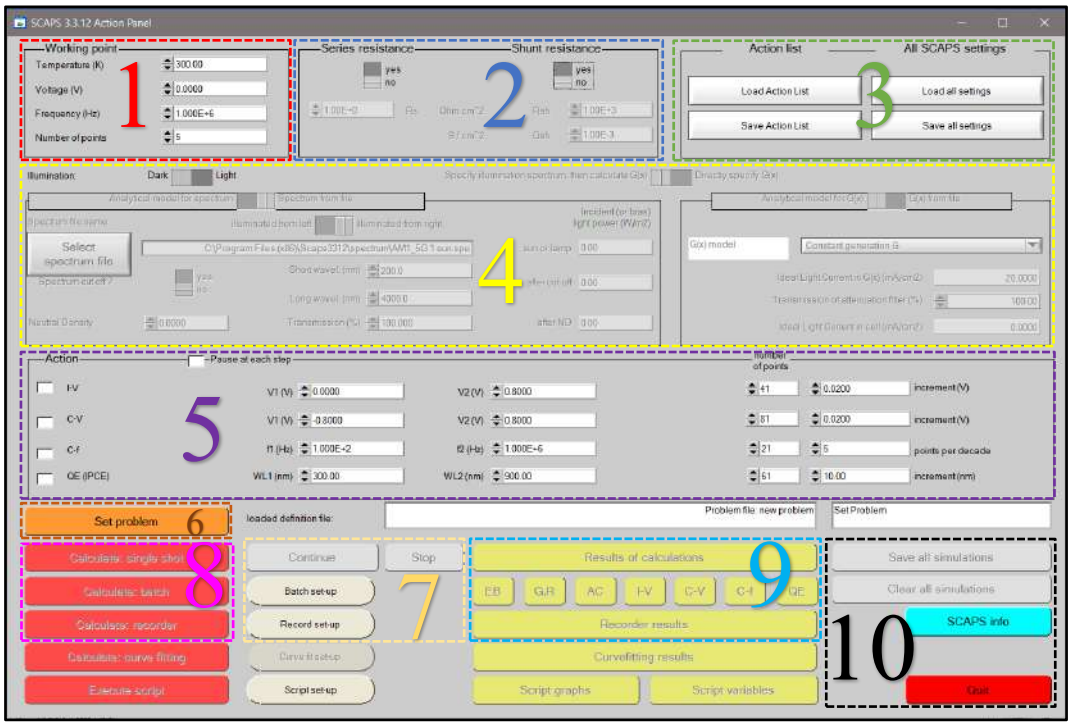


Figure A.2 Division of the Action Panel into 10 functional zones, labeled for detailed explanation.

Zone 1 - Working Point Parameters

The Working Point in SCAPS 1D defines the baseline physical conditions under which the solar cell device is simulated. These parameters are not varied during a single simulation run but remain constant, providing the fixed environment in which the numerical model operates. Zone 1 includes four key input variables: temperature, bias voltage, frequency, and the number of calculation points. Each of these contributes to defining the simulation context, influencing either the electronic transport properties or the resolution of the output curves.

- **Temperature (T):** Temperature affects multiple semiconductor properties, including the effective density of states in the conduction $N_C(T)$ and valence bands $N_V(T)$, carrier thermal velocities, and the thermal voltage $\frac{KT}{q}$. Importantly, SCAPS 1D does not automatically adjust temperature-dependent material parameters. The user is responsible for inputting all material-specific properties corresponding to the chosen temperature, such as energy bandgap, carrier mobility, and defect characteristics. A commonly used value is T= 300 K, which corresponds to standard test conditions under the AM1.5G solar spectrum.
- **Bias Voltage (V):** This voltage serves as a fixed DC bias in C-f and QE(λ) simulations, determining the electrical condition under which the optical or frequency response is evaluated. However, in I-V and C-V simulations, this value is ignored entirely, as the program automatically starts from v = 0V and sweeps through the defined range specified elsewhere in the simulation settings.
- **Frequency (*f*):** This field is only relevant in C-V simulations, where it defines the frequency at which the capacitance is evaluated. For all other simulation modes I-V, QE(λ), and C-f the frequency setting is discarded. A standard test frequency of f=10^6 Hz (1 MHz) is commonly used in C-V measurements to reflect high-speed switching conditions in practical testing.

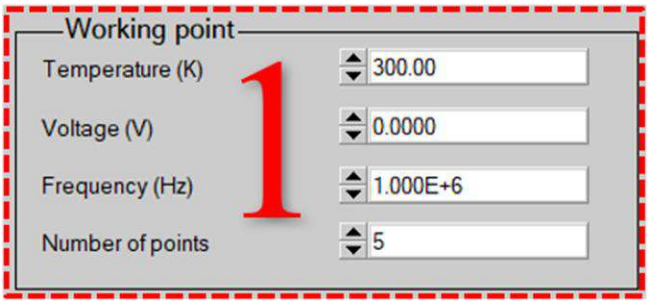


Figure A.3 Working Point Parameters Section in the SCAPS 1D Action Panel.

Zone 2 - Series and Shunt Resistance Configuration:

This section of the SCAPS 1D interface provides an essential tool for incorporating non-ideal electrical behaviors into the solar cell model. Through this zone, the user can introduce the effects of parasitic resistances specifically series resistance (R_s) and shunt resistance (R_{sh}) which are critical for modeling realistic deviations from ideal device performance.

- **Series Resistance (**Rs**):** represents the total ohmic losses encountered by charge carriers as they travel through the different layers of the solar cell, particularly the transparent conducting oxide (TCO), the absorber layer, and the metallic contacts. An increase in Rs causes a noticeable distortion in the forward region of the current-voltage (J-V) curve, reducing the slope and, consequently, the fill factor (FF) and output power. In high-performance devices, the typical range for Rs is between 0.5 and 2.0 Ω·cm², depending on layer thickness, material resistivity, and contact design. Accurate modeling of Rs is crucial for interpreting power losses due to series connections and for reproducing realistic J-V characteristics.

- **Shunt Resistance (**R_{sh}**):** models leakage pathways that allow current to bypass the intended p-n junction. These pathways may result from structural defects such as pinholes, grain boundaries, poor encapsulation, or improper back contact fabrication. A low Rsh leads to increased recombination losses and a reduction in both the open-circuit voltage (V_{OC}) and overall device efficiency. Ideally, Rsh should be significantly higher than 1000 Ω.cm² to minimize its impact on current leakage and performance degradation. This parameter is especially relevant in studies of device uniformity, fabrication quality, and defect-related losses.

- **Using Conductance Instead of Resistance:** SCAPS 1D also allows the user to input the inverse values conductances directly: $G_s = \frac{1}{R_s}$ and $G_{sh} = \frac{1}{R_{sh}}$. This is particularly useful when working with experimental data presented in terms of conductance or when dealing with very high or low resistance values that may introduce numerical instability. In practice, entering conductance may be preferable in advanced modeling scenarios, especially when optimizing device designs or automating simulation scripts.

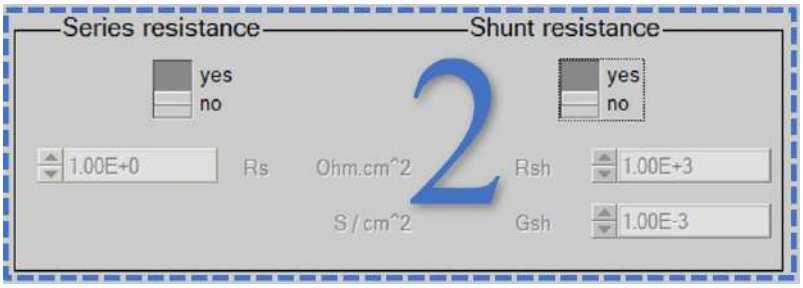


Figure A.4 Series and Shunt Resistance Configuration Panel in the SCAPS 1D Interface.

Zone 3 - Project Configuration and Action List Management:

This section of the SCAPS 1D interface provides essential tools for managing simulation workflows, storing complete configuration files, and maintaining the reproducibility of numerical experiments. It is particularly valuable in multi-step simulation processes, where consistency and data retention are critical for comparative or parametric studies.

- **The Action List:** feature allows users to define and save a customized sequence of simulations such as J-V, QE, and energy band diagram that can be executed in a fixed order. This is especially useful in cases where multiple device configurations are being tested under the same simulation protocol. Action lists streamline the simulation workflow, reduce user errors, and ensure procedural consistency across models.

- **Saving and Loading Global SCAPS Settings:** This functionality enables the user to store the entire simulation environment in a single file, which may include:

    - Layer parameters (thickness, bandgap, carrier type, doping density)
    - Bulk and interface defect properties
    - Contact type and biasing conditions
    - Illumination settings and spectral input
    - Chosen simulation modes and sweep ranges

SCAPS stores these configurations in its proprietary file formats (e.g., `SCI`, `SET`), allowing for seamless restoration at any time. This is particularly beneficial when performing iterative simulations or sharing standardized setups with collaborators.

- **Scientific Importance of This Functionality:** From an academic perspective, the ability to save and reload full simulation setups plays a vital role in ensuring reproducibility and data traceability, which are foundational principles of scientific

research. Saving configurations ensures that every simulation scenario is fully documented and can be revisited or repeated in future work. It also facilitates comparative modeling, such as when studying the impact of a single layer's modification while keeping all other parameters fixed. According to the official SCAPS manual, this functionality is critical for long-term research projects and makes SCAPS particularly suitable for advanced photovoltaic modeling and optimization workflows.



Figure A.5 Action List and Global Settings Panel in the SCAPS 1D Interface.

Zone 4 -Illumination and Spectrum Settings

Illumination settings are among the most critical factors defining the photovoltaic response of solar cells, as they directly control the photogeneration of charge carriers through optical absorption. Zone 4 of the SCAPS 1D interface offers a comprehensive set of tools for specifying spectral characteristics, light incidence direction, power intensity, and internal generation models. These parameters are essential not only for simulating the short-circuit current density J_{SC} and quantum efficiency (QE), but also for mimicking real-world operating conditions of multilayer solar devices.

- **Spectrum Selection:** SCAPS 1D allows users to input external spectral data typically in .spe format or to use built-in illumination spectra such as AM1.5G, a globally accepted reference spectrum that represents standard solar radiation at an intensity of 1000 W/m2The user may also define monochromatic or filtered spectra to represent laboratory-specific or indoor light sources. The chosen spectrum directly affects the calculation of the generation rate and absorption profile within each layer, making it a critical component in realistic device modeling.

- **Illumination Direction:** The interface provides the option to define the side from which light enters the device either from the front (top) or the back. This is crucial when simulating non-symmetric or bifacial cells, as the internal absorption and recombination

mechanisms vary with the light incidence direction. Typically, illumination is applied from the top through the TCO layer, but advanced architectures like vertically stacked or tandem devices may require reverse or dual-sided illumination modeling.

- **Spectral Range:** SCAPS 1D offers full control over the simulation wavelength window, enabling the researcher to restrict or expand the spectral range (e.g., 300-900 nm) based on material absorption characteristics. This is particularly useful in QE analysis and when comparing absorber materials with distinct spectral responses, such as perovskite versus silicon. The ability to define the spectral range is key to resolving photon-limited versus recombination-limited behavior.

- **Bias Illumination and Light Intensity:** For specific simulation types like QE and C-f analysis, users can apply a bias light a continuous low-level illumination simultaneous with the main source. This option allows for the emulation of partial illumination or background solar flux, approximating realistic operational conditions. The absolute light power can be adjusted in physical units ($W.m^{-2}$), making the tool adaptable to experimental lab settings or solar simulator configurations.

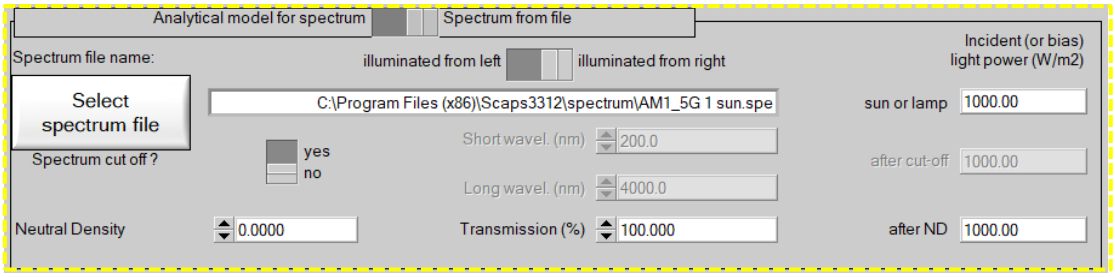


Figure A.6 Spectral Source and Illumination Direction Settings in SCAPS 1D.

- **Photogeneration Profile G(x):** Accurate modeling of the internal carrier generation profile G(x) is fundamental for predicting device performance. SCAPS 1D offers two main approaches:
    - **Built-in optical absorption model:** Generation is computed numerically based on the selected spectrum and material properties (absorption coefficients, thickness, etc.).
    - **External generation file import:** The user can load a spatially resolved generation profile from optical simulation tools (e.g., TMM, COMSOL),

enabling highly precise modeling of interference, reflection, and standing-wave effects in multilayer structures.

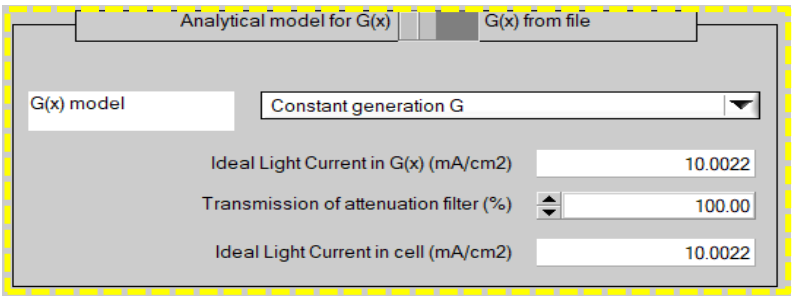


Figure A.7 Definition of the Carrier Generation Profile G(x) in SCAPS 1D.

Zone 5 - Simulation Type and Parameter Range Definition

This section represents the operational core of the SCAPS 1D interface, where the user selects the type of physical analysis to be executed and defines the corresponding numerical sweep ranges. It serves as the gateway between the structural configuration of the solar cell and the extraction of performance results. The interface enables the implementation of realistic electrical and optical simulations under controlled conditions, and it plays a key role in determining critical performance metrics such as V_{OC}, J_{SC}, Fill Factor (FF), and Power Conversion Efficiency (PCE).

The panel supports four principal simulation modes:

- **I - V: Current–Voltage Characteristics:** This function simulates the photovoltaic response of the device under a voltage sweep, typically ranging from negative bias to above the open-circuit voltage. The user specifies the start and end voltages (V1 and V2), the number of calculation points, and the voltage increment. **Common use:** To extract key performance indicators such as:

    - Short-circuit current J_{SC}
    - Open-circuit voltage V_{OC}
    - Maximum power point (V_{mp}, J_{mp})
    - Fill Factor and PCE

    This simulation is also useful for detecting S-shaped I-V curves, roll-off effects, or contact mismatches caused by interface defects or recombination phenomena.

- **C-V (Capacitance-Voltage) Profiling:** The C-V simulation is designed to assess the device's electrostatic response under bias at a fixed frequency (typically 1 - 100 kHz). It reveals:

    - Effective doping concentration via $\frac{1}{C^2-V}$ slope
    - Depletion region width
    - Built-in voltage or flat-band voltage
    - Interface-related anomalies (e.g., barrier formation or charge trapping)

  This mode is widely used to validate doping gradients, interface quality, and to extract critical device physics parameters.

- **C-f (Capacitance-Frequency Sweep):** The C-f analysis models the dynamic dielectric response of the device across a range of frequencies. The user defines the frequency limits (f1 and f2), the number of points, and optionally sets a logarithmic point density (points per decade).
  Applications include:

    - Evaluating trap-state response times
    - Investigating slow recombination mechanisms
    - Isolating interfacial contributions in complex device stacks

  This method is particularly valuable for diagnosing transient behavior and defect-related time constants.

- **QE (IPCE) Quantum Efficiency Spectrum:** This mode simulates the wavelength-dependent responsivity of the solar cell. The user enters the start and end wavelengths (WL1 and WL2), the number of points, and the spectral increment.
  From this simulation, one can obtain:

    - External Quantum Efficiency (EQE)
    - Internal Quantum Efficiency (IQE)
    - Spectral loss mechanisms
    - Layer-specific contributions to photocurrent generation

  QE analysis is crucial for verifying light absorption and carrier collection across the device, and is often used to compare simulated results with laboratory spectrophotometer data.

- **Additional Features in the Interface**
    - **Pause at each step:** When enabled, the simulation halts after each sub-analysis, allowing the user to review intermediate results. This is particularly useful in sensitivity studies or when analyzing a parameter step-by-step.
    - **Number of points & increment:** These inputs control the resolution of the sweep and the precision of output data. Choosing appropriate values balances accuracy and computational time.
    - **Vertical alignment of modes:** Each simulation type has a dedicated row with corresponding input fields, making the interface intuitive and modular.

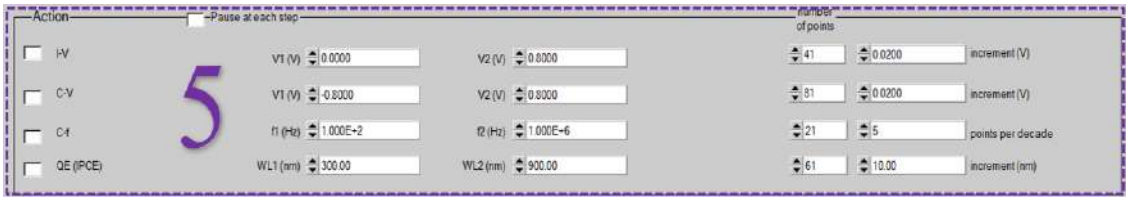


Figure A.8 Simulation Type and Sweep Range Configuration Panel in SCAPS 1D.

Zone 6 - Setting Up the Solar Cell Structure (Set Problem)

a)- Layer Definition and Material Properties

The top section of the "Set Problem" window is dedicated to defining the layered structure of the solar cell and assigning detailed material properties to each layer. Here, the user can specify the number of layers, their thicknesses, bandgaps, electron affinities, doping types (p-type or n-type), density of states for electrons and holes, carrier mobilities, and permittivities. In addition to these intrinsic properties, defect-related parameters can be included, such as the position of defects within the energy gap, their type (donor or acceptor), capture cross-sections, and their effect on carrier recombination. The user also sets the characteristics of the front and back metal contacts, including their work functions, Schottky barrier heights, interface behavior, and alignment with adjacent layers. This part of the interface serves as the foundation for constructing a realistic and physics-based model of the photovoltaic device.

b)- Light Direction and Electrical Boundary Conditions

The central section of the window focuses on defining key physical operating conditions of the device, especially related to illumination and voltage referencing. Using the "Illuminated from" setting, the direction of incident light can be selected either from the front or back of the device allowing simulation of single-junction or bifacial cells. The "Apply voltage to" option lets the user choose which contact receives the applied voltage, while "Current reference at" defines the terminal used as the current measurement reference. The checkbox "Invert the structure" enables automatic reversal of the layer order, which is useful when modeling inverted architectures. These controls are critical for ensuring that the simulated environment matches the real operating configuration of the solar cell under test.

c)- Saving Settings and Data Management

The lower part of the interface provides tools for data saving, retrieval, and organization of the simulation setup. Buttons such as "Save material" and "Load material" allow users to store and reuse material parameters, greatly facilitating iterative modeling and comparative analysis. Defect properties can also be managed separately via the "Add/Edit defects" tool, ensuring clarity and modularity in simulation inputs. When new layers are defined or existing ones are modified, confirmation through the "Accept layer" button is necessary to finalize the configuration. These features streamline the modeling workflow, reduce the risk of input errors, and enhance reproducibility in numerical solar cell simulations using SCAPS 1D.

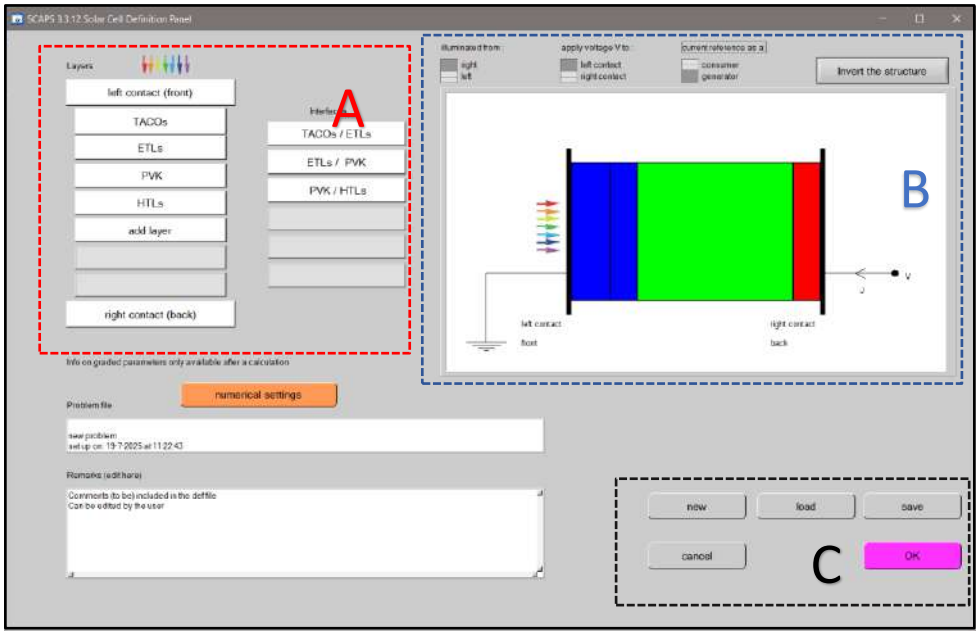


Figure A.9 Division of the "Set Problem" Window into Three Functional Zones in SCAPS 1D.

Zone 7 - Set Problem: Defining the Solar Cell Architecture and Its Components

The sixth zone in the SCAPS 1D interface, labeled as *Set Problem*, constitutes one of the most critical stages in preparing a physical simulation. This stage enables the construction of the complete structural model of the solar cell from the layer stack to the definition of illumination conditions, temperature, and voltage controls.

For clarity and methodological consistency in this dissertation, the *Set Problem* interface has been subdivided into three main zones:

- **Zone A** – Definition of the layer stack and contacts
- **Zone B** – Physical parameters and defects in layers
- **Zone C** – Illumination and biasing conditions

a)- Building the Structural Stack and Contacts of the Solar Cell:

Zone A represents the core step in constructing the solar cell structure within the *Set Problem* interface. Here, the user introduces all structural elements of the solar cell in a systematic and comprehensive manner. This zone is divided into three essential sub-windows:

- Add Layer
- Interface
- Left/Back Contact
    - **a.1) - Add Layer Window**:

This sub-window allows for the creation and addition of each layer that constitutes the solar cell from the front contact down to the back contact. Each layer must be defined with its corresponding physical and electronic parameters, including:

- Thickness
- Band gap energy
- Carrier type (n-type or p-type)
- Electron and hole concentrations
- Absorption coefficient (α)
- Electron and hole mobility
- Defect parameters and trap densities

The layers must be stacked in a logical sequence that mimics the real physical structure of the solar cell (e.g., ETL / Absorber / HTL), while accounting for metallic contacts at the boundaries.

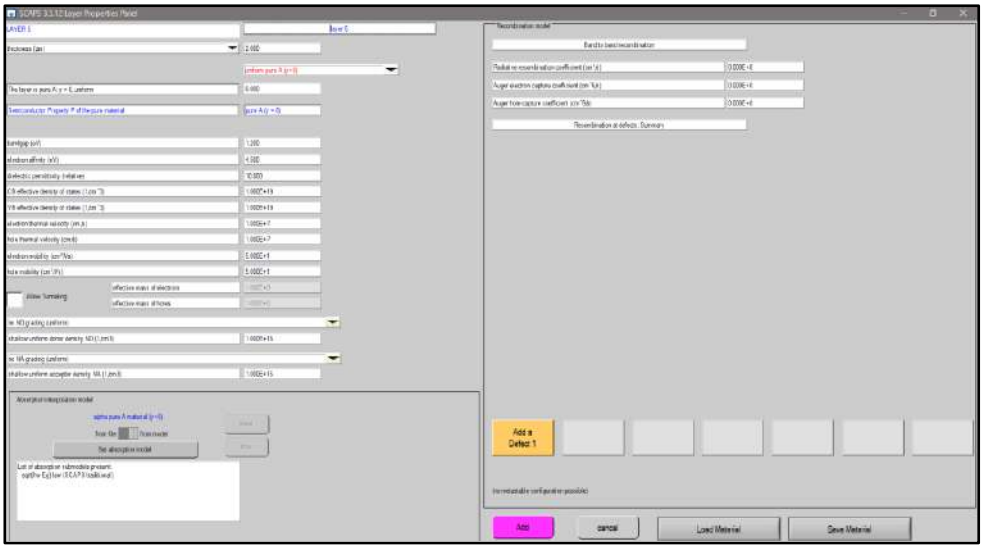


Figure A.10 Screenshot of the "Add Layer" window displaying the defined structure.

- **a.2)- Interface Window:**

Once layers are defined, the interfaces between each pair of adjacent layers are automatically created. This window provides options to define the physical characteristics of these interfaces, including:

- Recombination velocities for electrons and holes
- Interface defect densities
- Parameters for charge accumulation or barrier effects

These settings significantly influence device performance, especially in controlling non-radiative recombination losses.

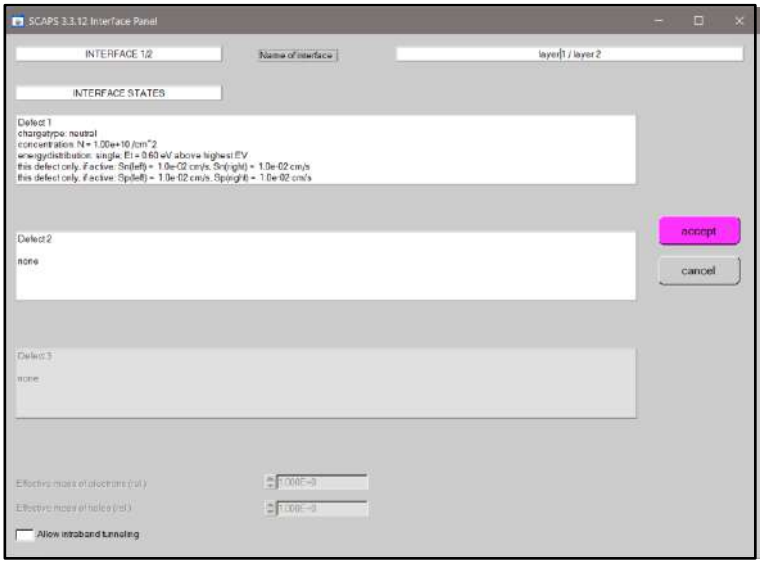


Figure A.11 Screenshot of the "Interface" window, focusing on a specific interface.

- **a.3) - Left/Back Contact Window:**

This sub-window is dedicated to the configuration of the back contact, which collects carriers (electrons or holes) after they traverse the device. Important parameters to be defined include:

- Work function
- Contact type (Ohmic or Schottky)
- Presence of optical filter or back reflector
- Thickness or partial transparency of the contact

These settings are crucial in minimizing energy losses at the rear side of the solar cell.

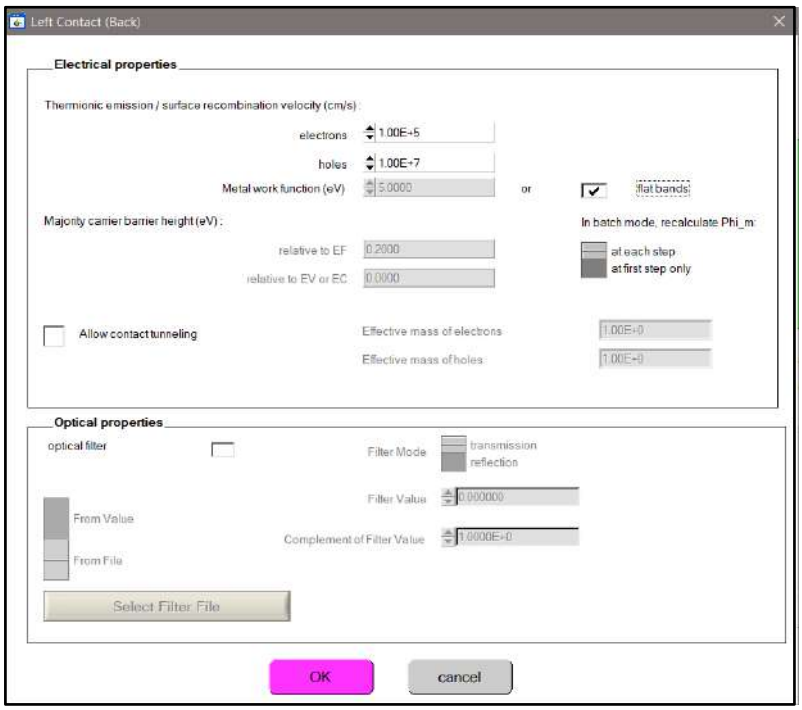


Figure A.12 Screenshot of the "Left Contact" window with visible work function setup and optical filtering options.

b)- Layer Structure Diagram:

Zone B of the SCAPS 1D interface plays a crucial role in providing a visual representation of the full layer structure of the solar cell, as previously defined in Zone A (Add Layer). This schematic diagram is automatically generated upon clicking the "Add Layer" button and reflects the sequence, type, thickness, and doping profile of each layer, along with the direction of light incidence.

- **Layer-by-Layer Representation**: The diagram displays each layer of the solar cell from top to bottom, corresponding to the order in which the layers were

defined. Each rectangular block in the diagram represents a single layer, and its relative width visually indicates the physical thickness of that layer, as specified in the "Add Layer" section.

- **Color Coding Based on Doping Type**: The program uses a color code to represent the doping type of each layer, which is determined by the values of ND (donor concentration) and N_A (acceptor concentration):
  - **Blue**: Indicates n-type doping (e.g., FTO, ETL), when $N_D > 0$ and $N_A = 0$.
  - **Red**: Indicates p-type doping (e.g., HTL), when $N_A > 0$ and ND = 0.
  - **Green**: Represents a co-doped or compensated layer ($N_D = N_A \neq 0$), or a layer where both doping values are non-zero and equal (when $N_D = N_A = 0$).

This visual encoding provides an intuitive insight into the electrostatic configuration and internal electric field distribution across the device structure.

- **Light Incidence Direction and Layer Inversion**: By default, the direction of incoming light is from the top (first defined layer). However, this can be adjusted using the "Inverter" checkbox located at the bottom of the diagram:
  - When unchecked, light enters from the topmost layer (standard configuration).
  - When checked, the direction of light incidence is reversed, so light enters from the bottom layer.

Additionally, the "Inverter" option can be used to mirror the entire stack structure, effectively reversing the layer sequence. This is particularly useful when simulating the device in p-i-n or n-i-p configurations, thus allowing for more flexible architectural studies and performance analysis based on structural orientation.

- **Dynamic Feedback from Parameter Changes**: Any modification in the layer thickness, defect density, values in Zone A is immediately reflected in the layer diagram. This makes Zone B a real-time diagnostic tool to verify the structural and electronic configuration before proceeding to simulation.



Figure A.13 Layer Structure Diagram of the Solar Cell in the SCAPS 1D Interface (Zone B). This figure illustrates the arrangement of layers, the doping type (indicated via color coding), and the direction of incident light.

c)- Device Settings File Management Tools

Zone C (as illustrated in the figure below) comprises a set of control buttons dedicated to managing the device configuration files within the "Set Problem" interface. These tools play a crucial role in enabling efficient creation, storage, and retrieval of solar cell device setups, thus ensuring a smooth and flexible workflow during simulation preparation.

Components of Zone C:

- **new**: This button is used to initialize a completely new device configuration. It resets all layers and parameters, allowing the user to start from scratch in designing a new solar cell structure.
- **load**: This function allows the user to import previously saved device configurations in SCAPS-compatible file formats. It is particularly useful when comparing multiple devices or resuming work on a previous design without re-entering all data manually.
- **save**: This option enables the user to save the current device setup (including layers, thicknesses, doping levels, and other material parameters) into a file for future access or documentation purposes.
- **cancel**: The cancel button discards any unsaved modifications and reverts to the previous state of the device setup.

- **OK**: This is the final confirmation button. Upon clicking it, all entered data in the "Set Problem" window are validated and transferred to the main simulation interface. This step is essential for proceeding with simulation tasks, such as defining operating conditions and recording output results.

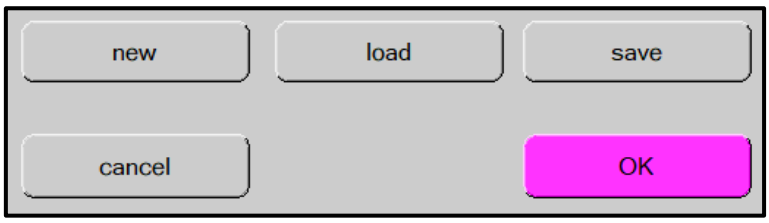


Figure A.14 Zone 6-C serves as a control interface for Zone 6, allowing the addition of new elements, reinitialization, and saving of changes.

Zone 8- Batch & Record Panel

The Batch & Record panel in SCAPS 1D serves as a powerful tool for performing automated and systematic simulations aimed at evaluating the impact of specific parameters on the photovoltaic performance of solar cells. This zone comprises two essential components: Batch Parameters and Record Options, both of which enable users to conduct in-depth numerical studies on the interplay between layer properties and electrical output.

- **Batch Parameters:**

The Batch section allows the user to define one or more input parameters to be varied systematically during a series of simulation runs. These parameters can be associated with specific layers such as thickness, doping concentration (N_D/N_A), defect density, or optical constants or with general simulation conditions. The user specifies the minimum and maximums valus and the number of steps, enabling either a linear sweep or a grid-based exploration of parameter space.

Typical use cases of the Batch function include:

- Studying the influence of absorber layer thickness on cell efficiency.
- Analyzing the effect of defect densities or recombination velocities across layers.
- Investigating doping gradient or mobility dependence on output parameters.

This tool is essential for sensitivity analysis, device optimization, and comparative studies of material configurations

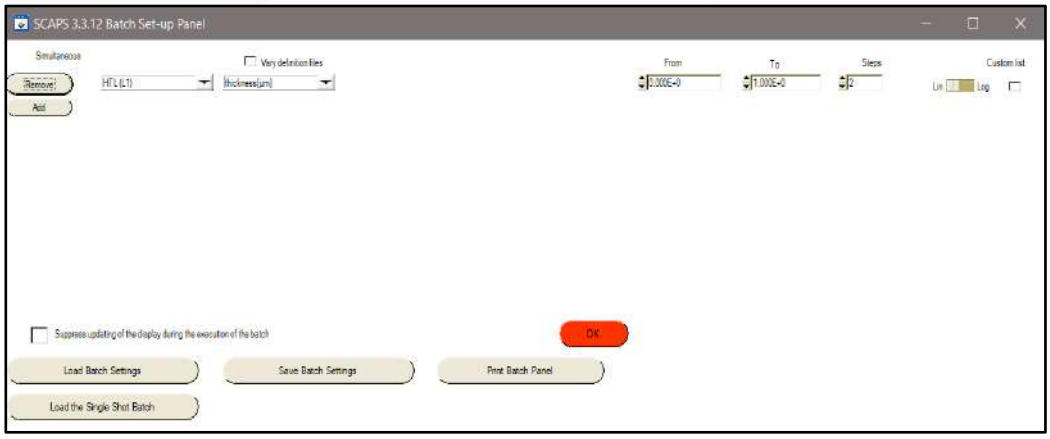


Figure A.15 This interface illustrates the configuration and execution of batch simulations for measurement and analysis.

- **Record Options:**

The Record panel allows users to select the physical quantities or output characteristics that are to be saved at each simulation step defined in the batch. These quantities include both local (spatially resolved within specific layers) and global performance metrics. Commonly recorded outputs include:

- Open-circuit voltage (Voc).
- Short-circuit current density (Jsc).
- Power conversion efficiency (PCE).
- Fill factor (FF).
- Quantum efficiency (QE).
- Internal electric field, recombination rates, or carrier densities at specific positions within the device.

The recording system is highly customizable, enabling users to specify precise spatial points within the layer stack to capture local values. This granularity is particularly useful when analyzing internal loss mechanisms, charge dynamics, or interface behaviors.

- **Coupled Analysis via Batch & Record:**

The true analytical strength of Zone 7 lies in the dynamic coupling between the Batch and Record functions. As a parameter is varied over a defined range using the Batch feature, corresponding results are simultaneously extracted through the Record function. This enables the creation of comprehensive data maps and performance trends as functions of layer properties or simulation conditions. For example:

- Mapping the dependence of Voc on the acceptor density in the hole transport layer.

- Investigating the effect of defect depth and density on the recombination profile across the device.

Such automation provides a deep understanding of sensitivity and optimization pathways, allowing for more informed decisions in device design and material selection.

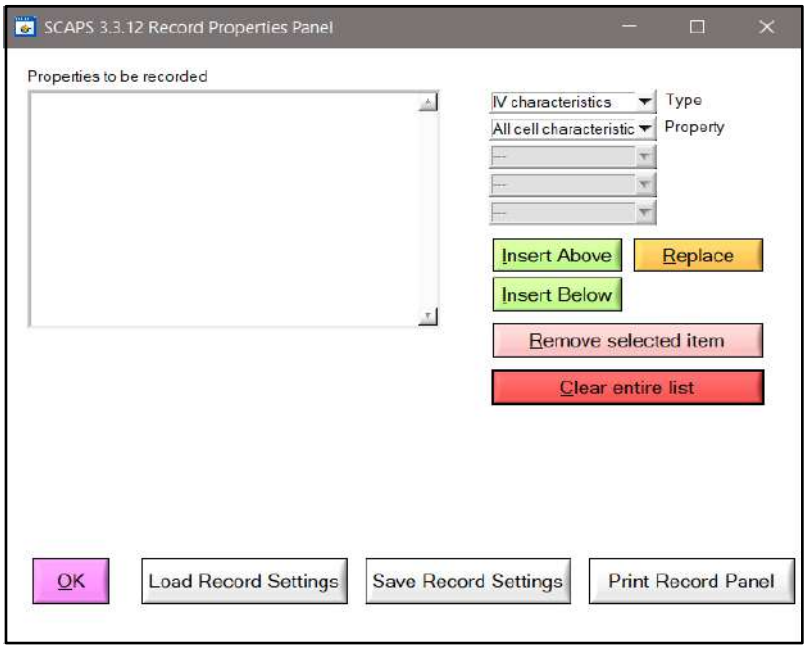


Figure A.16 The interface illustrates the configuration and execution of measurement parameters (Record) to be analyzed.

Zone 9- Execution of Batch and Record Calculations

This zone provides the control buttons to execute the simulation modes defined in Zone 7:

- **Calculate - Single Shot:** Runs a standard simulation using the currently defined device structure and conditions.
- **Calculate - Batch:** Executes all simulations defined in the batch file, systematically varying the selected parameter(s).
- **Calculate - Recorder**: Runs a simulation while extracting all quantities marked in the record file.

Zone 8 is inherently linked to Zone 7 its function depends on the batch and record configurations established there. It offers a flexible and efficient way to run multiple simulations and collect comprehensive output data with minimal manual intervention.

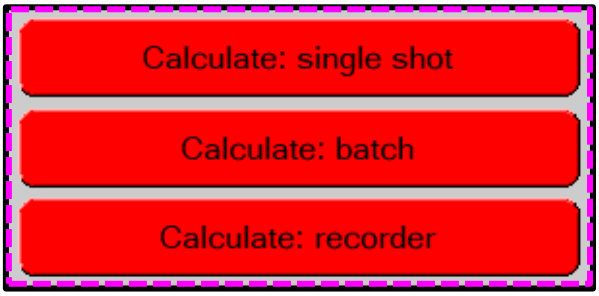


Figure A.17 This screen displays the execution of the simulation according to the predefined Batch and Record settings.

Zone 10 - Results Display Interface (Results of Calculations)

This area serves as the primary output module of SCAPS 1D, dedicated to presenting the computational results generated by the simulation process. The type and scope of the results displayed here are directly dependent on the simulation mode selected in the setup stage. Only the output relevant to the chosen simulation type is shown, rather than displaying all possible result categories.

The interface includes several specialized buttons, each corresponding to a specific type of physical or electrical analysis:

- **EB (Energy Bands)**: Displays band structure diagrams under equilibrium or applied bias conditions, enabling the examination of energy level distributions within semiconductor layers and the analysis of carrier transport mechanisms.
- **G, R (Generation and Recombination)**: Shows the spatial or temporal profiles of carrier generation and recombination rates, essential for evaluating solar cell performance and optical absorption efficiency.
- **AC (Alternating Current Response)**: Provides the device's small-signal AC response, useful for studying dynamic transport properties and extracting equivalent circuit parameters.
- **I–V (Current–Voltage Characteristics)**: Presents current–voltage curves under illuminated or dark conditions, serving as the primary metric for determining efficiency, open-circuit voltage, and short-circuit current.
- **C–V (Capacitance–Voltage)**: Displays capacitance as a function of applied voltage, allowing for the extraction of depletion layer properties and doping profiles.
- **C–f (Capacitance–Frequency)**: Shows the frequency dependence of capacitance, aiding in the detection of deep-level traps and recombination dynamics.

QE (Quantum Efficiency): Plots the spectral quantum efficiency, indicating the device's response to different wavelengths and revealing photon loss mechanisms.

The Recorder Results button at the bottom is specifically designed to present data recorded during simulations configured through the Batch or Recorder setup (in Zone 7). This enables sequential analysis of parameter variations or operational conditions across multiple simulation runs.

It is important to note that this area is functionally dependent on prior configuration choices: only the result types corresponding to the selected simulation mode will be available. This selective output approach enhances analytical efficiency by avoiding unnecessary data clutter and focusing the user's attention on physically relevant performance indicators.

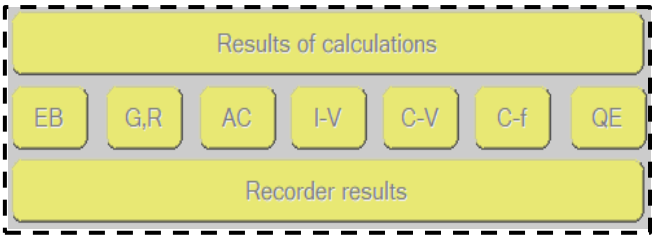


Figure A.18 Shows the simulation results based on the previously selected test type, displaying only the relevant outputs without including all default results.

- **How Can the Results Be Extracted from SCAPS 1D?**

In this example, we demonstrate the procedure for inserting and extracting simulation results using SCAPS 1D. The illumination conditions were first set and kept at their default standard configuration, followed by selecting four key simulations: I–V, C–V, C–f, and QE. This selection is performed by ticking the small boxes in front of each option, which turn black when activated and remain white when not selected.

Once the desired simulations are chosen, the calculation is initiated by pressing the simulation button. After a short computation time, the results are displayed in the form of graphical curves that represent the various physical responses of the solar cell. As illustrated in the attached figure, these outputs provide a detailed insight into the electrical and optical behavior of the studied structure.

It is worth emphasizing that the simulations provided by SCAPS 1D do not merely generate a single plot; rather, they yield a comprehensive set of curves, each of which provides deeper insight into the physical and electronic characteristics of the solar cell. Each type of simulation

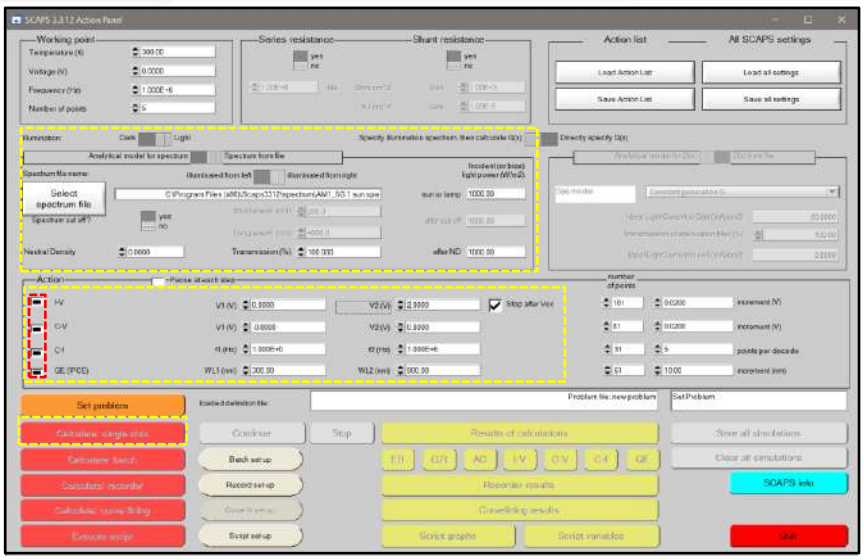


Figure A.19 Interface for configuring the initial settings prior to running the simulation in SCAPS 1D.

thus, represents a multidimensional perspective of device performance, reflecting mechanisms of charge transport, recombination, and spectral response dynamics.

In the case of Current-Voltage (I-V) simulations, several distinct curves can be obtained. The dark I-V curve enables the study of leakage currents and parasitic conduction, while the illuminated I-V curve constitutes the reference for extracting the main photovoltaic performance metrics, such as the open-circuit voltage (Voc), short-circuit current (Jsc), and fill factor (FF). Furthermore, comparative I-V analyses under varying illumination intensities and temperatures allow for an assessment of the influence of external conditions on device stability and efficiency.

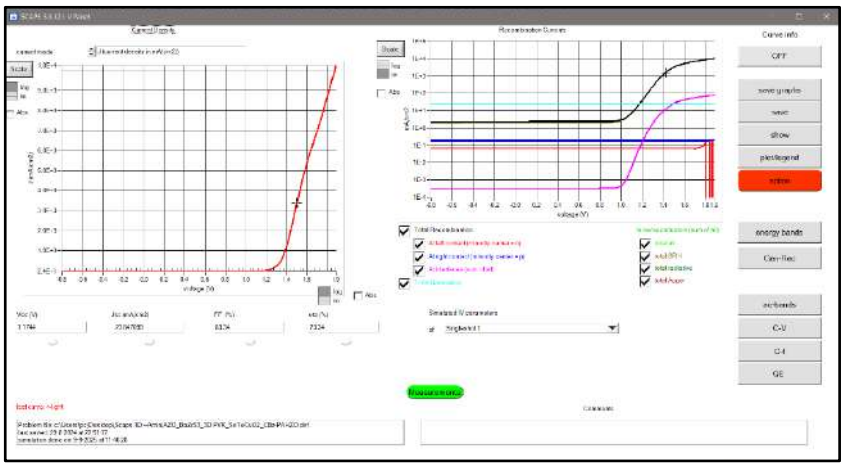


Figure A.20 Interface displaying the I-V parameter after completing the simulation in SCAPS 1D.

For Capacitance-Voltage (C-V) simulations, the outputs go beyond simple capacitance values. The variation of capacitance with applied bias can be analyzed, and the $\frac{1}{C^2}$ $(cm^2/nF)^2$ vs. Voltage representation is particularly useful for determining doping concentrations and the depletion width. Moreover, performing C-V analyses at different frequencies provides further insights into defect states and interfacial charge transport.

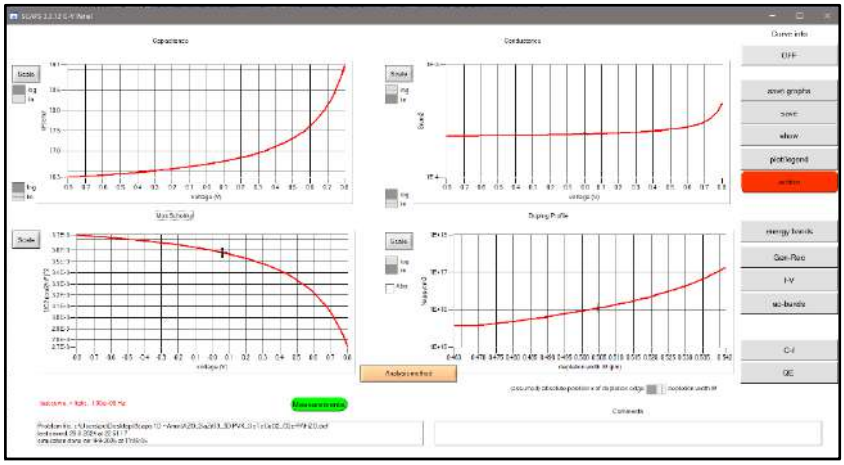


Figure A.21 Interface displaying the C-V parameter after completing the simulation in SCAPS 1D.

In Capacitance-Frequency (C-f) simulations, the focus is on the frequency response of the cell across a broad spectrum. At low frequencies, defect states and slow recombination dynamics dominate, while at high frequencies, fast free-carrier transport becomes evident. The transition between these regimes serves as a diagnostic tool for identifying deep-level defect states within the absorber material.

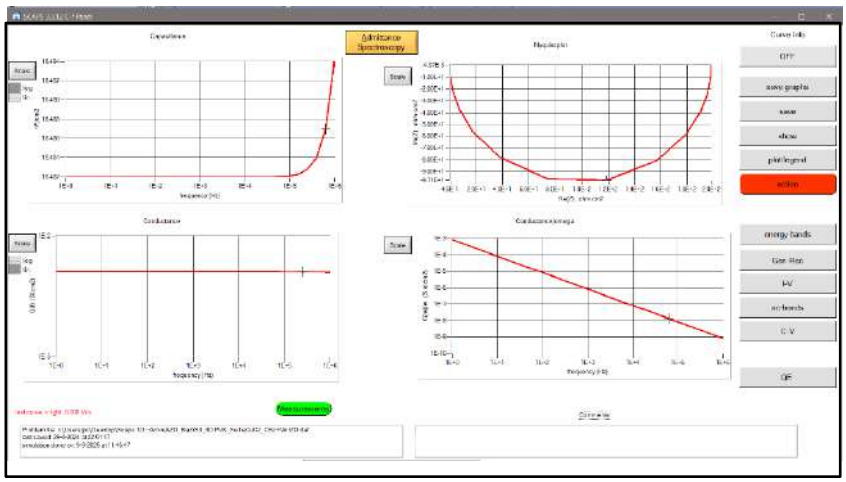


Figure A.22 Interface displaying the C-f parameter after completing the simulation in SCAPS 1D.

Finally, Quantum Efficiency (QE) simulations provide a detailed spectral analysis of the device, mapping the sensitivity of the absorber layer across the solar spectrum. This includes the decomposition of spectral contributions from individual functional layers (ETL, HTL, absorber) and comparative analysis under front versus rear illumination.

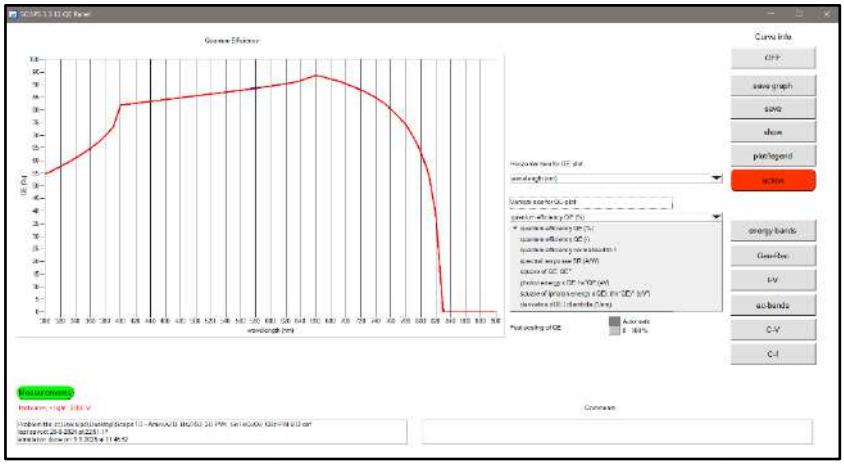


Figure A.23 Interface displaying the QE parameter after completing the simulation in SCAPS 1D.

Thus, the SCAPS 1D simulation results should not be perceived as single-curve outputs, but rather as bundles of analytical plots that equip the researcher with robust diagnostic and optimization tools for advancing solar cell performance.

The results saving interface in SCAPS 1D provides flexible tools for exporting and analyzing simulation outputs, along with an option to return to the main setup window. These functionalities can be classified into five main features:

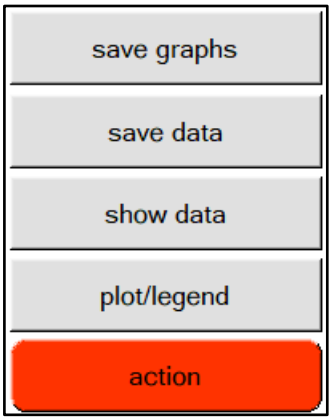


Figure A.24 SCAPS 1D interface providing multiple saving tools, including saving graphs, saving data.

- **Save Graphs:** Exports the simulation curves in various image formats (PNG, JPEG, BMP), either as a full panel or selected parts, allowing for direct inclusion in academic
- theses or scientific articles.

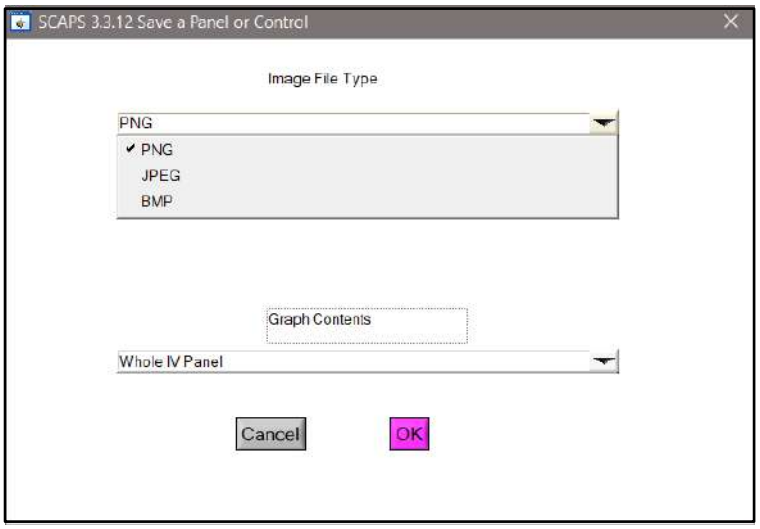


Figure A.25 SCAPS 1D interface illustrating the process of saving simulation plots as image files (e.g., PNG or JPEG) for documentation and analysis.

- **Save Data:** Stores the numerical results in text files or designated folders, enabling further processing with external analysis software such as Excel or Origin.

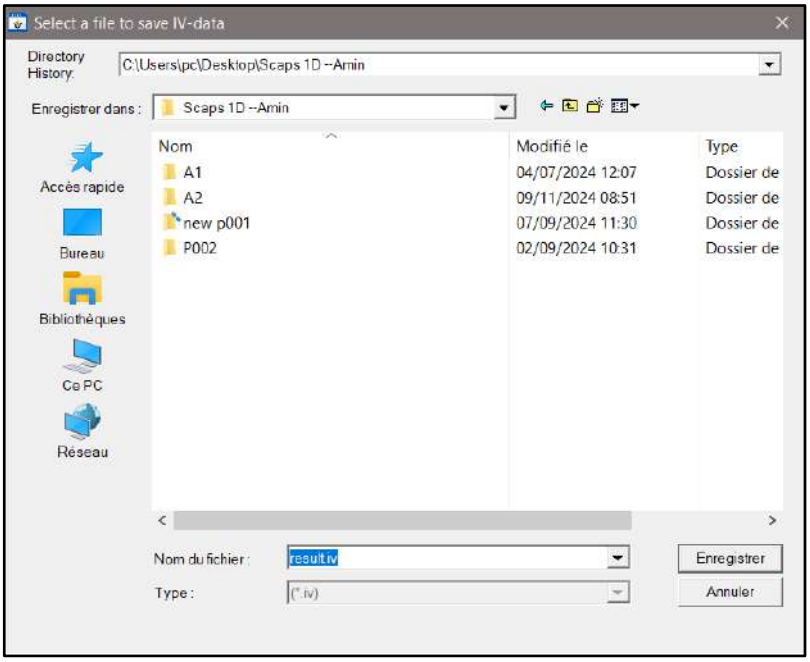


Figure A.26 interface showing the process of saving numerical results as a text file or in a designated folder for further processing with external tools such as Excel or Origin.

- **Show Data:** Displays detailed numerical values directly in the SCAPS 1D interface, with the option to copy and paste them into external programs for advanced processing or customized visualization.

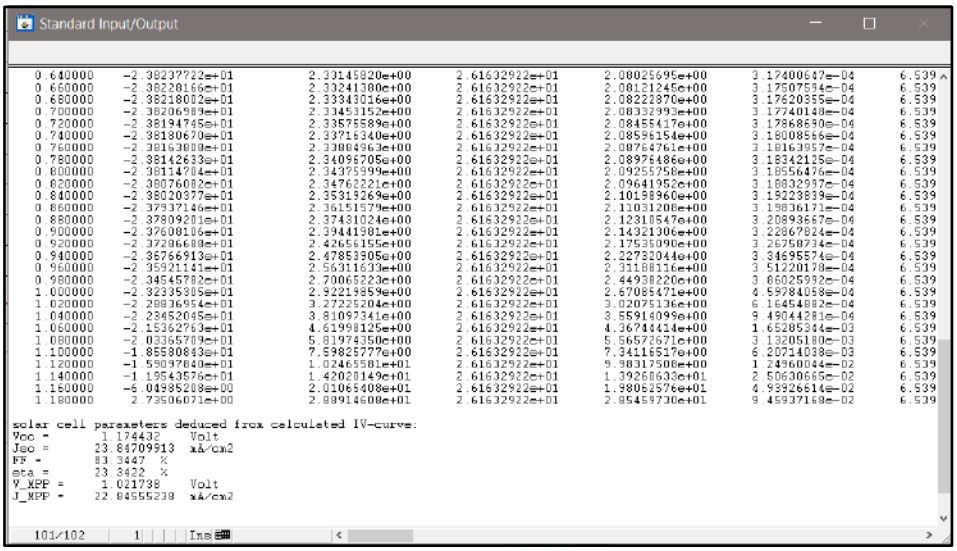


Figure A.27 SCAPS 1D interface illustrating the display of numerical results for direct preview without saving them to a file, with the option to copy and paste into external programs for further analysis.

- **Plot/Legend (Print):** Provides tools to format and print the graphs, with options to control scaling, layout, and annotations, ensuring professional-quality representation of the simulation results.

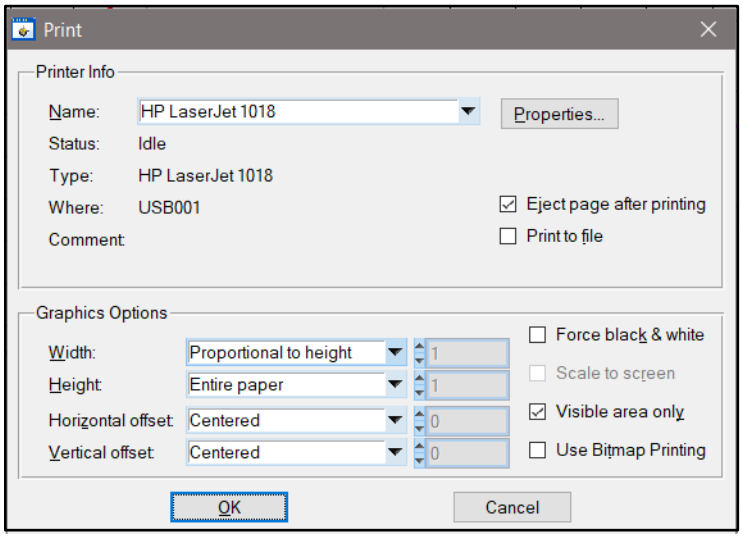


Figure A.28 SCAPS 1D interface showing how to print the simulated curves, with options to adjust scaling and annotations to ensure clear presentation in scientific reports.

- **Action:** Allows returning to the initial setup window (Set Problem or Numerical Settings) to adjust simulation parameters, facilitating an efficient workflow between result analysis and model configuration.

Zone 11 - Simulation Management and Program Control

This area provides essential commands for managing simulation sessions and controlling the overall execution of the SCAPS 1D environment. It contains four main functions:

1. **Save All Simulations**
    - Intended to store the complete set of simulation results currently loaded in memory into external files.
    - This function preserves both the numerical datasets and associated metadata, ensuring reproducibility and enabling post-processing or further analysis without re-running the simulations.
    - Typically becomes active when multiple completed simulations are present in the working session.

2. **Clear All Simulations**
    - Deletes all simulations and associated results from the current session's memory, resetting the simulation workspace.
    - This prevents unintentional overlap between successive simulation runs and conserves computational memory resources.

3. **SCAPS Info**
    - Displays information about the SCAPS 1D version, compilation details, licensing, and possibly the authorship or institutional credits.
    - Useful for citation purposes in academic publications and for verifying software updates in research workflows.

4. **Quit**
    - Exits the SCAPS 1D program entirely.
    - Users are typically prompted to save unsaved data before termination to avoid loss of results.

Functional Note

The Save All Simulations *and* Clear All Simulations buttons remain inactive unless at least one simulation has been executed during the current session. This conditional activation ensures that users cannot accidentally perform redundant or destructive operations when no data is present.

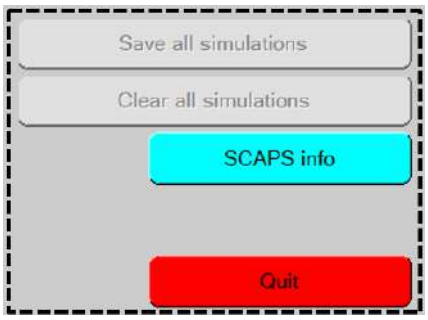


Figure A.29 This section enables the analysis of simulation data using the program's available tools for results visualization and interpretation.